W&M ScholarWorks

Dissertations, Theses, and Masters Projects

Theses, Dissertations, & Master Projects

1995

Calculations of the interactions of energetic ions with materials for protection of computer memory and biological systems

Myung-Hee Y. Kim
College of William & Mary - Arts & Sciences

Follow this and additional works at: https://scholarworks.wm.edu/etd

Part of the Investigative Techniques Commons, Nuclear Engineering Commons, Physics Commons, and the Polymer Chemistry Commons

Recommended Citation

Kim, Myung-Hee Y., "Calculations of the interactions of energetic ions with materials for protection of computer memory and biological systems" (1995). *Dissertations, Theses, and Masters Projects.* Paper 1539623872.
https://dx.doi.org/doi:10.21220/s2-8xy2-rm11

This Dissertation is brought to you for free and open access by the Theses, Dissertations, & Master Projects at W&M ScholarWorks. It has been accepted for inclusion in Dissertations, Theses, and Masters Projects by an authorized administrator of W&M ScholarWorks. For more information, please contact scholarworks@wm.edu.

INFORMATION TO USERS

This manuscript has been reproduced from the microfilm master. UMI films the text directly from the original or copy submitted. Thus, some thesis and dissertation copies are in typewriter face, while others may be from any type of computer printer.

The quality of this reproduction is dependent upon the quality of the copy submitted. Broken or indistinct print, colored or poor quality illustrations and photographs, print bleedthrough, substandard margins, and improper alignment can adversely affect reproduction.

In the unlikely event that the author did not send UMI a complete manuscript and there are missing pages, these will be noted. Also, if unauthorized copyright material had to be removed, a note will indicate the deletion.

Oversize materials (e.g., maps, drawings, charts) are reproduced by sectioning the original, beginning at the upper left-hand corner and continuing from left to right in equal sections with small overlaps. Each original is also photographed in one exposure and is included in reduced form at the back of the book.

Photographs included in the original manuscript have been reproduced xerographically in this copy. Higher quality 6" x 9" black and white photographic prints are available for any photographs or illustrations appearing in this copy for an additional charge. Contact UMI directly to order.

UMI

A Bell & Howell Information Company
300 North Zeeb Road, Ann Arbor, MI 48106-1346 USA
313/761-4700 800/521-0600

Reproduced with permission of the copyright owner. Further reproduction prohibited without permission.

Reproduced with permission of the copyright owner. Further reproduction prohibited without permission.

CALCULATIONS OF THE INTERACTIONS OF ENERGETIC IONS WITH MATERIALS FOR PROTECTION OF COMPUTER MEMORY AND BIOLOGICAL SYSTEMS

A Dissertation
Presented to
The Faculty of the Department of Applied Science
The College of William and Mary in Virginia

In Partial Fulfillment
Of the Requirements for the Degree of
Doctor of Philosophy

by
Myung-Hee Y. Kim
1995

Reproduced with permission of the copyright owner. Further reproduction prohibited without permission.

UMI Number: 9605788

UMI Microform 9605788
Copyright 1995, by UMI Company. All rights reserved.

This microform edition is protected against unauthorized
copying under Title 17, United States Code.

UMI
300 North Zeeb Road
Ann Arbor, MI 48103

Reproduced with permission of the copyright owner. Further reproduction prohibited without permission.

APPROVAL SHEET

This dissertation is submitted in partial fulfillment of

the requirements for the degree of

Doctor of Philosophy

Myung-Hee Y. Kim
Myung-Hee Yoon Kim

Approved, July 1995

Richard L. Kiefer, Ph.D.
Committee Chairman/Advisor

Robert A. Orwoll, Ph.D.

William J. Kossler, Ph.D.

Sheila A. Thibeault
Sheila A. Thibeault, Ph.D.
NASA Langley Research Center
Hampton, Virginia

John W. Wilson, Ph.D.
NASA Langley Research Center
Hampton, Virginia

Reproduced with permission of the copyright owner. Further reproduction prohibited without permission.

TABLE OF CONTENTS

Reproduced with permission of the copyright owner. Further reproduction prohibited without permission.

CHAPTER 3. EXPERIMENTAL/THEORETICAL STUDIES

3.3 Laboratory Ion Beams Transport on Shield Materials

CHAPTER 4. APPLICATION TO STATIC RANDOM ACCESS MEMORY DEVICES IN HZE EXPOSURE

CHAPTER 5. APPLICATION TO BIOLOGICAL SYSTEM IN HZE EXPOSURE

Reproduced with permission of the copyright owner. Further reproduction prohibited without permission.

Reproduced with permission of the copyright owner. Further reproduction prohibited without permission.

ACKNOWLEDGEMENTS

This work was supported by the NASA Space Exploration Initiative (SEI) Program, NASA Langley Research Center, and by the Department of Applied Science at the College of William and Mary. I am grateful to each of my committee members for their wise counsel and encouragement. Special acknowledgement is given to my supervisor Dr. Richard L. Kiefer for his inspiration and support throughout my study period. I appreciate the opportunity of having discussions with Dr. William J. Kossler. I also appreciate his time and effort for the review of this work. I wish to thank Dr. Sheila A. Thibeault for introducing me to research approaches and for encouraging me throughout this study. I also wish to thank Dr. Robert A. Orwoll for his guidance and constructive review of this manuscript. Dr. John W. Wilson is acknowledged for his generosity and guidance as an advisor to me in applying theoretical concepts and principles.

I am thankful to all the faculty, staff, and students in Polymer Science of the Department of Applied Science for their friendship.

I wish to specially thank my husband, Sung Chan, my daughter, Jee Yun, and my parents for their encouragement.

Reproduced with permission of the copyright owner. Further reproduction prohibited without permission.

LIST OF TABLES

Reproduced with permission of the copyright owner. Further reproduction prohibited without permission.

LIST OF FIGURES

Reproduced with permission of the copyright owner. Further reproduction prohibited without permission.

Reproduced with permission of the copyright owner. Further reproduction prohibited without permission.

Reproduced with permission of the copyright owner. Further reproduction prohibited without permission.

Reproduced with permission of the copyright owner. Further reproduction prohibited without permission.

Reproduced with permission of the copyright owner. Further reproduction prohibited without permission.

Reproduced with permission of the copyright owner. Further reproduction prohibited without permission.

ABSTRACT

Theoretical calculations were performed for the propagation and interactions of particles having high atomic numbers and energy through diverse shield materials including polymeric materials and epoxy-bound lunar regolith by using transport codes for laboratory ion beams and the cosmic ray spectrum. Heavy ions fragment and lose energy upon interactions with shielding materials of specified elemental composition, density, and thickness. A fragmenting heavy iron ion produces hundreds of isotopes during nuclear reactions, which are treated in the solution of the transport problem used here. A reduced set of 80 isotopes is sufficient to represent the charge distribution, but a minimum of 122 isotopes is necessary for the mass distribution. These isotopes are adequate for ion beams with charges equal to or less than 26. To predict the single event upset (SEU) rate in electronic devices, the resultant linear energy transfer (LET) spectra from the transport code behind various materials are coupled with a measured SEU cross section versus LET curve. The SEU rate on static random access memory (SRAM) is shown as a function of shield thickness for various materials. For a given mass the most effective shields for SEU reduction are materials with high hydrogen density, such as polyethylene. The shield effectiveness for protection of biological systems is examined by using conventional quality factors to calculate the dose equivalents and also by using the probability of the neoplastic transformation of shielded C3H10T1/2 mouse cells. The attenuation of biological effects within the shield and body tissues depends on the materials properties. The results predict that hydrogenous materials are good candidates for high-performance shields. Two biological models were used. Quantitative results depended upon model.

Reproduced with permission of the copyright owner. Further reproduction prohibited without permission.

CALCULATIONS OF THE INTERACTIONS OF ENERGETIC IONS WITH MATERIALS FOR PROTECTION OF COMPUTER MEMORY AND BIOLOGICAL SYSTEMS

Reproduced with permission of the copyright owner. Further reproduction prohibited without permission.

CHAPTER 1. INTRODUCTION

1.1 Overview

A deep space mission is one which extends beyond the Earth's magnetosphere, and generally involves the transfer from an Earth orbit to a solar orbit. Beyond the Van Allen radiation belts, solar cosmic rays (SCRs) and galactic cosmic rays (GCRs) are the only major sources of space radiation.

Since exploratory manned space missions of short duration have taken place in an Earth orbit, only the more intense space radiations, such as the radiations trapped in the Van Allen belts and SCRs, were considered. The exposure risk came from electrons and protons. For these radiations, conventional protection practice, which is an extrapolation based on the existing human database, may be adequate. The human database is mainly from γ-ray exposure data obtained from the nuclear weapons studies of World War II and from X-ray exposure data from patients undergoing radiation therapy.

For a deep space mission, the exposure from geomagnetically trapped radiation is reduced by a rapid transit through this region and the exposure from SCR could be controlled by using a small, highly shielded volume. The major source of radiation for career exposure limits is the low level background GCR. The GCR consists of a low flux

Reproduced with permission of the copyright owner. Further reproduction prohibited without permission.

of energetic bare nuclei which appear to fill our galaxy isotropically. It is known to extend from 0.1 GeV to energies up to ~10^{10} GeV, and includes all of the elements from hydrogen up to the actinides. Because of this enormous energy range, humans and microelectronic equipment in a lunar habitat or on a manned mission to Mars will require more protection from GCR than has been used heretofore on shorter missions. Although galactic heavy ions are 1-2 % of the GCR fluence, these energetic heavy nuclei (HZE) are of concern for radiation protection and radiation shielding technology, because gross rearrangements, mutations, and deletions in DNA are expected for humans which are the most radiation-sensitive component of the spacecraft. These HZE nuclei are biologically the most significant component and are very instrumental in causing single event upsets (SEUs) on microelectronics because of their unusually high specific ionization. SEU refers to the process by which ionizing radiation creates a sufficient number of electron-hole pairs in a circuit to establish an electrical current which causes a charge in the logic state of the device. Protecting space-borne microelectronics from SEU by transmitted radiation will benefit system reliability and system-design cost.

For GCR, the broad energy spectrum of HZE produces "surprises" for space-borne microelectronics, such as multibit SEUs that may not be seen in an accelerator experiment. The alterations induced in biological molecules by HZE nuclei are peculiar and are not readily produced by X-rays or γ-rays. Thus, accurate methods to estimate the risk resulting from HZE nuclei are needed for both space-borne computer memory and biological systems. The bioresponse to HZE nuclei for delayed effects must be more than

Reproduced with permission of the copyright owner. Further reproduction prohibited without permission.

an extrapolation of the human exposure database which is based primarily on X-ray and γ-ray exposures.

Radiation within a spacecraft structure, which interacts with onboard personnel or equipment, depends on the shield composition because different compositions have different atomic cross sections, nuclear attenuation, and distributions of fragmentation products. Selecting an appropriate composition of a structural piece, a container, or a coating is a recognized means of reducing the radiation hazard. A theoretical study was initiated to investigate the interaction and alteration of space radiations by various structural materials in order to select the materials that will provide the best shielding. The shield performance of potential space construction materials is compared theoretically in several different ways.

The objective of this study is to predict the effectiveness of various materials as shielding from HZE particles of GCR for a deep space mission. The typical nuclear radiation environment in space is summarized in section 1.2. Section 1.3 is a summary of the interaction and propagation of these primary space radiations through matter. Section 1.4 discusses radiation-protection issues. Chapter 2 deals with the development of the NASA LaRC transport codes and the database for HZE and nucleonic components in the straightahead approximation to compute fluxes, energy spectra, and linear energy transfer (LET) spectra. In chapter 3, the fluences of projectile fragments behind shield materials are calculated for laboratory ion beams, and the effects of isotope selection on solution

Reproduced with permission of the copyright owner. Further reproduction prohibited without permission.

accuracy are examined. The role of nuclear cross sections in modifying the space radiation fields within shield materials is investigated to assess the transmitted environment by using the GCR transport code. The associated effects of the modified environment on the microscopic distribution of the energy absorption events are discussed for the application to a computer memory system in chapter 4 and for the application to a biological system in chapter 5. Chapter 6 summarizes the shield effectiveness of some appropriate materials for a deep space mission and draws conclusions.

Reproduced with permission of the copyright owner. Further reproduction prohibited without permission.

1.2 High Charge and Energy Ions (HZE)

Cosmic rays have been studied for a long time and there are references of their characteristics[1-4]. These cosmic rays have extraordinary penetrating power and fall continuously upon the Earth from somewhere beyond. Since about 1925 this radiation has been known as cosmic radiation. The origin of most cosmic rays is probably in our galaxy, especially in supernova explosions[2,3], although the highest-energy components ($\geq 10^{17}$ eV amu^{-1}) may well be of extragalactic origin[4]. The Sun contributes significantly to the flux of low-energy (≤ 1 GeV amu^{-1}) cosmic rays arriving at the Earth. Disturbed regions on the Sun sporadically emit bursts of energetic charged particles into interplanetary space. The emission of these particles is associated with solar flares[1].

The types of particle radiations in space[5] are shown in figure 1a. The predominant types of particle radiations in the Earth's environment are solar wind protons, auroral electrons, solar storm protons, trapped protons, trapped electrons, solar cosmic rays (SCRs), and galactic cosmic rays (GCRs). There are temporal variations as well as spatial distributions.

The solar wind is really an extension of the solar corona, and extends to at least several astronomical units (1 AU $\approx 1.5 \times 10^8$ km). The solar wind is a plasma, which means that a substantial fraction of the matter is ionized. It is composed mostly of protons

Reproduced with permission of the copyright owner. Further reproduction prohibited without permission.

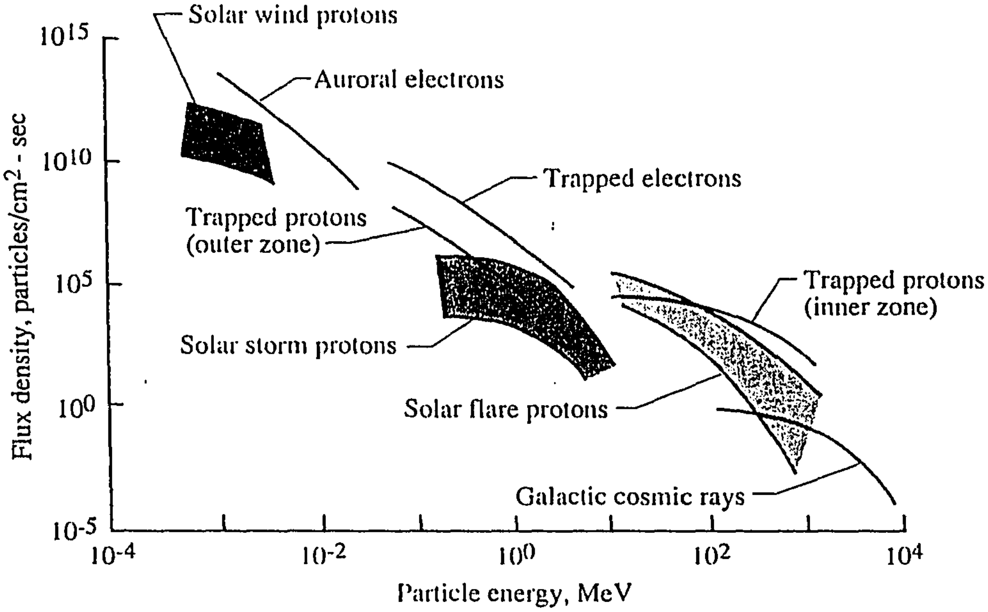

Figure 1a. Typical space particle radiation environment

Reproduced with permission of the copyright owner. Further reproduction prohibited without permission.

and is persistent through variable parts of the quiet Sun's output. The solar wind protons have thermal energies of ~1-10 keV. Except when the Sun is active, the solar wind constitutes the most important particulate solar radiation.

Charged particles are trapped in the geomagnetosphere, where there are two geomagnetically trapped radiation belts (Van Allen belts). The first (inner zone) is primarily centered at an altitude of 2,000 km; and the second (outer zone), at 20,000 km. These Van Allen belts are spatially distorted by the solar wind pressing on the geomagnetosphere.

A solar flare is an intense local brightening on the face of the Sun close to a sunspot. The solar abnormality results in an alteration of the general outflow of solar plasma at moderate energies, and in local solar magnetic fields which are carried by that plasma. As the solar plasma envelopes the Earth, the magnetic screening effects inherent in plasmas act to shield the Earth from galactic radiation known as a Forbush decrease, while contributing far more radiation of their own.

When the solar plasma interacts with the geomagnetic field a disturbance or storm occurs. During an intense magnetic disturbance, the Van Allen belt magnetic fields are compressed into the Earth's atmosphere in polar regions and trapped electrons are lost. These auroral electrons are seen only in polar regions after solar flares.

Reproduced with permission of the copyright owner. Further reproduction prohibited without permission.

The solar protons tend to be eliminated from equatorial regions of the magnetosphere as they are deflected by the horizontal geomagnetic field lines into space. However, solar primary particles arrive at the poles by moving along the near vertical geomagnetic filed lines and are thus not deflected. When the low-energy solar storm protons are channeled into the polar regions by the Earth's magnetic field, radio blackouts are produced in the lowest ionospheric region following certain solar flares, which is called a polar cap absorption event.

Solar energetic particles (SEP) are sometimes emitted during some solar flares and these events occur more frequently during periods of high solar activity. Solar cosmic ray (SCR) events with periods of several hours to days represent one of several short-lived manifestations of the active Sun. The solar wind and solar CR are composed of the same types of particles, mostly protons. These two groups of particles are distinguished by their numbers and speeds (energy). Solar CR have energies measured in millions of electron volts. SEP events occur relatively uniformly in time at low intensity and low energy. Rare clusters of high intensity and high energy events however are critical to spaceflight. In general, these latter major events happen during the ascending or descending phase of the solar sunspot cycle.

In addition to the radiation from the Sun, the Earth also is bombarded with charged particles from outside the solar system i.e. GCR. These particles have a range of energies that exceeds 10 GeV per nucleon. The region outside the solar system in the

Reproduced with permission of the copyright owner. Further reproduction prohibited without permission.

outer part of the galaxy is believed to be filled uniformly with cosmic rays. At 1 AU, the GCR flux is affected by solar activity due to interaction with the solar plasma emitted into the interplanetary space, and is out of phase with the Sun's activity - the more active the Sun, the smaller the GCR flux at the Earth.

The radiations with energies below 100 keV - such as solar wind protons and auroral electrons - and the solar storm protons with energies below 10 MeV are considered biologically unimportant since they are shielded against by even gaseous barriers. The most important radiations for biological consideration are the trapped protons in the inner zone, the trapped electrons in both the inner and the outer zones, solar cosmic rays, and galactic cosmic rays[6]. For interplanetary travel, the exposure from geomagnetically trapped radiations is reduced by a rapid transit through this region.

Two major origins of highly penetrating and damaging space radiations are SCRs and GCRs. The SCRs consist mostly of protons and with the next significant component being alpha particles. Even though the abundance of some heavy ions from major solar events may increase rapidly by 3 or 4 orders of magnitude above the galactic background for periods of several hours to days, these events are not of great concern for long-term missions since they are very rare and shielding against SCR is relatively easy by using a shelter and personal shielding. The GCRs also consist mostly of protons and alpha particles, but have a small but significant component of heavier particles. The existence of heavy ions in the galactic cosmic rays is observed at a high altitude in the Earth's

Reproduced with permission of the copyright owner. Further reproduction prohibited without permission.

atmosphere[7]. The unusually high specific ionization of these energetic heavy nuclei (HZE) indicates that they may pose a significant health hazard. Galactic heavy ions will probably be the ultimate limiting factor in space operations, because their relative dose contributions are comparable to those of the light particles but their biological effects are far more serious[6]. These are discussed below in sections 1.4 and 5.2.

The intensity of the GCR flux varies over the approximately 11-year solar cycle due to changes in the interplanetary plasma resulting from the expanding solar corona. The GCR flux reaching us is decreased during intense sun-spot activity, because the low-energy GCR particles are deflected by the Sun's enhanced magnetic field carried by the expanding solar plasma. The maximum dose received occurs at solar minima due to the lower solar plasma output. Measurements based on balloons and satellites at solar minimum modulation[8], in which major solar particle events are usually absent, show the greatest extent of GCR exposure[6].

Cosmic radiation has turned out to be a vital contributor to our understanding of high energy phenomena in our galaxy. The cosmic rays constitute approximately one-third of the energy density of the interstellar medium and, on a galactic scale, they form a relativistic gas whose pressure is important to take into account in the dynamics of galactic magnetic fields[8]. The cosmic ray nuclei are the only direct and measurable sample of matter from outside the solar system. It is a unique sample since it includes all of the elements from hydrogen up to the actinides. Cosmic rays are fully ionized nuclei. The

Reproduced with permission of the copyright owner. Further reproduction prohibited without permission.

electrons are stripped from the atoms during acceleration to CR energies. The cosmic radiation arriving beyond the Earth's magnetic field at the distance of the Earth from the Sun (i.e., 1 AU) is composed of ~ 98% nuclei and ~ 2% electrons and positrons[8]. In the energy range 10^8~10^{10} eV amu^{-1}, where it has its highest intensity, the nuclear component consists roughly of 87 % protons, ~ 12 % helium nuclei and a total of ~ 1 % for all of the heavier nuclei from carbon to the actinides[8].

While protons carry most of the CR energy, heavy particles give information on composition and propagation. Although GCRs probably include every natural element, not all are important for space radiation protection purposes. The elemental abundances for species heavier than iron (atomic charge number, $Z>26$) are typically 2 to 4 orders of magnitude smaller than that for iron[9]. Figure 1b illustrates the spectra at 1 AU for hydrogen, helium, and heavy nuclei up to nickel at the 1977 solar minimum modulation from the relatively quiet solar cycle 21 (1975-1986). In the solar system some elements such as the L nuclei (Li, Be, B), F and several nuclei between Si and Fe are quite rare[10]. Whereas in the CR flux these nuclei are present nearly as commonly as their neighbors[10]. This shows that their origin is in the breakup of heavy particles during CR propagation which would not be present in the CR sources. This generation of secondary nuclei[11] was shown using a one-dimension equilibrium solution ignoring ionization energy loss and radioactive decay. The more intense components of space radiations such as solar cosmic rays and trapped radiation were considered to be the principal radiation hazards for short duration exploratory missions since the continuous GCR background exposures are of low

Reproduced with permission of the copyright owner. Further reproduction prohibited without permission.

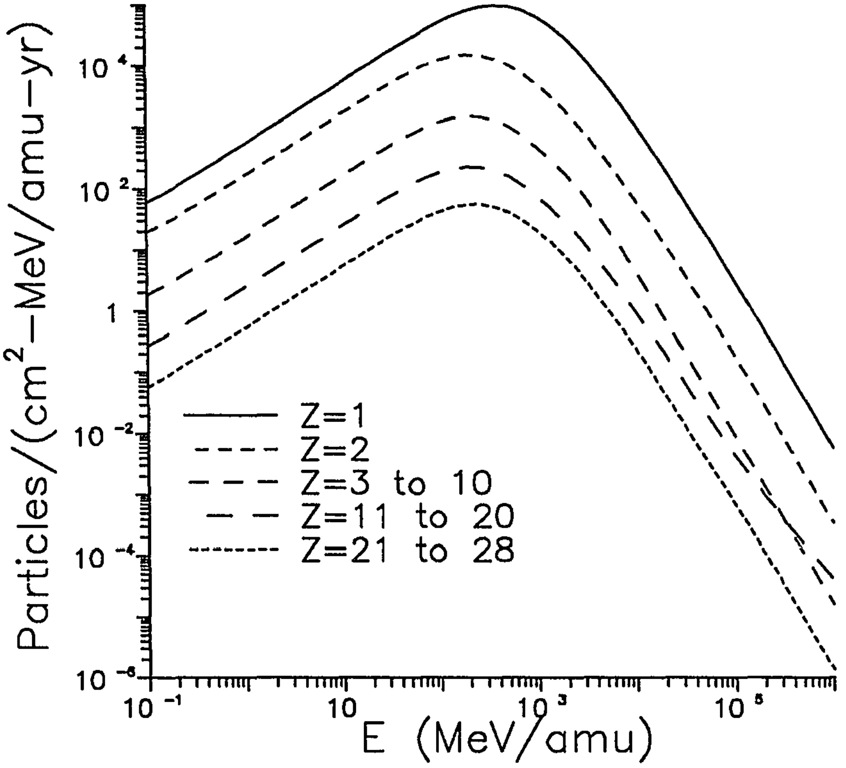

Figure 1b. Energy spectra of primary galactic cosmic ray ions at the 1977 solar minimum

Reproduced with permission of the copyright owner. Further reproduction prohibited without permission.

intensity. For the particles of high charge and energy (HZE) as components of the GCR, the unique pattern of energy deposition on the microscopic scale raised issues with respect to effects on living cells[12]. Delayed effects from long term exposures are suspected to come from continuous background HZE exposure of the GCR and they cannot be estimated by extrapolation from the well-established human database based primarily on X-ray and γ-ray exposures[13]. The exposures by GCR will be the ultimate limiting factor in deep space missions. Increased lifetime cancer risk above the natural incidence will be limited within 3 percent in future NASA missions as recommended by the National Council on Radiation Protection and Measurement[14].

Reproduced with permission of the copyright owner. Further reproduction prohibited without permission.

1.3 The Straightahead Approximation and Velocity Conserving Fragmentation Interactions

The propagation of galactic ions through matter has been studied by many researchers as a means of determining the origin of these ions as well as evaluation of required shielding. The calculations assume that the galactic cosmic components are transported through a material as their energies are attenuated by transfer to electrons of the media or by the generation of a multitude of cascading secondary particles from all subsequent-generation collisions. These calculations have been carried out using the straightahead approximation. This approximation reduces the calculation to a one-dimensional transport and it applies to both elastic and non-elastic collisions. Therefore, all emergent particles have the same direction of motion as the incident particle. Even though this approximation usually overestimates the dose, the error, by comparison to the exact calculations for space vehicle shielding, is often small[15].

Space radiations are nearly isotropic. Thus, in this field of isotropic radiation, the dose at a specific slab-shield thickness with normal incident radiation is equivalent to the dose in the center of a spherical shield of the same thickness. With CR propagation through space, it is customary, and more useful physically, to express distances by the total mass of all atoms encountered (in grams per square centimeter). The thickness of

Reproduced with permission of the copyright owner. Further reproduction prohibited without permission.

absorber in g/cm^2 can be converted to a linear thickness by dividing by the density of the shield material. This measure of thickness allows immediate comparison between various materials of equal shield mass.

The projectile nuclei moving at relativistic speeds collide with stationary target nuclei. In the overlap region of the colliding nuclei, nucleons are removed from the projectile nucleus by direct knockout. As a result of the dynamics of the removal process of nucleons, the primary residue is highly excited. In the calculations presented here the compound nuclear model is used to describe the decay of the excited residual nucleus. A high-energy nucleus may make collisions while traversing a complex target nucleus, leaving behind a fraction of its energy as excitation energy, and directly ejecting one or more nucleons (protons or neutrons), or clusters such as deuterons, tritons, helions, or α particles[16]. A particular final nuclide as a result of the de-excitation of a primary residue is the nuclear fragment, sometimes referred to as a secondary product. Customarily in cosmic ion transport studies, the fragment velocities are assumed to be equal to the fragmenting ion velocity before collision at the interaction site[16,17]. The assumption of velocity conservation (β conserved) is adequate for space radiations calculations[18] because the difference between the results with and without this assumption were found to be negligible[6].

Reproduced with permission of the copyright owner. Further reproduction prohibited without permission.

1.4 Application to Various Radiation-Protection Issues

Radiation hazard risks are characterized as either deterministic or stochastic. Deterministic radiation effects are identified by relating the severity of injury to the degree of exposure. Even though a given level of exposure will result in different levels of injury among a group of individuals, the severity of injury for a given individual increases with increased exposure level. The injury in most tissues results mainly from the inability of the cells to undergo division (clonogenic death). The three main deterministic effects[14] are prodromal response (i.e., anorexia, nausea, fatigue, vomiting, diarrhea), temporary sterility, and ocular lens opacity. Stochastic radiation effects are identified by the probability of occurrence, not severity, being related to degree of exposure. Although a given level of exposure will represent some level of risk for a given group, the risk within a given subgroup may be higher or lower at the same exposure level. The main stochastic effect is cancer induction. The occurrence of cancer is associated with changes in the genetic structure of a cell (transformation) for which the normal controls against cell division have been inactivated. The primary radiation protection from solar flares is to control early somatic radiation effects, which may impact mission safety. The risk of stochastic effects is defined in terms of the excess lifetime probability of cancer. This has been of secondary importance for short term space operations in low Earth orbit (LEO). It has been the recommendation by the National Council on Radiation Protection and

Reproduced with permission of the copyright owner. Further reproduction prohibited without permission.

Measurement[14] that exposure induced cancer risk be limited to not more than 3 percent above the estimated natural probability.

Career exposure limits are determined by late somatic effects. These in turn are the ultimate limiting factor on mission durations[14]. Late somatic effects, such as cancer, are not immediately observable and occur by chance according to the laws of probability. These are not genetic or hereditary effects. The delayed effects are mainly the consequence of exposure to the highly charged energetic (HZE) nuclei of galactic cosmic rays (GCR). The radial spread of ionization by HZE nuclei is on the order of biological cell dimensions[13] (2 - 10 μm), and the dimensions of many modern large integrated circuits[6] (0.5 μm). For this scale, the effects of HZE nuclei, either directly by ionization or indirectly by the ionization of secondary electrons (δ-rays), become important as the biologically most significant hazards and as interruptive events of electronic circuits.

In LEO, the predominant exposure is from electrons and protons. For this radiation, extrapolations based on existing radiobiological data may be adequate. The quantities commonly used in radiation protection, such as dose, dose equivalent, and quality factor, have been used to establish radiation limits. The quality factor is a function of the linear energy transfer (LET) of the radiation and is a defined quantity rather than the result of a measurement.

Reproduced with permission of the copyright owner. Further reproduction prohibited without permission.

A specific damage produced by radiation is called a biological end point and includes such consequences as leukemia, anemia, sterility, carcinogenesis, shortening of life span, etc. There is growing evidence of biological end points which are peculiar to high-LET HZE exposures that are not readily produced by X-rays or γ-rays. For such biological end points, the relative biological effectiveness (RBE), which is the ratio of γ-ray and specific ion exposure levels resulting in the same biological end point, is very large or possibly undefined. The RBE becomes infinite if γ-rays do not produce the biological end point. This occurs, for example, in sister chromatid exchanges in resting human lymphocytes irradiated with ^{238}Pu α-particles[19], abnormalities in stem cell colonies surviving similar α-particle irradiation[20], and the partial disintegration of chromosomes after irradiation with high-energy heavy ion beams[21]. Thus, a new method to predict the risk resulting from exposure to GCR radiation must be developed. This must be more than an extrapolation of the human exposure database for low-LET exposures. Accurate conversion of the radiation environment to estimated exposure fields at specific tissue sites.

In passing through shield material, the GCR interacts mostly by transferring small amounts of momentum to orbital electrons causing ionization of the atomic constituents . Although nuclear reactions are far less numerous, their effects are magnified because of the large momentum transferred to the nuclear particles and the struck nucleus itself. Many secondary particles of nuclear reactions are sufficiently energetic in turn to produce similar nuclear reactions and thus cause a buildup of secondary radiations. On the other

Reproduced with permission of the copyright owner. Further reproduction prohibited without permission.

hand the secondaries produced by the fragmentation are less ionizing and have less LET. Thus they may pose a reduced hazard.

Radiation shielding is an attempt to control the radiation environment, in particular to lower the LET of the incident ions. While the traditional structural material in the space program has been aluminum because of its strength per unit mass and its good thermal properties, other structural shield materials would better reduce the exposure risk from space radiations. Shield material for GCR may be characterized by what if transmits. There is larger interaction (cm^2/g) between HZE nuclei and light nuclear targets[22], so hydrogen-containing materials, such as many organic polymers, are most effective per unit mass.

Neutrons, formed in nuclear reactions between HZE particles and nuclei in shield materials, would be present in the internal environment of a space vehicle and would interact with onboard personnel or equipment. Fast neutrons (> 1 MeV) and protons that are produced in fragmentations can produce energetic reactions with the silicon of an electronic device, resulting in the production of heavy recoil ions which can cause single event upsets (SEU) in sensitive components. Being uncharged, these secondary neutrons cannot dissipate their kinetic energy through Coulombic interactions. Neutrons can only lose energy by collisions or reactions with a nucleus. The lighter the nucleus, the greater the amount of energy that can be lost in an elastic collision with a neutron. Neutrons are thermalized by repeated collisions with light nuclei, especially protons in a hydrogenous

Reproduced with permission of the copyright owner. Further reproduction prohibited without permission.

polymer medium. While low-energy secondary charged particles are stopped near their point of production, low-energy neutrons are able to migrate far from the beam axis. At large distances from the beam, only a net outward flux of low-energy neutrons is observed. This flux decreases exponentially because of absorptive processes in the medium (ultimately, neutron capture). The products of such reactions are very often radioactive. Thus, protection from low energy neutrons is important during a long duration space flight. The addition of boron to a shield is one means that allows the material to absorb low-energy neutrons because the isotope ^{10}B has a very high neutron capture cross section. The products of the reaction, ^{4}He and ^{7}Li, are not radioactive and are readily absorbed in the material. Thus, boron-containing polymers have possible uses as structural material for a spacecraft or as a container for electronic devices.

Reproduced with permission of the copyright owner. Further reproduction prohibited without permission.

CHAPTER 2. GALACTIC COSMIC RAY TRANSPORT

2.1 Introduction

Heavy ion transport is important for an understanding of the origin of galactic cosmic rays (GCR). The average density in interstellar space is 1 atom/cm^3, and the path lengths for nuclear collisions are on the order of 3 to 4 g/cm^2. Thus in interstellar space fragmentation cross sections are needed only to the first order, however higher order terms cannot be ignored in accelerator or space shielding transport problems[23].

Approaches to the solution of high-energy, heavy-ion (HZE) propagation, including the ionization energy loss, have been developed over the last 20 years. Wilson derived an expression for the high-energy heavy ion transport problem including in the first-order in collisions term and then examined it up to 6-order corrections by an iterative method[23]. The straightahead approximation mentioned earlier with velocity conservation on fragmentation usually appears sufficient[18] for space applications because the primary ions display a broad energy spectrum and arrive isotropically. Thus details which might be seen in a more exact calculation are averaged over. The calculation shows that a first-order perturbation theory is generally insufficient to represent the transport process. Solution methods included the nuclear cross section's dependence on fragment energies. Another approach has been made by Wilson who added a second collision term to an

Reproduced with permission of the copyright owner. Further reproduction prohibited without permission.

analytic expansion[24] of the heavy ion transport solution. This term was found to be very important in describing 670 MeV/amu ^{20}Ne beams[25]. The three-term expansion of perturbation theory was modified to also include the effects of the energy variation of the nuclear cross section[25]. The results from the code were further compared with ^{20}Ne transport experiments at the Lawrence Berkeley Laboratory (LBL) BEVALAC accelerator[26, 27].

To investigate the interaction and alteration of energetic heavy nuclei of GCR by structural materials, a laboratory ion-beam transport code[28] (LBLBEAM) with perturbation theory is used. Total ion fluences at the down stream face of a shield for incident monoenergetic, single ion beams are calculated in the present work for different shield thicknesses. The monoenergetic projectiles are ^{56}Fe beams at an incident kinetic energy of 605 MeV/amu and ^{20}Ne beams at 425 MeV/amu. These projectiles are chosen for analysis because relativistic ^{56}Fe nuclei are among the dominant HZE particles in GCR of radiobiological significance for manned spaceflight and ^{20}Ne is about equal in abundance to iron.

To provide computationally efficient HZE transport codes for laboratory ion beam applications, a radical reorientation was made[29]. For laboratory radiations, nearly monoenergetic beams may be handled with an analytic representation, while for the broad continuous-energy spectrum of space radiation numerical methods are required. The perturbation code was converted to use the nuclear fragmentation (NUCFRG) database[30].

Reproduced with permission of the copyright owner. Further reproduction prohibited without permission.

An analytic solution to the HZE transport equation in terms of a Green's function representing nuclear and atomic/molecular processes (GRNTRN[31]) is used. The nonperturbative Green's function code virtually eliminates numerically generated and propagated errors[29]. The solutions themselves must represent the fields associated with all of the isotopes produced in the fragmentation process. The solution convergence in HZE transport is examined by choosing various selections of isotopes used in the calculation to determine which contribute to the solution in a significant way.

The integral form of the transport equation was also used to derive a numerical marching procedure to solve the cosmic ray transport problem[32]. In this procedure, the boundary condition fluences are propagated by a small distance into the interior region of and these are then propagated in successive cycles to arbitrary distance[32]. This marching procedure can easily include the energy-dependent nuclear cross sections[30] within the numerical procedure. A comparison of the numerical procedure[32] with an analytic benchmark solution to a simplified problem[33] validates the solution technique to about 1 percent accuracy. Thus, analytic methods[23] were applied in a marching procedure. Solutions to a more complete theory were derived with the general Boltzmann equation and simplified by using the standard assumptions for the straightahead equation in the continuous slowing down approximation ($-dE/dx$) with the assumption that heavy projectile breakup conserves velocity[18]. A numerical procedure was derived with the coupling of the heavy ions to the nucleon fields[32]. This galactic cosmic ray (GCR) transport code, HZETRN[18], is used to predict the propagation and interactions of the

Reproduced with permission of the copyright owner. Further reproduction prohibited without permission.

deep-space nucleons and heavy ions through various media for further investigation of shield effectiveness.

Calculations are performed on a VAX 4000/500 system by using transport codes (LBLBEAM[28], GRNTRN[31], HZETRN[18]), the nuclear fragmentation database (NUCFRG[30]), and a LET distribution code (LET[46]) developed at NASA Langley Research Center. The computation time required for the nonperturbation code (GRNTRN) is approximately 10 minutes[31], while 15 minutes for evaluation of the first collision term and 45 minumtes for the second collision term for the perturbation code (LBLBEAM). Theories of codes are summarized in the following sections.

Reproduced with permission of the copyright owner. Further reproduction prohibited without permission.

2.2 NASA-LaRC HZETRN Code System

2.2.1 Modeling of Monoenergetic, Single-Ion Beam Transport with Perturbation Theory

In moving through extended matter, heavy ions lose energy through interaction with atomic electrons along their trajectories because electrons are so much lighter. On occasion, they interact with nuclei of the matter and produce ion fragments moving in the forward direction and low energy fragments of the struck target nucleus. The rare nuclear reactions are important because a large amount of energy is transferred in the reaction and the ion fragments are energetic. With the straightahead approximation and neglecting heavier target secondary fragments, the Boltzmann transport equation is written as[28]

$$\left[\frac{\partial}{\partial x} - \frac{\partial}{\partial E}\tilde{S}_j(E) + \sigma_j\right]\phi_j(x,E) = \sum_{k>j} m_{jk}\sigma_k\phi_k(x,E) \qquad (2.1)$$

where $\phi_j(x,E)$ is the flux of ions of type j with atomic mass A_j at x moving along the x-axis at energy E in units of MeV/amu, σ_j is the corresponding macroscopic nuclear absorption cross section, $\tilde{S}_j(E)$ is the change in E per unit distance, and m_{jk} is the fragmenting parameter for ion j produced in collision by ion k. The range of the ion $R_j(E)$ is then obtained by[28]

$$R_j(E) = \int_0^E \frac{dE'}{\tilde{S}_j(E')} \quad . \qquad (2.2)$$

From Bethe's theory[34]

$$\tilde{S}_j(E) = \frac{A_p Z_j^2}{A_j Z_p^2}\tilde{S}_p(E) \qquad (2.3)$$

Reproduced with permission of the copyright owner. Further reproduction prohibited without permission.

for which

$$\frac{Z_j^2}{A_j} R_j(E) = \frac{Z_p^2}{A_p} R_p(E) \tag{2.4}$$

The subscript p refers to a proton. The parameter ν_j is defined as[28]

$$\nu_j = \frac{Z_j^2}{A_j} \quad , \tag{2.5}$$

so that

$$\nu_j \, R_j(E) = \nu_k \, R_k(E) \quad . \tag{2.6}$$

The solution to equation (2.1) is to be found subject to boundary specification at x=0 and arbitrary E as[28]

$$\phi_j(0,E) = F_j(E) \, . \tag{2.7}$$

Usually $F_j(E)$ is called the incident beam spectrum. The boundary condition for a monoenergetic beam of type M ions is taken as[28]

$$F_j(E) = \delta_{jM} \, \delta(E - E_0) \, , \tag{2.8}$$

where δ_{jM} is the Kronecker delta, $\delta(E\text{-}E_0)$ is the Dirac delta, and E_0 is the incident beam energy. The uncollided flux to equation (2.1) for a monoenergetic beam of type M ions is[28]

$$\phi_j^{(0)}(x,E) = \frac{1}{\tilde{S}_j(E)} \exp(-\sigma_j x) \, \delta_{jM} \, \delta\left[x + R_j(E) - R_M(E_0)\right] . \tag{2.9}$$

For the first collision term, Wilson et al.[28] get

$$\phi_j^{(1)}(x,E) = \frac{1}{\tilde{S}_j(E)} m_{jM} \sigma_{jM} \frac{\nu_j}{\left|\nu_M - \nu_j\right|} \exp\left\{-\frac{1}{2}\sigma_j\left[x - R_j(E) - \eta'\right] - \frac{1}{2}\sigma_M\left[x + R_j(E) + \eta'\right]\right\} \tag{2.10}$$

where

$$\eta' = \frac{2\nu_M}{\nu_M - \nu_j} R_M(E_0) - \frac{\nu_M + \nu_j}{\nu_M - \nu_j}\left(x + R_j(E)\right) \tag{2.11}$$

Reproduced with permission of the copyright owner. Further reproduction prohibited without permission.

for $R_j(E)$ such that

$$\frac{v_M}{v_j}[R_M(E_0)-x] < R_j(E) < \frac{v_M}{v_j}R_M(E_0)-x. \tag{2.12}$$

Otherwise $\phi_j^{(1)}(x,E)$ is taken to be zero. After a complicated but straightforward manipulation, a similar result may be obtained for $\phi_j^{(2)}(x,E)$.

The solution to equation (2.1) is approximated as

$$\phi_j(x,E) = \phi_j^{(0)}(x,E) + \phi_j^{(1)}(x,E) + \phi_j^{(2)}(x,E) \tag{2.13}$$

where $\phi_j^{(0)}(x,E)$ is the attenuated primary ion fluence, $\phi_j^{(1)}(x,E)$ is the first collision term and $\phi_j^{(2)}(x,E)$ is the second collision term. Higher order collision terms are neglected. The results of the first collision term, $\phi_j^{(1)}(x,E)$, and the second collision term, $\phi_j^{(2)}(x,E)$, are integrated numerically over their entire energy spectrum. The total integral flux associated with each term is evaluated by using

$$\Phi_j^{(1)}(x) = \int_0^\infty \phi_j^{(1)}(x,E)dE \approx \sum_i \phi_j^{(1)}(x,E_i)(\Delta E) \tag{2.14}$$

$$\Phi_j^{(2)}(x) = \int_0^\infty \phi_j^{(2)}(x,E)dE \approx \sum_i \phi_j^{(2)}(x,E_i)(\Delta E)\ . \tag{2.15}$$

For a three-term perturbation expansion, the total ion fluence is

$$\Phi_j(x) = \Phi_j^{(0)}(x) + \Phi_j^{(1)} + \Phi_j^{(2)}(x). \tag{2.16}$$

The flux of each identified nucleus with charge Z, $\phi_Z(x,E)$, is defined as

$$\phi_Z(x,E) = \sum_{A_j} \phi_{ZA_j}(x,E) \tag{2.17}$$

where $\phi_{ZA_j}(x,E)$ is the same as $\phi_j(x,E)$ of equation (2.13) for all of the isotopes of projectile fragment charge Z with different atomic mass A_j. Equation (2.17) is integrated numerically over the entire energy spectrum and the total integral flux for each charge Z is approximated as

$$\Phi_Z(x) = \int_0^\infty \phi_Z(x,E)dE \approx \sum_i \phi_z(x,E_i)(\Delta E)\ . \tag{2.18}$$

Reproduced with permission of the copyright owner. Further reproduction prohibited without permission.

These are compared for different shield materials in section 3.3.1. In these calculations, the fragmentation cross sections of Silberberg, Tsao, and Shapiro[35] were the only ones used.

Reproduced with permission of the copyright owner. Further reproduction prohibited without permission.

2.2.2 A Semiempirical Nuclear Fragmentation Model

Fragmentation cross section databases are a major input into the transport codes. The Silberberg-Tsao model[36] is used mainly for high charge and energy ion (HZE) fragmentation on hydrogen targets. The scaled Silberberg-Tsao cross sections augmented with Bertini cross sections[37] are used for the lightest fragment (n, p, ^{2}H, ^{3}H, ^{3}He, ^{4}He) cross sections for nucleon and cluster production with nucleon collisions.

The essence of the NUCFRG code is that the mass removal ΔA from a projectile of mass A_P by collision with a target of mass A_T is a function of the impact parameter b for arbitrary target nuclei. In the abrasion-ablation fragmentation model[16], the projectile nuclei, moving at relativistic speeds, collide with stationary target nuclei. In the abrasion step, nucleons are removed by direct knockout in the overlap region of colliding nuclei. The highly excited remaining projectile piece continues its trajectory with essentially its precollision velocity and subsequently deexcites by the emission of gamma radiation and/or nuclear particles. This step is the ablation stage. The NUCFRG code calculates the average excitation from frictional forces at the interface of the interaction zone and an empirical correction to the surface energy for highly misshapen nuclei[38]. The frictional forces are derived from two-body collisional processes, and the corresponding excitation energy is a fluctuating variable. The average frictional force is generated by a random

Reproduced with permission of the copyright owner. Further reproduction prohibited without permission.

variable[30] and assumed to fluctuate between its maximum and minimum values with equal probability. Only nuclear radii are determined with the root-mean-square radius obtained from experiment for mass ≤ 26, and from parameterized experimental values for mass > 26.

At a given impact parameter *b*, there is a distance of closest approach *r* for which the interaction takes place, which one obtains from[17]

$$b^2 = r(r - r_m) \tag{2.19}$$

where r_m is the distance of closest approach for zero impact parameter. If *r* is large, the interaction is dominated by Coulomb excitation. At smaller distances, the overlap of the uniform spheres of colliding nuclei (nuclear densities) strongly interacts and mass is removed from the projectile and target.

The total number of nucleons removed through the abrasion-ablation process is given as a function of the impact parameter *b* as[16]

$$\Delta A = \Delta_{\mathrm{abr}}(b) + \Delta_{\mathrm{abl}}(b) \tag{2.20}$$

The impact parameter is related to the impact separation *r* for a Coulomb trajectory[16] in equation (2.19). For a Coulomb trajectory, the kinetic energy of the projectile is decreased as energy is given up to released nucleons in the collision event by assuming that 10 MeV is the average binding energy. The nuclear fragmentation cross sections are approximated according to the abrasion-ablation model of Bowman, Swiatecki, and Tsang[39]. The abrasion-ablation cross section for removal of ΔA nucleons, $\sigma(\Delta A)$, is[39]

$$\sigma(\Delta A) = \pi b_2^2 - \pi b_1^2 \tag{2.21}$$

Reproduced with permission of the copyright owner. Further reproduction prohibited without permission.

where b_2 is the impact parameter for which the volume of intersection of the projectile contains Δ_{abr} nucleons and the resulting excitation energies release an additional Δ_{abl} nucleons at the rate of one nucleon for every 10 MeV of excitation[17]. The charge distributions of the final projectile fragments are strongly affected by nuclear stability. The Rudstam[40] charge distribution formula for a given $\sigma(\Delta A)$ with a calculated normalization constant is used to calculate the nuclear fragmentation cross section for a specific fragment.

The charge of the nucleons removed, ΔZ, is calculated according to charge conservation[41]

$$Z_P = Z_F + \Delta Z \tag{2.22}$$

and is divided among the nucleons and light nuclei (^{2}H, ^{3}H, ^{3}He, and ^{4}He) produced by the interaction. The abraded nucleons are those removed from that portion of the projectile in the overlap region with the target. Therefore, the charge removed by abrasion is assumed to be proportional to the charge fraction of the projectile nucleus as[16]

$$Z_{\text{abr}} = Z_P \frac{\Delta_{\text{abr}}}{A_P} \ . \tag{2.23}$$

The charge release in the ablation is then[16]

$$Z_{\text{abl}} = \Delta Z - Z_{\text{abr}} \ . \tag{2.24}$$

Because of the unusually tight binding of the alpha-particle, helium production is maximized in the ablation process[41]

$$N_\alpha = \left\{ \text{Int}\left(\frac{Z_{\text{abl}}}{2}\right), \text{Int}\left(\frac{A_{\text{abl}}}{4}\right) \right\}_{\text{min}} \tag{2.25}$$

Reproduced with permission of the copyright owner. Further reproduction prohibited without permission.

where Int(x) denotes the integer part of x. The other light nuclides are likewise maximi5ed from the remaining ablated mass and charge in the order of decreasing binding energy. The number of protons produced is given by charge conservation as[41]

$$N_p = Z_{\text{abl}} - \sum_{i=2,3,4} Z_i N_i \ . \tag{2.26}$$

Similarly, the number of neutrons produced is given by mass conservation as[41]

$$N_n = A_{\text{abl}} - N_p - \sum_i A_i N_i \tag{2.27}$$

where i ranges over all the mass 2,3, and 4 ablated particles.

For the central collisions, the projectile disintegration is assumed to be nucleons if $R_P < R_T$, where R_P (R_T) is the projectile (target) radius, so that[30]

$$N_p = Z_P$$

and

$$N_n = A_P - Z_P \ .$$

Otherwise it is ignored.

Fragmentation contributions from electromagnetic dissociation (EMD) processes are considered for single nucleon removal[30]. In EMD, the virtual photon field of the target nucleus interacts electromagnetically with constituents of the projectile to cause excitation and eventual breakup[30].

The calculation is performed for $\Delta A = 1$ to $\Delta A = A_P - 1$. The results are input databases for transport codes (a nonperturbative Green's function code, GRNTRN[31]; and a galactic cosmic radiation code, HZETRN[18]).

Reproduced with permission of the copyright owner. Further reproduction prohibited without permission.

2.2.3 Modeling of Realistic Ion Beam Transport with a Nonperturbative Green's Function

A heavy-ion transport code including a database has been provided for laboratory ion beam applications as an analytic solution to the heavy-ion transport equation in terms of a Green's function representing nuclear and atomic/molecular processes. Results based on the new code were compared with perturbation theory results[31], which previously had been compared with those of ^{20}Ne transport experiments at the Lawrence Berkeley Laboratory (LBL) BEVALAC accelerator[26, 27]. In the LBL comparison, the primary errors in the computation were attributed to the nuclear cross sections and the approximations used in applying acceptance functions[31]. The perturbation code was converted to access the NUCFRG database[30, 42], then a direct comparison between the perturbation code and the nonperturbative Green's function code was made[31]. In this comparison, the sequence of perturbation terms appeared to be converging toward the nonperturbative result even though the lighter fragments did not converge in the first three perturbation terms[31]. The nonperturbative Green's function code eliminates the need to control truncation and discretization errors[29].

For multiple charged ions, the Boltzmann equation may be reduced to[23]

$$\left[\frac{\partial}{\partial x}-\frac{\partial}{\partial E}\tilde{S}_j(E)+\sigma_j\right]\phi_j(x,E)=\sum_k \sigma_{jk}\phi_k(x,E), \tag{2.28}$$

Reproduced with permission of the copyright owner. Further reproduction prohibited without permission.

where σ_{jk} is the macroscopic cross section for the collision of ion type k to produce an ion of type j. σ_{jk} is obtained from the NUCFRG database[41] and equivalent to $m_{jk}\sigma_k$ in equation (2.1).

The solution to equation (2.28) is found subject to the boundary condition

$$\phi_j(0,E) = f_j(E). \tag{2.29}$$

For this boundary condition, laboratory beams have only one value of j for which $f_j(E)$ is not zero. The function, $f_j(E)$, is described by a mean energy E_0, and an energy spread, σ, such that[28]

$$f_j(E) = \frac{1}{\sqrt{2\pi}\,\sigma}\exp\left[-\frac{(E-E_0)^2}{2\sigma^2}\right]. \tag{2.30}$$

The usual method of solution is to solve equation (2.28) as a perturbation series. In practice, the computational requirements limit the usefulness of the technique for deep penetration where many higher order terms are required[29].

A Green's function (G_{jm}) is introduced[31] as a solution of

$$\left[\frac{\partial}{\partial x} - \frac{\partial}{\partial E}\tilde{S}_j(E) + \sigma_j\right]G_{jm}(x,E,E_0) = \sum_k \sigma_{jk}G_{km}(x,E,E_0) \tag{2.31}$$

subject to the boundary condition

$$G_{jm}(0,E,E_0) = \delta_{jm}\delta(E-E_0). \tag{2.32}$$

The solution to equation (2.31) is given by superposition as[31]

$$\phi_j(x,E) = \sum_k \int G_{jk}(x,E,E')f_k(E')dE' \tag{2.33}$$

If $G_{jk}(x,E,E')$ is known as an algebraic quantity, the evaluation of equation (2.32) may be accomplished by simple integration techniques and the associated errors are avoided in solving equation (2.28) numerically[6].

Reproduced with permission of the copyright owner. Further reproduction prohibited without permission.

The Green's function equations can be simplified by transforming the energy into the residual range (r_j) as

$$r_j(E) = \int_0^E \frac{1}{\tilde{S}_j(E')} dE' \qquad (2.34)$$

and defining new field functions as[43]

$$\psi_j(x, r_j) = \tilde{S}_j(E)\phi_j(x, E) \,, \qquad (2.35)$$

$$\text{ƀ}_{jm}(x, r_j, r'_m) = \tilde{S}_j(E) G_{jm}(x, E, E'), \text{ and} \qquad (2.36)$$

$$\hat{f}_j(r_j) = \tilde{S}_j(E) f_j(E) \ . \qquad (2.37)$$

The nonperturbative solution term ƀ_{jm} is given as[43]

$$\text{ƀ}_{jm}(x, r_j, r'_m) \approx e^{-\sigma_j x}\delta_{jm}\delta(x + r_j - r'_m) + \frac{\nu_j\left[g_{jm}(x) - e^{-\sigma_j x}\delta_{jm}\right]}{x(\nu_m - \nu_j)} \ . \qquad (2.38)$$

Here ν_j is the range scale factor as $\nu_j r_j = \nu_m r_m$ and defined in equation (2.5), and $g_{jm}(x)$ is obtained through the following[31]. Define $g(j)$ and g as a function of n arguments[31]

$$g(j) = e^{-\sigma_j x} , \qquad (2.39)$$

$$g(j_1, j_2, \ldots, j_n, j_{n+1}) = \frac{g(j_1, j_2, \ldots, j_{n-1}, j_n) - g(j_1, j_2, \ldots, j_{n-1}, j_{n+1})}{\sigma_{j_{n+1}} - \sigma_{j_n}} \ . \qquad (2.40)$$

Then:

$$g_{jm}(x) = \delta_{jm} g(m) + \sigma_{jm} g(j, m) + \cdots = \sum_k g_{jk}(x - y) g_{km}(y) \qquad (2.41)$$

for any positive values of x and y[31].

The approximate solution of the transformed equation (2.31) is then given by[43]

$$\psi_j(x, r_j) = e^{-\sigma_j x}\hat{f}(r_j + x) + \sum_m \frac{\nu_j\left[g_{jm}(x) - e^{-\sigma_j x}\delta_{jm}\right]}{x(\nu_m - \nu_j)} \times \left[\hat{F}_m(r'_{mu}) - \hat{F}_m(r'_{ml})\right] . \qquad (2.42)$$

In equation (2.42), r'_{ml} and r'_{mu} are given by lower and upper limits of residual range for a proton or neutron removal[43]. The symbol $\hat{F}_m(r'_m)$ refers to the integral spectrum[43]

$$\hat{F}_m(r'_m) = \int_{r'_m}^{\infty} \hat{f}_m(r) dr . \qquad (2.43)$$

This is further defined as[43]

Reproduced with permission of the copyright owner. Further reproduction prohibited without permission.

$$\hat{F}_m(r'_m) \equiv F_m(E') \tag{2.44}$$

with

$$F_m(E') = \int_{E'}^{\infty} f_m(E)dE \tag{2.45}$$

and

$$r'_m = \int_0^{E'} \frac{dE}{\tilde{S}_m(E)} . \tag{2.46}$$

Note that the computational procedures are affected by the number of elements in equation (2.41). The number of terms in the application of equation (2.41) increases as N^2, where N is the number of isotope fields represented in the solution given by equation (2.42). For computational efficiency, the number of isotopes is minimized without greatly compromising the accuracy of the solution. The effects on isotope selections are studied for an adequate laboratory ion beam simulation by using a nonperturbative Green's function code[31].

Reproduced with permission of the copyright owner. Further reproduction prohibited without permission.

2.2.4 Modeling of Galactic Cosmic Radiation Transport with a Marching Procedure

To predict the propagation and interactions of the deep space nucleons and heavy ions through various media, the Langley Research Center galactic cosmic ray (GCR) transport code, HZETRN[18], is used. This code includes the transport of high-energy heavy ions up to atomic number 28 and solves the fundamental Boltzmann transport equation (2.1). The solution method uses a combination of analytic and numerical tools. The GCR transport problem is transformed to an integral along the characteristic fluence curve of that particular ion. As a result of the conservation of velocity in fragmentation, the perturbation series is replaced by a simple numerical procedure.

For the purpose of solving the fundamental Boltzmann transport equation (2.1), a method of characteristic solution[18] defines the coordinates as

$$\eta_j \equiv x - r_j(E) \quad \text{and} \tag{2.47}$$

$$\xi_j \equiv x + r_j(E), \tag{2.48}$$

where η_j varies along the particle path and ξ_j is constant along the particle trajectory[18].

The new fluence functions are taken as[18]

$$\chi_j(\eta_j, \xi_j) \equiv \tilde{S}_j(E)\phi_j(x,E) = \psi_j(x, r_j(E)) \tag{2.49}$$

$$\bar{\chi}_k(\eta_j, \xi_j) \equiv \chi_k(\eta_k, \xi_k) \tag{2.50}$$

$$\eta_j + \xi_j = \eta_k + \xi_k \tag{2.51}$$

Reproduced with permission of the copyright owner. Further reproduction prohibited without permission.

$$\eta_j - \xi_j = \frac{\nu_k}{\nu_j}(\eta_k - \xi_k) \tag{2.52}$$

With this coordinate, equation (2.1) becomes

$$\left[2\frac{\partial}{\partial\eta_j} + \sigma_j\right]\chi_j(\eta_j, \xi_j) = \sum_k m_{jk}\sigma_k\frac{\nu_j}{\nu_k}\chi_k(\eta_j, \xi_j) \tag{2.53}$$

where σ_j is assumed to be energy independent. By using line integration with an integrating factor[18] and defining

$$\psi_j(x, r_j) = \chi_j(\eta_j, \xi_j)\,, \tag{2.54}$$

where we have dropped the argument E of $r_j(E)$. A valid solution of equation (2.1) is[18]

$$\psi_j(x, r_j) = \exp(-\sigma_j x)\psi_j(0, r_j + x) + \int_0^x dz\, \exp(-\sigma_j z)\sum_k m_{jk}\sigma_k\frac{\nu_j}{\nu_k}\psi_k(x - z, r_k + \frac{\nu_j}{\nu_k}z)\ . \tag{2.55}$$

Equation (2.55) provides a means of propagating the boundary conditions to an interior region of small distance x and may be used in successive cycles to propagate to any arbitrary distance $x+h$. For given values of the solution at x, the values at $x+h$ are taken as[18]

$$\psi_j(x + h, r_j) = \exp(-\sigma_j h)\psi_j(x, r_j + h) +$$

$$\int_0^h dz\, \exp(-\sigma_j z)\sum_k m_{jk}\sigma_k\frac{\nu_j}{\nu_k}\psi_k(x + h - z, r_k + \frac{\nu_j}{\nu_k}z)\,. \tag{2.56}$$

This is further approximated by[18]

$$\psi_j(x + h, r_j) = \exp(-\sigma_j h)\psi_j(x, r_j + h) +$$

$$\sum_k m_{jk}\sigma_k\frac{\nu_j}{\nu_k}\left[\frac{\exp(-\sigma_j h) - \exp(-\sigma_k h)}{\sigma_k - \sigma_j}\right]\psi_k(x, r_k + \frac{\nu_j}{\nu_k}h)\ . \tag{2.57}$$

This is a marching procedure which can be continued indefinitely to greater depths within the material. Equation (2.57) is the basis of the numerical method. The method requires a simple numerical interpolation in one variable and a single summation. The basic step size in h is taken as 1 g/cm^2.

Reproduced with permission of the copyright owner. Further reproduction prohibited without permission.

2.2.5 LET Distribution

The unit of dosage in radiation protection is the sievert (Sv) which is equal to the dose in gray (Gy), which is defined as 1 J kg^{-1}, multiplied by the relative damage done by a specific kind of radiation. The latter quantity depends on several factors.

In radiobiology, the most important factor is the density of ionization. This for an individual charged particle is simply its stopping power $S_j(E)$, or for neutrals and secondaries one uses by the linear energy transfer or LET, the average energy deposited per unit length, possibly in gm/cm^2. Thus, the biological response or risk to radiation exposure is assumed to be related to the energy absorbed per unit mass within a macroscopic volume of the biological material[44]. For the same energy deposited, high-LET radiations as contrasted to radiations of low-LET such as X-rays, γ-rays, and β-rays, produce localized heavy damage which is clearly as important determinant of long term biological response. Although an LET-dependent relative biological effectiveness (RBE) is useful for charged particles of relatively low kinetic energy, there are great concerns for the biological effects of high charge and energy (HZE) ions in deep space caused by the lateral spread of high energy deposition. Cross sections for such interactions can be larger than the geometric cross section due to the secondary electrons produced along the path of the energetic ion[45]. Even though this limits LET concepts to low charge and low

Reproduced with permission of the copyright owner. Further reproduction prohibited without permission.

energy particles, LET is still an important rough indicator for HZE particles as well. A linear energy transfer distribution is a guide in assessing biologically significant components.

Techniques to generate LET distribution have been clearly described in the analysis of shielding for protection of biological and electronic equipment by Wilson and Badavi[46]. From the flux of particles with energy E, $\phi_E(E)\,dE$, the flux of particles with LET, $\phi_L(L)\,dL$, is defined as[46]

$$\phi_L(L) = \left|\frac{dL}{dE}\right|^{-1} \phi_E(E) \tag{2.58}$$

where L is as a function of E, and $|dL/dE|^{-1}$ is the Jacobian between E and L spaces. $\phi_L(L)$ has a singularity at dL/dE=0, so that it is defined on open intervals as[46]

$$\phi_L(L) = \sum_B \left|\frac{dL}{dE}\right|_B^{-1} \phi_E(E_B) \tag{2.59}$$

where B denotes various branch functions, and E_B is the energy of each branch associated with L for all values of $L \equiv L(E_B)$. In specific applications, a representation for $\phi_L(L)$ is simplified since $L(E)$ has one maximum value and one minimum value at other than zero energy. Furthermore, $L(E)$ has continuous second derivatives allowing a Taylor series expansion as

$$L(E) \approx L(E_B) + \tfrac{1}{2}L''(E_B)(E-E_B)^2 \tag{2.60}$$

in the neighborhood of the branch limits. At the branch limit, dL/dE=0, and from equation (2.60)

$$\frac{dL}{dE_B} = L'_B - L''_B(E-E_B) = 0$$

$$L'_B = L''_B(E-E_B) \tag{2.61}$$

and

Reproduced with permission of the copyright owner. Further reproduction prohibited without permission.

$$(E-E_B)=\sqrt{2\left|\frac{(L-L_B)}{L''_B}\right|}\ . \tag{2.62}$$

From equations (2.61) and (2.62),

$$\frac{dL}{dE_B}=L'_B=L''_B\sqrt{2\left|\frac{(L-L_B)}{L''_B}\right|}=\sqrt{2\left|L''_B(L-L_B)\right|} \tag{2.63}$$

at the branch limit. Therefore,

$$\phi_L(L)\approx\phi_E(E_B)\left[\sqrt{2\left|L''_B(L-L_B)\right|}\,\right]^{-1} \tag{2.64}$$

in the neighborhood of the branch points, where the subscript B denotes evaluation at the branch limit[46].

The maximum and minimum branch points[46] are found at dL/dE=0 from the mapping of energy to LET in which a maximum LET ($L_{\max}$) occurs at a rather low energy ($E_{\max}$) and a minimum LET ($L_{\min}$) is at a high energy ($E_{\min}$) that is approximately given by an inverse dependence on the energy along the ion's trajectory. There is a gradual increase in LET toward energies beyond $E_{\min}$ because of relativistic effects. When the branch points and equations (2.58) through (2.64) are considered, the triple valued branch functions are represented by[46]

$$\{\phi_{L_i}\}_B=\left\{\left|\frac{dE}{dL}\right|\right\}_i\phi_{E_i},\ \text{where}\ E_i\in\{E_i\}_B \tag{2.65}$$

and B denotes one of the three branches. The sequence of E_i with the lower branch, $\{E_i\}_l$, is defined as those values of energy less than $E_{\max}$ at rather lower energies. The energy sequence with the main branch, $\{E_i\}_m$, is defined by $E_{\max} < E_i < E_{\min}$ and the sequence $\{E_i\}_h$ with the high branch defined as those values of energy greater than $E_{\min}$ at higher energies[46]..

Reproduced with permission of the copyright owner. Further reproduction prohibited without permission.

Since ϕ_{L_i} is unbounded near the branch limit, an extrapolation into the neighborhood of the branch limit is provided for sufficiently close E_i^{46}

$$\phi_{L_i} = \left|\frac{dE}{dL}\right|_i \phi_{E_i}$$

$$\phi_{E_i} = \left|\frac{dL}{dE}\right|_i \phi_{L_i} = \sqrt{2\left|L_B''(L_i - L_B)\right|}\,\phi_{L_i}\,. \tag{2.66}$$

Taking equation (2.66) into (2.64)

$$\phi_L(L) \approx \phi_{L_i}\sqrt{\frac{|L_i - L_B|}{|L - L_B|}} \tag{2.67}$$

where L_i is the nearest value to the branch limit L_B in the appropriate domain[46]. The numerical branch limit values of $E_{\max}$, $E_{\min}$, $L_{\max}$, and $L_{\min}$ depend on the charge and mass of the particles and are specified for each ion type in the radiation field[46]. The mapping of LET to energy is qualitatively the same triple valued function but is quantitatively different for each ion type. An important feature of the LET at the branch limits, L_B, is that the LET of all charged particles moving with the same velocity in a given absorber is proportional to the squares of their charges.

In the absence of nuclear effects, the fluence within a medium at a distance x from the boundary is[46]

$$\phi(x,E)S(E) = \phi(0,E_x)S(E_x) \tag{2.68}$$

where $\phi(x,E)$ is the fluence at a distance x within a medium, $S(E)$ is the stopping power , $\phi(0,E_x)$ is the fluence at the boundary, $S(E_x)$ is the stopping power at the boundary, and the energy E_x at the boundary is calculated from

$$R(E_x) = R(E) + x$$

$$E_x = R^{-1}[R(E) + x].$$

If the target thickness, x, is large enough, $x >> R(E)$, then $E_x = R^{-1}(x)$, so that

$$\phi(x,E)S(E) = \phi(0,E_x)S(E_x) \approx \phi[0,R^{-1}(x)]S[R^{-1}(x)]$$

Reproduced with permission of the copyright owner. Further reproduction prohibited without permission.

and the spectrum reaches an equilibrium value as[46]

$$\phi(x,E) \approx \frac{S[R^{-1}(x)]\phi[0,R^{-1}(x)]}{S(E)}. \qquad (2.69)$$

Equilibrium is achieved quickly at low energies. At high energies, nuclear effects dominate and equilibrium is not achieved. The limit of a pure equilibrium spectrum for each particle type j at all energies would be given by $\phi_E(E)S_j(E) = c$, where c is a constant value. The equilibrium differential LET spectra have been given elsewhere[46] for ions of H, He, Li, and C with the $c = 1$. Comparison of the equilibrium differential LET spectra shows that the equilibrium occurs at a higher energy loss with heavier ions. These equilibrium limits are proportional to the squares of their charges.

The integral LET spectrum is defined and related to integral energy spectra as[46]

$$\Phi(>L) = \int_L^{L_{\max}} \phi_L(L')dL' = \Phi(>E_1) - \Phi(>E_2) + \Phi(>E_3) \quad , \qquad (2.70)$$

where E_1, E_2, and E_3 are the three roots of $S(E) = L$. The integral equilibrium spectrum is given for $\xi \geq E_3$[46],

$$\Phi(>E) = c\int_E^{\xi} \frac{dE'}{L(E')} = c\Big(R(\xi) - R(E)\Big)$$

where the arbitrary value ξ is taken to be 10 GeV.

The integral LET spectrum for $\xi \geq E_3$ is then[46]

$$\Phi(>L) = c\Big(R(\xi) + R(E_2) - R(E_1) - R(E_3)\Big). \qquad (2.71)$$

For the higher-LET region only, there are two roots E_1 and E_2[46]. Then equation (2.71) is[46]

$$\Phi(>L) = \Phi(>E_1) - \Phi(>E_2) = c\int_{E_1}^{\xi} \frac{dE'}{L(E')} - c\int_{E_2}^{\xi} \frac{dE'}{L(E')} = c\Big(R(E_2) - R(E_1)\Big). \qquad (2.72)$$

From range-energy relations, the range of a particle would be roughly proportional to the square of its energy if it is nonrelativistic. Using this qualitative idea, the range at

Reproduced with permission of the copyright owner. Further reproduction prohibited without permission.

relatively much lower energy is neglected. Thus, the integral LET spectra are characteristic of the main branch of the LET curve except $L_{\max}$ as[46]

$$\Phi(>L) \approx cR(E_2) \quad , \qquad (2.73)$$

where the ion with sufficiently high velocities is stripped of all of its electrons and the LET is essentially all through electronic excitation and ionization of the stopping material. At the highest LET value ($L_{\max}$)[46],

$$\Phi(L_{\max}) = \Phi(E_{\max}) = c\int_{E_1}^{E_2} \frac{1}{S(E_{\max})} dE = \frac{c(E_2 - E_1)}{S(E_{\max})} \quad . \qquad (2.74)$$

CHAPTER 3. EXPERIMENTAL/THEORETICAL STUDIES

3.1 Introduction

The high energy heavy ion radiation components are usually attenuated to lower linear energy transfer (LET) lighter ions as a result of nuclear interactions between projectile and target nuclei. Recall that LET is proportional to the square of the ion charge. These interactions become more significant as the particles penetrate further into the shield medium. The internal radiation environment within a spacecraft structure, which interacts with onboard personnel or equipment, depends on the shield composition. This dependence is a result of differences in atomic cross sections, nuclear attenuation, and the distribution of fragmentation products in different shield materials. Calculations show that hydrogen presents the greatest cross section per unit mass[47]. It also provides the maximum energy reduction of secondary neutrons in an elastic collision, and absorbs neutrons of reduced energy. Thus, hydrogen-containing materials, such as polymers, have been chosen as subjects for the calculations. The preparation of experimental studies of the attenuation of ion beams in potential space construction materials or as a container for microelectronic devices will utilize theoretical predictions based on the current understanding.

Reproduced with permission of the copyright owner. Further reproduction prohibited without permission.

Even though ionization cross sections are much larger, monoenergetic primary particles if of sufficient energy will still suffer nuclear reactions before stopping in the shield medium. In nuclear reactions, the secondary radiations have broad distributions of secondary energies for lighter particles. The most energetic secondaries are confined in a narrow cone about the initial direction and are closely confined to the initial beam axis over at least the first mean-free path[6]. This cone narrows with increasing primary energy. The flux of each secondary radiation with a broad energy distribution is integrated numerically to obtain the total ion fluence by using equation (2.18). These total ion fluences are then compared for different materials as discussed in section 3.3.1.

A heavy-ion transport code including a database[31] has been used. This code has been used for the ion beam applications described here. A Green's function technique obtains an analytic solution of the heavy-ion transport equations, equation (2.42). A fragmenting iron ion produces hundreds of isotopes as a result of its nuclear reactions. These isotopes are represented in the solution of the transport problem. Only a hundred or so such isotopes contribute to the solution in a significant way. A reduced set of isotopes is selected to minimize the computational burden, but that introduces some error in the final result. A determination of the number of isotopes for an adequate laboratory beam simulation is required . The atomic weight taken as the nearest integral value and the charge associated with each field function are truncated to the nearest isotope using a weighted square-distance method. A minimum list of 122 isotopes is required for an adequate representation of the mass and charge distributions of the secondary radiation

Reproduced with permission of the copyright owner. Further reproduction prohibited without permission.

fields. A reduced set of 80 isotopes is sufficient to represent the charge distribution alone and represents reasonably well the linear energy transfer properties for an iron beam. The resulting 122-isotope list should be adequate for a laboratory ion beam with charges equal to or less than 26, because iron fragmentation produces nearly every isotope lighter than iron (Z = 26). This is discussed in section 3.3.2.

Reproduced with permission of the copyright owner. Further reproduction prohibited without permission.

3.2 Potential Space Construction Materials

The calculation is extended herein to complex polymer molecular structures that are hydrogen-containing materials and which may be fabricated and supplied as shield material. The model[48] of tetraglycidyl 4,4' diamino diphenyl methane (TG 4,4' DDM) epoxy cured with diamino diphenyl sulfone (DDS), is among those considered. Figure 2 shows the epoxy structure. The dashed line encloses the repeat cured unit. Table 1 contains the values of the atomic parameters for the pure epoxy tested. The density of the epoxy is 1.32 g/cm^3.

For more specific extended-duration lunar missions, a lunar-soil model by Nealy, Wilson, and Townsend[49] is used to predict the fluxes of energetic galactic cosmic rays in the internal environment after passing through a thick lunar regolith shield. In the case of a lunar-soil model, the five most abundant elements, comprising up to 99.9 percent of the regolith samples, are chosen. The lunar soil composition used is that for the measured abundances of SiO_2, Al_2O_3, FeO, and MgO and has the elemental percentage given by Nealy, Wilson, and Townsend[49]. Table 2 contains the values of the atomic parameters for lunar regolith. The average soil mass density, 1.5 g/cm^3, is used based on the density range of 0.8 to 2.15 g/cm^3 reported before. Table 3 contains the values of the atomic parameters for lunar regolith/epoxy composites.

Reproduced with permission of the copyright owner. Further reproduction prohibited without permission.

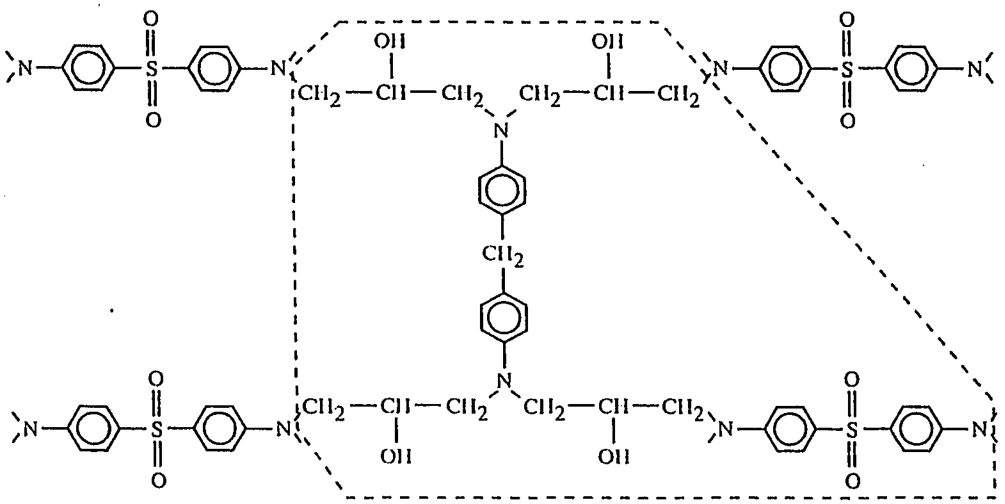

Figure 2. Tetraglycidyl 4,4' diamino diphenyl methane epoxy cured with diamino diphenyl sulfone

Reproduced with permission of the copyright owner. Further reproduction prohibited without permission.

Table 1. Values of atomic parameters for the pure epoxy, ρ=1.32 g/cm^3

Parameters	Hydrogen	Carbon	Nitrogen	Oxygen	Sulfur
Atomic Number, Z	1	6	7	8	16
Mass Number, A	1	12	14	16	32
Number of Atoms in Each Repeat Unit	42	37	4	6	1
Weight in Each Repeat Unit	42	444	56	96	32
Atom Density, 10^{22} atoms/gm	3.77	3.32	0.36	0.54	0.09

Reproduced with permission of the copyright owner. Further reproduction prohibited without permission.

Table 2. Values of atomic parameters for the lunar regolith, $\rho=1.5$ g/cm^3

Parameters	Oxygen	Silicon	Aluminum	Iron	Magnesium
Atomic Number, Z	8	14	13	26	12
Mass Number, A	16	28	27	56	24
Normalized Weight Percentage	44.7 %	24.5 %	9.3 %	15.4 %	6.0 %
10^{21} Atoms/gm	23.1	4.15	1.67	0.66	1.38

Reproduced with permission of the copyright owner. Further reproduction prohibited without permission.

Table 3. Values of atomic parameters for the lunar regolith/epoxy composites, where

ρ_f=1.5 g/cm^3 and ρ_e=1.32 g/cm^3

			Atom Density, 10^{21} Atoms/gm	
Elements	Atomic Number, Z	Mass Number, A	W_t=0.1 Epoxy, ρ_c=1.48 g/cm^3	Wt=0.2 Epoxy, ρ_c=1.46 g/cm^3
H	1	1	3.78	7.53
C	6	12	3.32	6.65
N	7	14	0.36	0.72
O	8	16	0.54	19.57
S	16	32	0.09	0.18
Si	14	28	3.74	3.32
Al	13	27	1.51	1.34
Fe	26	56	0.59	0.53
Mg	12	24	1.24	1.1

Reproduced with permission of the copyright owner. Further reproduction prohibited without permission.

Several polymers were tested with the calculations to gauge their effectiveness as shield materials: an aromatic polyether, polysulfone P1700[50] from the Union Carbide Corporation, which is an amorphous, rigid, tough thermoplastic with a high second-order transition (T_g) and noteworthy electrical properties; a commercial polyetherimide, Ultem[51] from the General Electric Company, which has an unusually high melting point and possess outstanding thermal stability, but is intractable; and a polypyromellitimide, Kapton[52], a thermoset from the du Pont Corporation which has excellent thermal, oxidative, and hydrolytic stability. Films of Kapton with a thickness of 2.0 mils have shown outstanding resistance to irradiation from high energy electrons and from thermal neutrons[52]. The repeat units of these polymers are shown in figure 3. Polyethylene, with its high hydrogen density, and polytetrafluoroethylene, with heavier fluorine atoms and no hydrogen, were tested. Table 4 contains the values of the atomic parameters for the pure polymers.

The addition of boron powder to a polymer allows the material to absorb low-energy neutrons[53]. This occurs because neutrons, when reduced to very low energies, have a high probability of reacting with a nucleus in a process called neutron capture. Neutron thermalization is a natural consequence of movement through hydrogen bearing polymers. Low energy neutrons react particularly well with a stable isotope of boron, ^{10}B, which constitutes 19.6 percent of the naturally-occurring element. The products of the reaction, ^{4}He and ^{7}Li, are not radioactive. Thus, various weight fractions of boron in films of some of these polymers were tested. Table 5 contains the values of the atomic

Reproduced with permission of the copyright owner. Further reproduction prohibited without permission.

parameters for the polymer/boron mixtures. The density of natural boron powder was taken as 2.59 g/cm^3.

Reproduced with permission of the copyright owner. Further reproduction prohibited without permission.

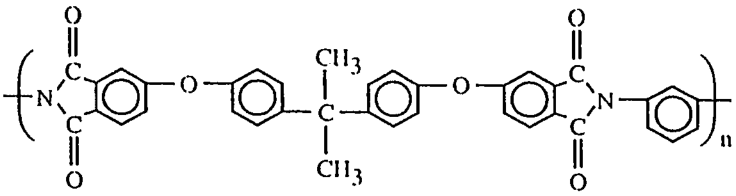

(a) Polyetherimide.

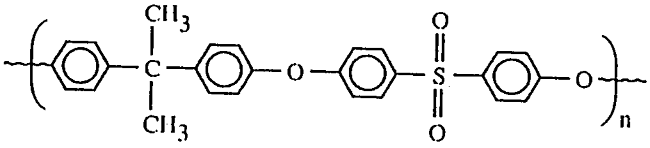

(b) Polysulfone.

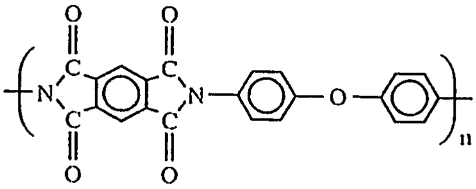

(c) Polyimide.

Figure 3. The repeat units of three polymers studied

Reproduced with permission of the copyright owner. Further reproduction prohibited without permission.

Table 4. Values of atomic parameters for some polymers

	Elements	Atomic Number, Z	Mass Number, A	Atom Density, 10^{22} Atoms/gm	Density, g/cm^3
Polyetherimide	H	1	1	2.44	1.27
	C	6	12	3.76	
	N	7	14	0.203	
	O	8	16	0.61	
Polysulfone	H	1	1	3.0	1.24
	C	6	12	3.68	
	O	8	16	0.545	
	S	16	32	0.136	
Polyimide	H	1	1	1.58	1.42
	C	6	12	3.47	
	N	7	14	0.315	
	O	8	16	0.788	
Polyethylene	H	1	1	8.60	.92
	C	6	12	4.30	
Poly(tetrafluoro-ethylene)	C	6	12	1.20	2.17
	F	9	19	2.40	

Reproduced with permission of the copyright owner. Further reproduction prohibited without permission.

Table 5. Values of atomic parameters for various boron containing polymers

				Atom Density, 10^{21} Atoms/gm			
	Elements	Atomic No., Z	Mass No., A	5 % B	10 % B	15 % B	20 % B
Polyetherimide	H	1	1	23.2	22.0	20.7	19.5
	C	6	12	35.8	33.8	32.0	30.1
	N	7	14	1.93	1.83	1.73	1.63
	O	8	16	5.80	5.49	5.18	4.88
	B	5	11	2.23	4.46	6.69	8.93
	B	5	10	0.558	1.11	1.67	2.23
Polysulfone	H	1	1	28.6	27.0	25.5	24.1
	C	6	12	35.0	33.1	31.3	29.6
	O	8	16	5.19	4.90	4.63	4.38
	S	16	32	1.30	1.22	1.16	1.10
	B	5	11	2.11	4.46	6.66	8.76
	B	5	10	0.527	1.12	1.66	2.20
Polyimide	H	1	1	15.0	14.2	13.4	12.6
	C	6	12	33.0	31.2	29.4	27.7
	N	7	14	3.0	2.84	2.67	2.52
	O	8	16	7.52	7.10	6.69	6.31
	B	5	11	2.15	4.46	6.82	8.9
	B	5	10	0.538	1.12	1.7	2.23

Reproduced with permission of the copyright owner. Further reproduction prohibited without permission.

3.3 Laboratory Ion Beams on Shield Materials

3.3.1 Total Ion Fluence Comparisons

Two ion beams were used in the calculations: ^{56}Fe at 605 MeV/amu and ^{20}Ne at 425 MeV/amu. These beams and energies were chosen because they matched experimental data taken at the Lawrence Berkeley Laboratory (Thibeault, S. A., private communication). An initial range of the primary ion beam, to which the primary ion of initial energy can be extended from the boundary, for a material with known density is calculated by using the Bethe formula[34] where the linear energy transfer is quite accurate at high energy. The initial range of penetration of the 605 MeV/amu ^{56}Fe beam in lunar regolith of density 1.5 g/cm^3 is approximately 10 cm (15.8 g/cm^2). The calculations show that lighter fragments of the incident ^{56}Fe nuclei with energies lower than 605 MeV/amu are predicted to be in high abundance for a lunar regolith brick of thickness 16 g/cm^2 which is slightly larger than the range of penetration. Figure 4 shows the distribution of these fragments as they appear at the back of the shield. Note that the addition of hydrogen-bearing epoxy to the regolith brick increases the protection. Figure 5 shows that lighter particles with energies lower than 605 MeV/amu also are predicted to be present for a lunar regolith brick of thickness 18 g/cm^2. These results demonstrate that most of these particles are secondaries from the nuclear interaction processes. Most

Reproduced with permission of the copyright owner. Further reproduction prohibited without permission.

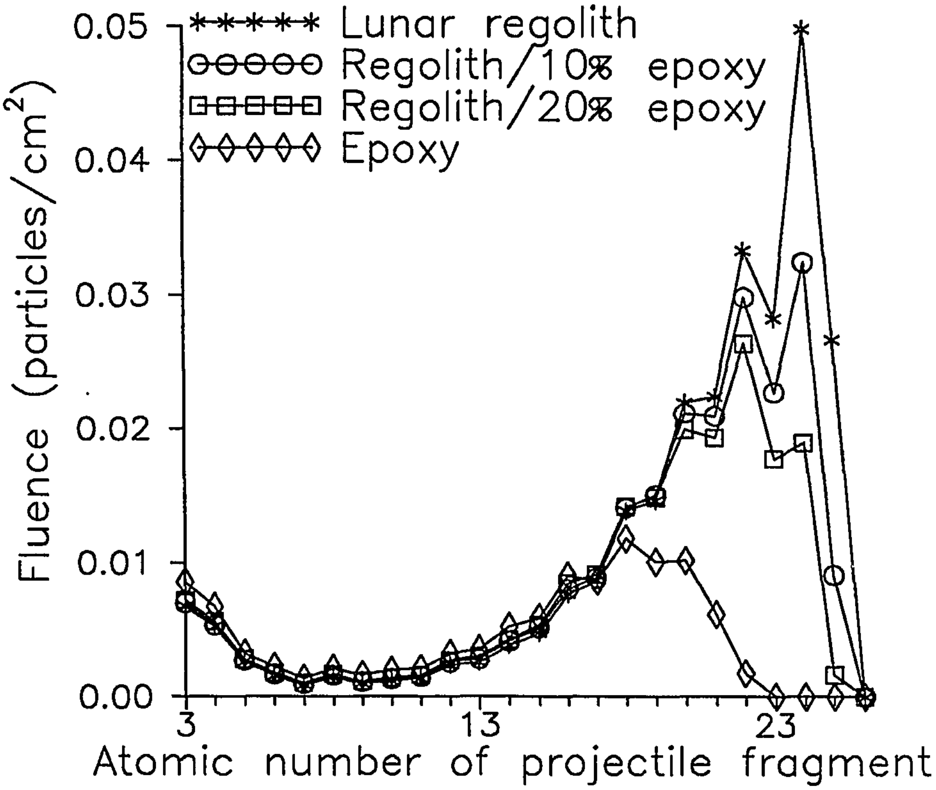

Figure 4. Attenuation of 605 MeV/amu iron beams in lunar construction materials (16 g/cm^2)

Reproduced with permission of the copyright owner. Further reproduction prohibited without permission.

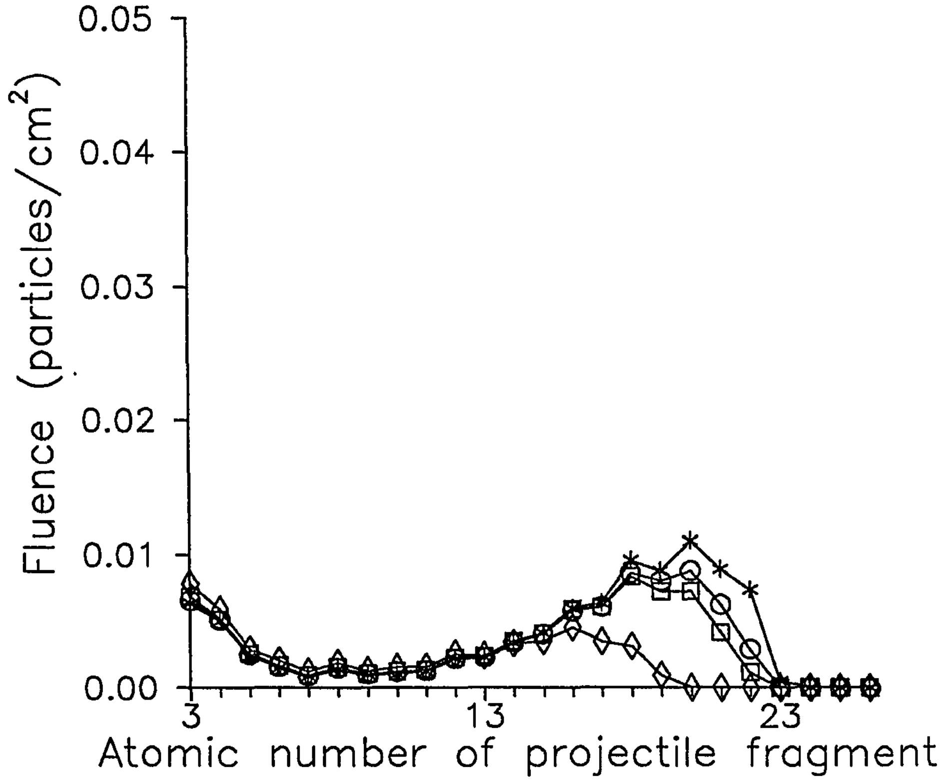

Figure 5. Attenuation of 605 MeV/amu iron beams in lunar construction materials (18 g/cm^2)

Reproduced with permission of the copyright owner. Further reproduction prohibited without permission.

conspicuous is that the maximum contribution comes from a broad range of particles above Z = 3 (Li).

The calculated initial range of the primary beams of ^{56}Fe at 605 MeV/amu and ^{20}Ne at 425 MeV/amu for each polymer are shown in table 6. Table 6 also shows the effects of adding boron to three of the polymers. From these calculated initial ranges, a thickness of 10 g/cm^2 is considered to be a thin target and 18 g/cm^2 is a thick target for a primary ^{56}Fe beam at 605 MeV/amu, while 18 g/cm^2 and 20 g/cm^2 are considered to be a thin and a thick targets respectively for a primary ^{20}Ne beam at 425 MeV/amu. The fluences of identified projectile fragment nuclei are compared for thick targets of the primary ^{56}Fe beam at 605MeV/amu, and the primary ^{20}Ne beam at 425 MeV/amu where the thicknesses are slightly larger than the initial ranges.

The mean free paths for nuclear reaction and the nature of the reaction products may be determined from nuclear cross section data. Energetic incident particles have short mean free paths for nuclear reaction in hydrogen targets, because a hydrogenous material has larger nuclear absorption cross sections per unit mass than a non-hydrogen material[47]. The charge removal from a projectile by fragmentation with hydrogen targets is smaller than that with non-hydrogen targets[54]. Due to the greater hydrogen content of polyethylene, the charge difference of projectile by fragmentation in polyethylene is smaller than that in polytetrafluoroethylene and other polymers. Thin polyethylene enhances the high Z fragment when it is compared with the other thin polymers. The

Reproduced with permission of the copyright owner. Further reproduction prohibited without permission.

Table 6. The calculated initial range for some polymers and polymers with varying weight percentages of boron.

	ρ (g/cm^3)	Initial Range of ^{56}Fe Beam at 605 MeV/amu, (g/cm^2)	Initial Range of ^{20}Ne Beam at 425 MeV/amu, (g/cm^2)
Pure Polyetherimide	1.27	13.8	19.2
5 % B	1.30	13.9	19.3
10 % B	1.33	14.0	19.5
15 % B	1.36	14.0	19.6
20 % B	1.40	14.1	19.7
Pure Polysulfone	1.24	13.7	19.1
5 % B	1.27	13.8	19.2
10 % B	1.30	13.9	19.3
15 % B	1.34	14.0	19.5
20 % B	1.37	14.0	19.5
Pure Polyimide	1.42	14.1	19.6
5 % B	1.45	14.1	19.7
10 % B	1.48	14.2	19.8
15 % B	1.51	14.3	19.9
20 % B	1.54	14.4	20.0
Polyethylene	0.92	12.2	
Poly(tetrafluoroethylene)	2.17	15.7	

Reproduced with permission of the copyright owner. Further reproduction prohibited without permission.

second and further fragmentation events occur more often in the thicker polyethylene shields because of the higher nuclear attenuation rate in polyethylene than in the other polymer shields. The charge difference from the second and further collisions greatly reduces the fluence of HZE fragments emitted from the back side of a polyethylene shield.

The lighter material such as polyethylene enhances the high energy heavy fragment fluence relative to polytetrafluoroethylene for thin shields as shown in figure 6 and reduces the fluence more efficiently than polytetrafluoroethylene and other polymers for thick shields as shown in figure 7. In fact, the succession of curves in figures 6 and 7 are governed by the amount of hydrogen per unit mass and polyethylene is the most abundant in hydrogen. Study on the effect of shield composition on the LET distribution at several depths has already shown that for the radiation distributions observed at solar minima[54] polyethylene is the most effective high-LET degrader at thicknesses greater than 5g/cm^2. Here too, polyethylene is the most effective shield material among several polymers at a thickness greater than 18 g/cm^2 for a ^{56}Fe beam at 605 MeV/amu.

The addition of boron powder to a polymeric material causes no degradation in glass transition temperature or Young's modulus[53]. The calculated fluence for a polyetherimide containing various weight fractions of boron is shown in figure 8 for a ^{56}Fe beam at 605 MeV/amu, and in figure 9 for a ^{20}Ne beam at 425 MeV/amu. These results show no significant difference for various weight fractions of boron. For thick shields, the pure polymer shows slightly better attenuation of fragments of charge greater than 3 than

Reproduced with permission of the copyright owner. Further reproduction prohibited without permission.

does a mixture containing 20 % boron. As the fraction of B increases from 5 % to 20 % by weight, both the density and the initial range increase because boron has a higher atomic number than hydrogen. Similar results are obtained for the polysulfone and the polyimide. Hence, pure polymers are expected to attenuate fragments of charge greater than 3 slightly better than materials containing various fractions of boron. The laboratory code with perturbation theory does not include light fragments of $Z < 3$ in any realistic way, because a greater knowledge of nuclear fragmentation processes and a corresponding transport theory are required for these fragments.

Reproduced with permission of the copyright owner. Further reproduction prohibited without permission.

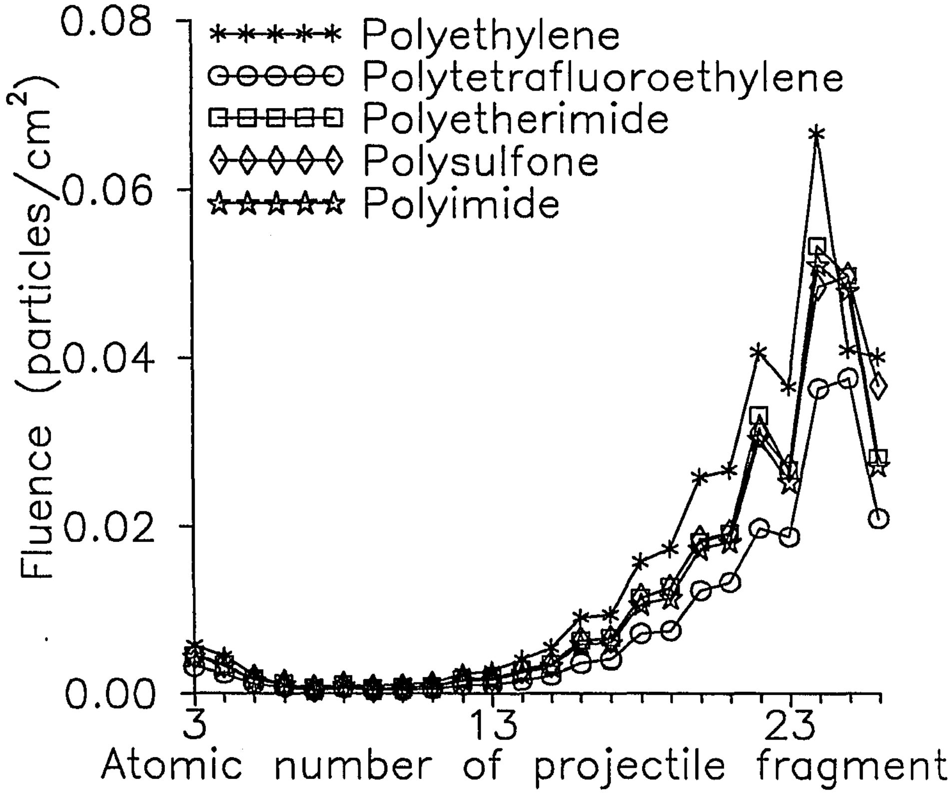

Figure 6. Attenuation of 605 MeV/amu iron beams in various polymer construction materials (5 g/cm^2)

Reproduced with permission of the copyright owner. Further reproduction prohibited without permission.

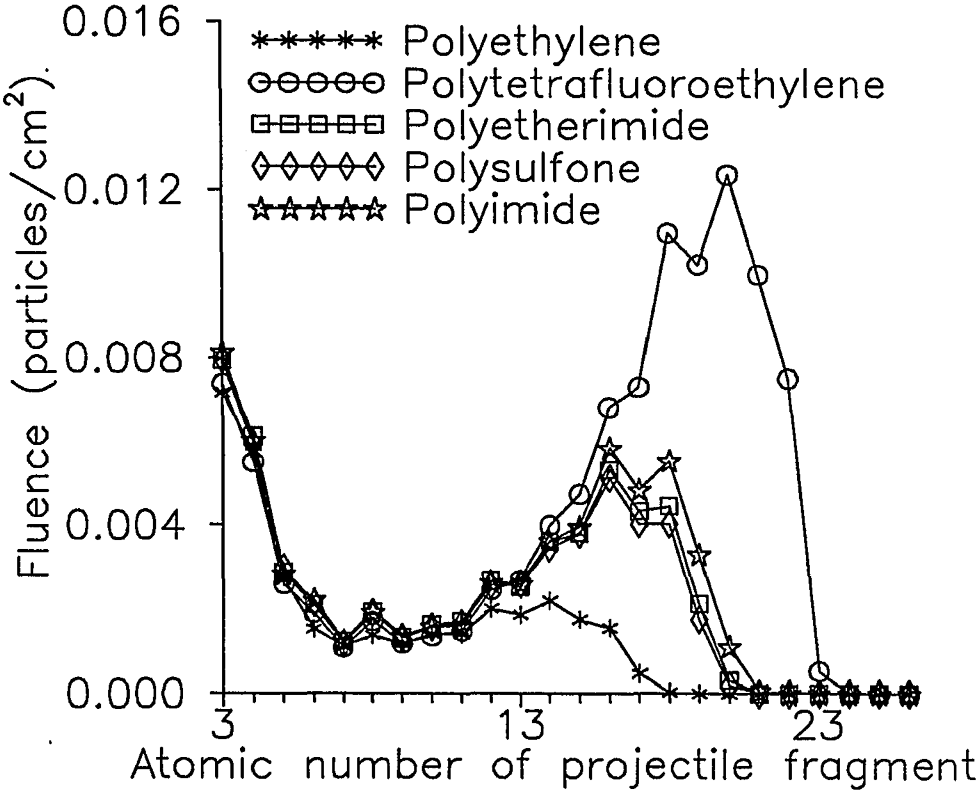

Figure 7. Attenuation of 605 MeV/amu iron beams in various polymer construction materials (18 g/cm^2)

Reproduced with permission of the copyright owner. Further reproduction prohibited without permission.

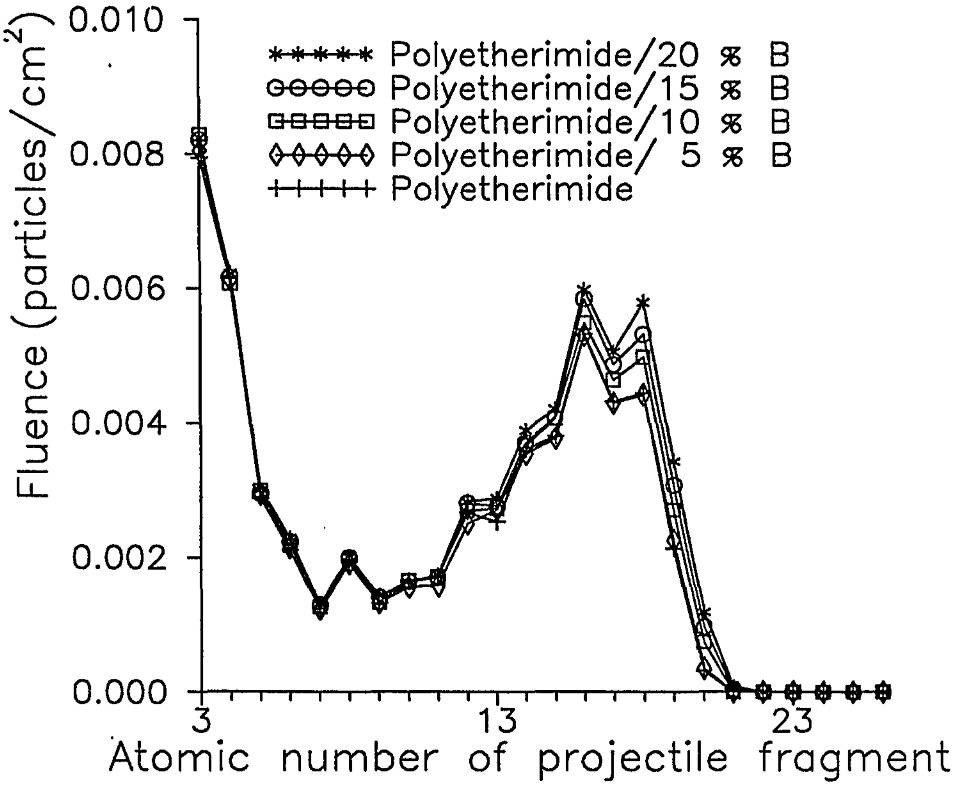

Figure 8. Attenuation of 605 MeV/amu iron beams in various weight fraction of boron-containing polyetherimide (18 g/cm^2)

Reproduced with permission of the copyright owner. Further reproduction prohibited without permission.

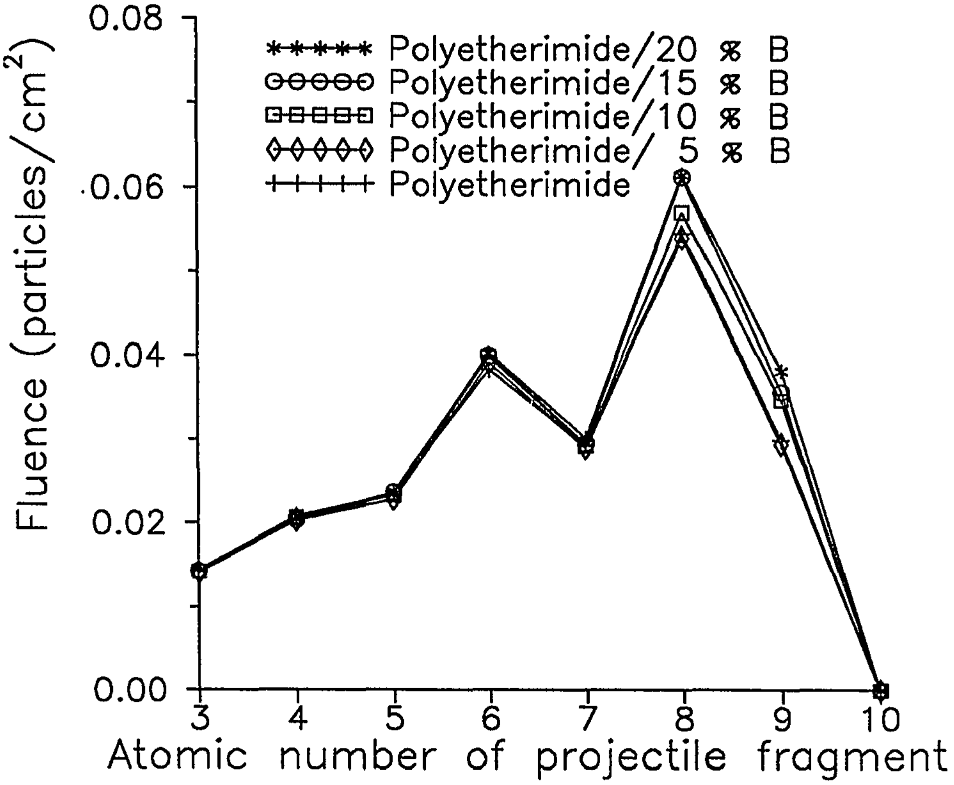

Figure 9. Attenuation of 425 MeV/amu neon beams in various weight fraction of boron-containing polyetherimide (20 g/cm^2)

Reproduced with permission of the copyright owner. Further reproduction prohibited without permission.

3.3.2 Effects on Isotope Selection

The nonperturbative method generates the Green's function for any ion of charge Z $\leq$28 that results from the impact of that ion on a material medium, including the secondary fragment fields. The atomic weight, taken as the nearest integral value, and charge associated with each field function are truncated to the nearest isotope A_l, Z_l in the isotope table. The truncation minimizes the distance to the nearest isotope using a weighted square-distance function

$$D_{il} = (A_i - A_l)^2 + 4(Z_i - Z_l)^2 \qquad (3.1)$$

where A_i, Z_i is the isotope produced in the fragmentation event. Because charge is a dominating factor for linear energy transfer, the distance is weighted more by charge than by mass to give faster convergence in equation (3.1). Clearly, the accuracy in the transport result requires the isotope list to contain the main isotopes produced in the fragmentation event. The isotopes of lesser importance may be approximated. Initially, 59 isotopes were selected to represent each nuclear mass value between 1 and 58 based on a nuclear stability curve. Such a list was found adequate for transport of galactic cosmic rays using the HZETRN code[42, 55]. However, such a representation was inadequate for transport of an iron beam using the nonperturbative code GRNTRN[31]; thus, more isotopes were added to the table. To determine the number of isotopes required for an adequate laboratory beam simulation, which has both solution accuracy and practical computation

Reproduced with permission of the copyright owner. Further reproduction prohibited without permission.

time, the solution convergence was tested with the isotope selection. The output spectra of charge and mass with an increased size of isotope table were compared to the result with a prior isotope table. When they had significant discrepancy at some charge and/or mass, more isotopes were added for the successive tables, while the lesser important isotopes, which do not contribute to the output spectra in a significant way, were omitted from the tables in order to get the practical computational efficiency. This process of selection was continued until the output spectra were converged within an insignificant error.

The total flux of identified projectile fragment nuclei between H and Fe is found for 505 MeV/amu monoenergetic ^{56}Fe beams with a 0.2 percent energy spread for the primary beam incident on an epoxy sample with a thickness of 5 g/cm^2. The resin selected is tetraglycidyl 4,4' diaminodiphenylmethane (TG 4,4' DDM) epoxy cured with diaminodiphenylsulfone (DDS). A repeat unit of the cured epoxy has a molecular formula of $C_{37}H_{42}N_4O_6S$ and has a density of 1.32 g/cm^3. An epoxy was tested because it is a common material which can be fabricated and supplied as a shield medium. The results based on tables of 59 and 80 isotopes are shown in figures 10 and 11. The integral output spectra for the projectiles and fragments in figure 10 show a somewhat similar charge distribution for both 59 and 80 isotopes, but the mass distributions in figure 11 show large differences. The 80-isotope table is probably adequate for applications in which charge is the dominating factor (e.g., linear energy transfer), but the mass distribution would be substantially improved through the use of an expanded isotope list.

Reproduced with permission of the copyright owner. Further reproduction prohibited without permission.

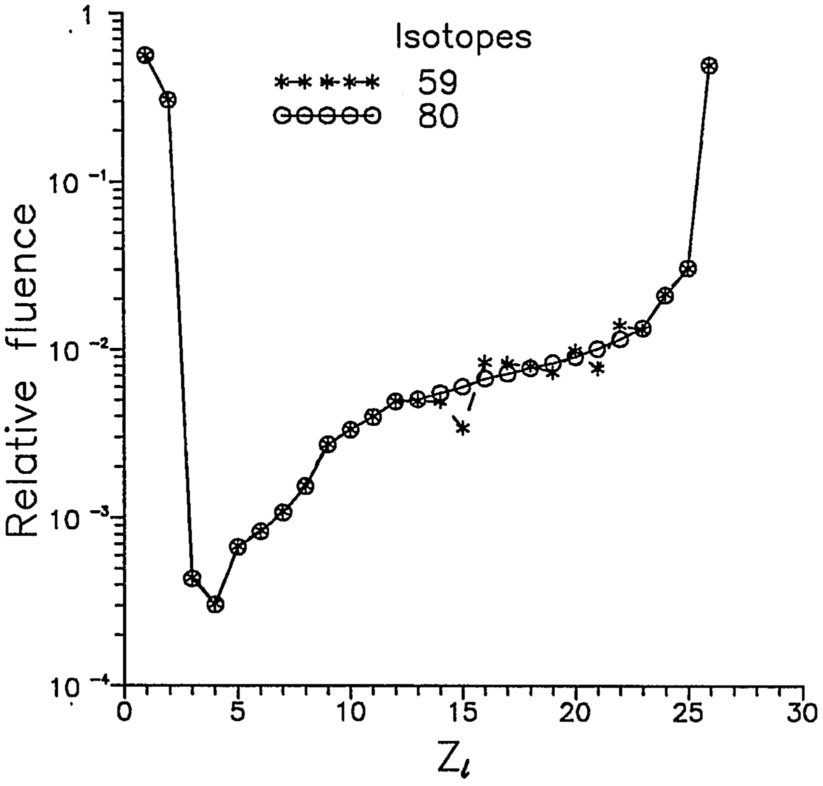

Figure 10. Convergence of charge distribution of 505 MeV/amu iron beams in 5 g/cm^2 of epoxy for 59 and 80 isotopes

Reproduced with permission of the copyright owner. Further reproduction prohibited without permission.

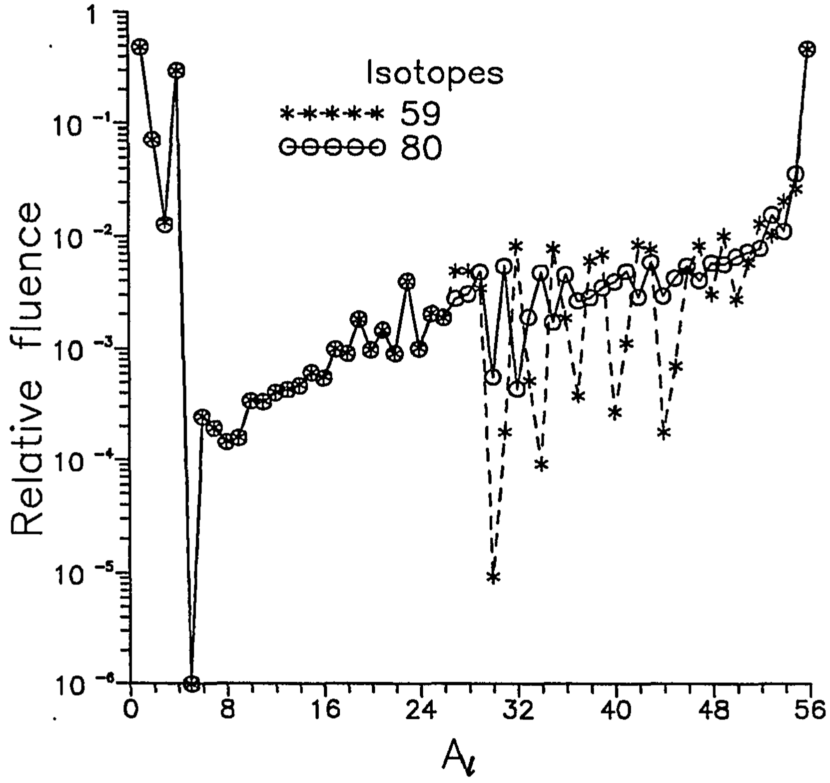

Figure 11. Convergence of mass distribution of 505 MeV/amu iron beams in 5 g/cm^2 of epoxy for 59 and 80 isotopes

Reproduced with permission of the copyright owner. Further reproduction prohibited without permission.

A modest change to the 80-isotope list was made with the addition of 5 isotopes, the results of which are shown in figure 12. Significant improvement in the mass distribution is achieved for $A_l < 40$, but the result is worse at higher mass numbers. The charge distribution was less accurate and the use of a 100-isotope list could not adequately resolve the convergence problem for the mass distribution as seen in figures 12 and 13. The isotope tables were incrementally expanded with continuous improvement in the mass distribution, as seen in figures 14 to 17. The final list of 122 isotopes appears to be the minimum set required to represent the fragment mass distribution. The charge distribution had nearly converged at 80 isotopes and no substantial change in its convergence occurs beyond 100 isotopes, as seen in figure 18.

Although the specific tests were derived for an iron beam on a given epoxy resin, the isotope distributions are largely dominated by the nuclear physics of the projectile fragments and virtually all elements are produced below the projectile atomic number. Thus, similar convergence properties are expected for other shield materials. It should be noted that iron is a principal contributor to galactic cosmic ray exposure and the current results indicate that the space shield calculations require a larger table than the 59 isotopes currently used.

Reproduced with permission of the copyright owner. Further reproduction prohibited without permission.

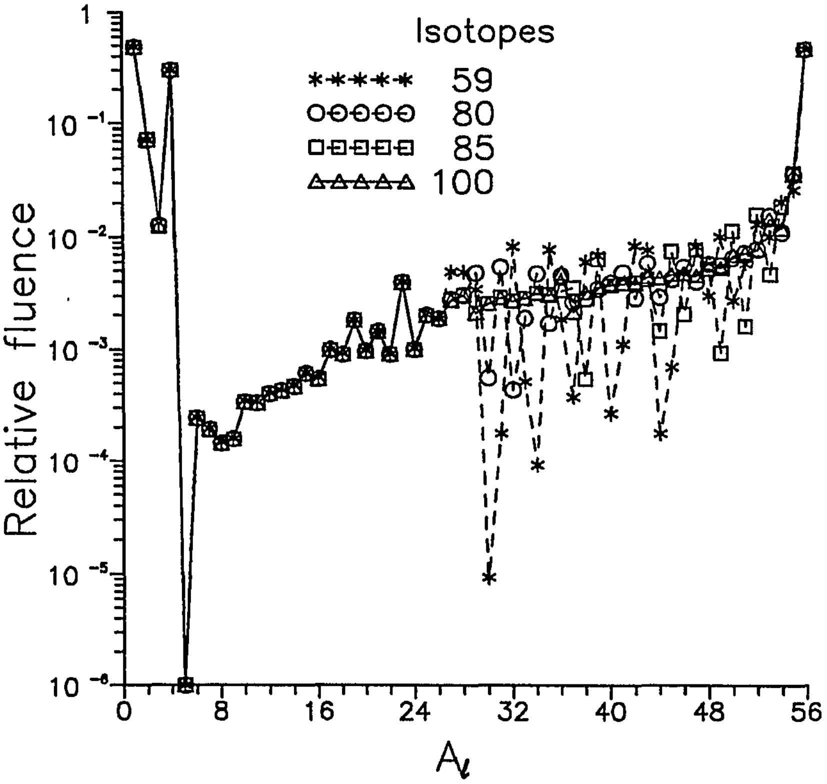

Figure 12. Convergence of mass distribution of 505 MeV/amu iron beams in 5 g/cm^2 of epoxy for 59, 80, 85, and 100 isotopes

Reproduced with permission of the copyright owner. Further reproduction prohibited without permission.

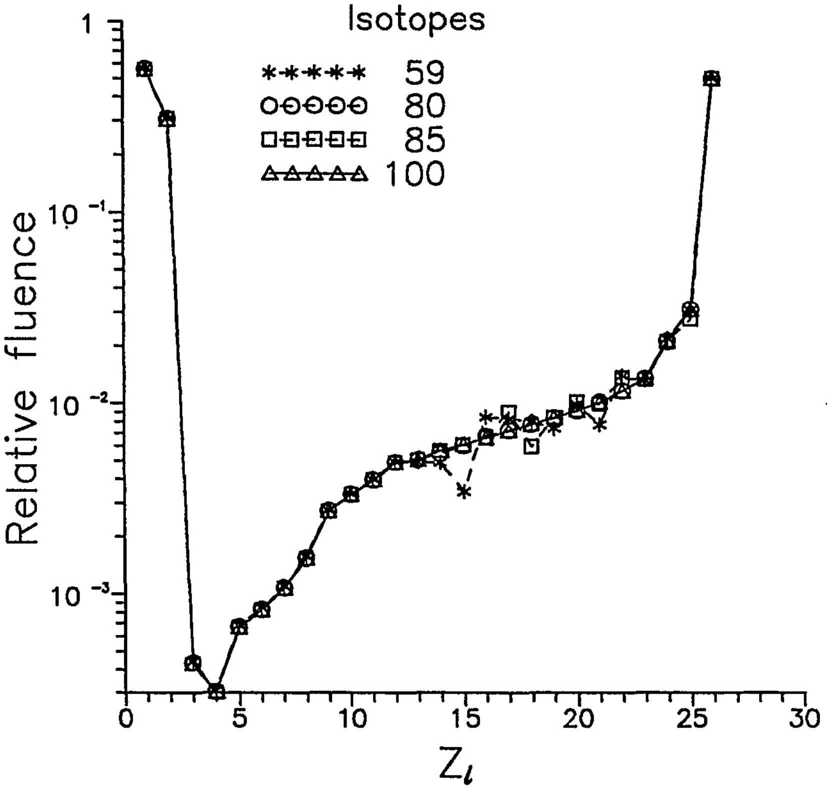

Figure 13. Convergence of charge distribution of 505 MeV/amu iron beams in 5 g/cm^2 of epoxy for 59, 80, 85, and 100 isotopes

Reproduced with permission of the copyright owner. Further reproduction prohibited without permission.

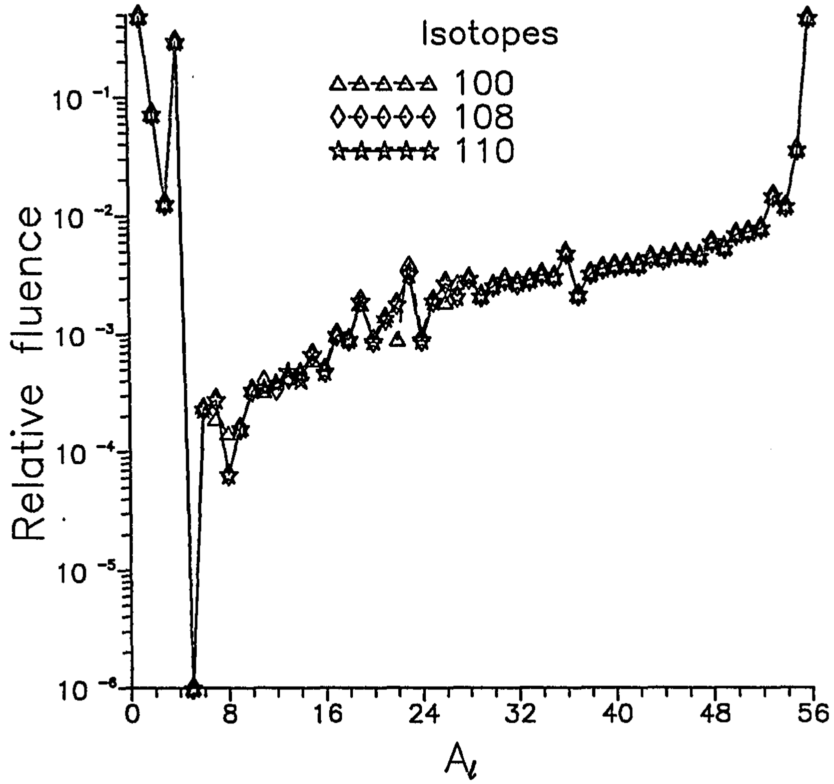

Figure 14. Convergence of mass distribution of 505 MeV/amu iron beams in 5 g/cm^2 of epoxy for 100, 108, and 110 isotopes

Reproduced with permission of the copyright owner. Further reproduction prohibited without permission.

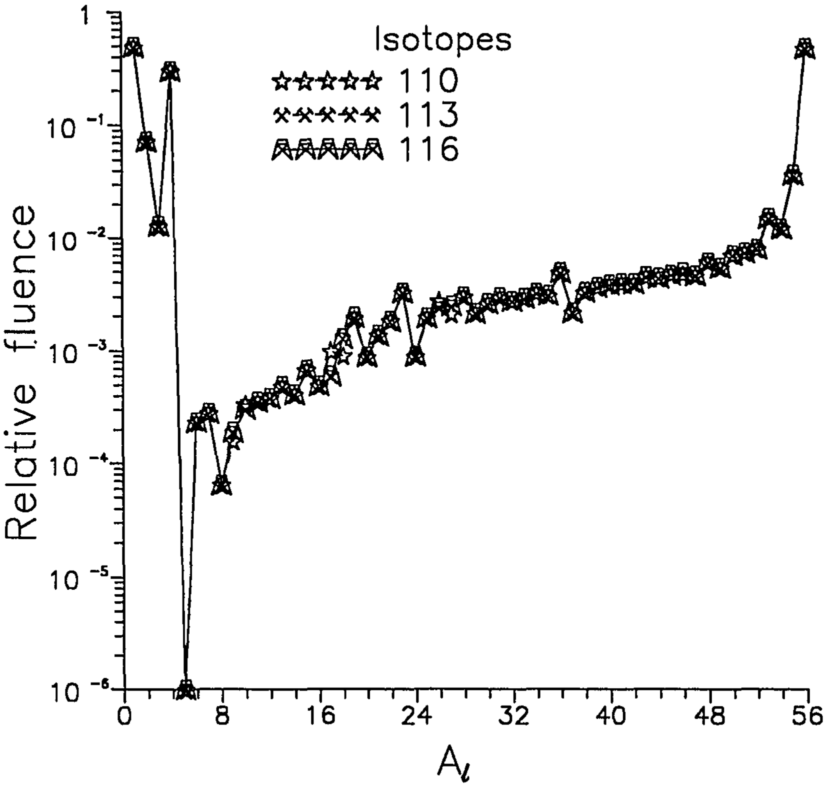

Figure 15. Convergence of mass distribution of 505 MeV/amu iron beams in 5 g/cm^2 of epoxy for 110, 113, and 116 isotopes

Reproduced with permission of the copyright owner. Further reproduction prohibited without permission.

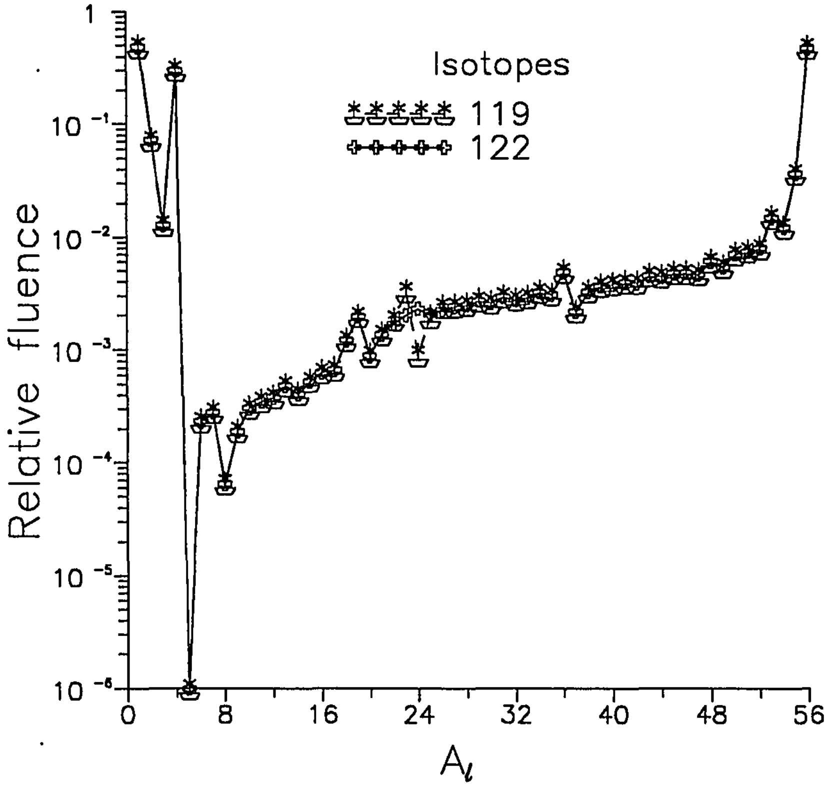

Figure 16. Convergence of mass distribution of 505 MeV/amu iron beams in 5 g/cm^2 of epoxy for 119 and 122 isotopes

Reproduced with permission of the copyright owner. Further reproduction prohibited without permission.

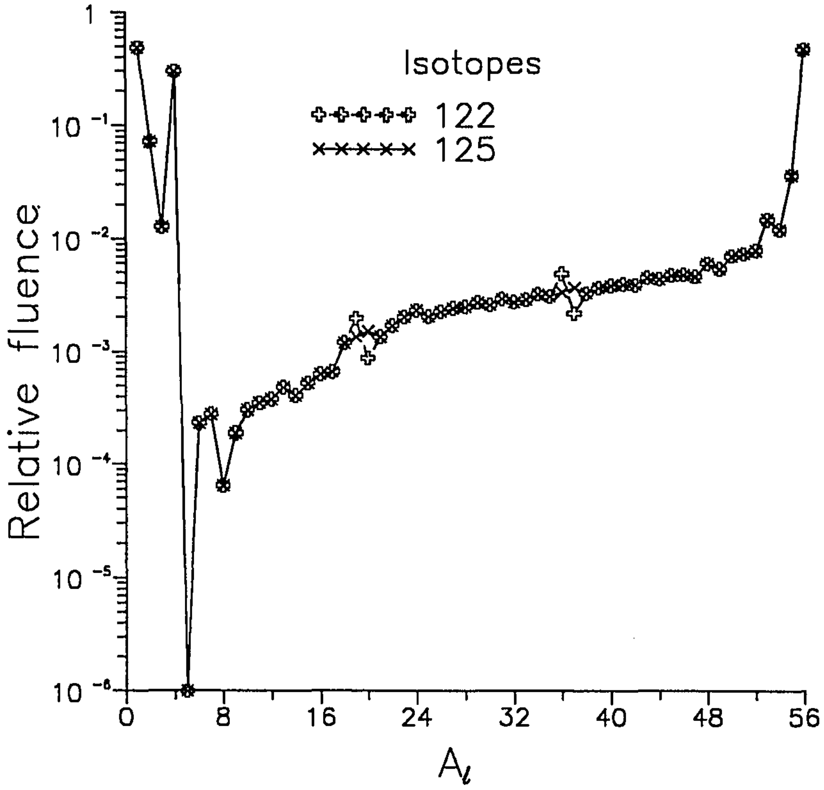

Figure 17. Convergence of mass distribution of 505 MeV/amu iron beams in 5 g/cm^2 of epoxy for 122 and 125 isotopes

Reproduced with permission of the copyright owner. Further reproduction prohibited without permission.

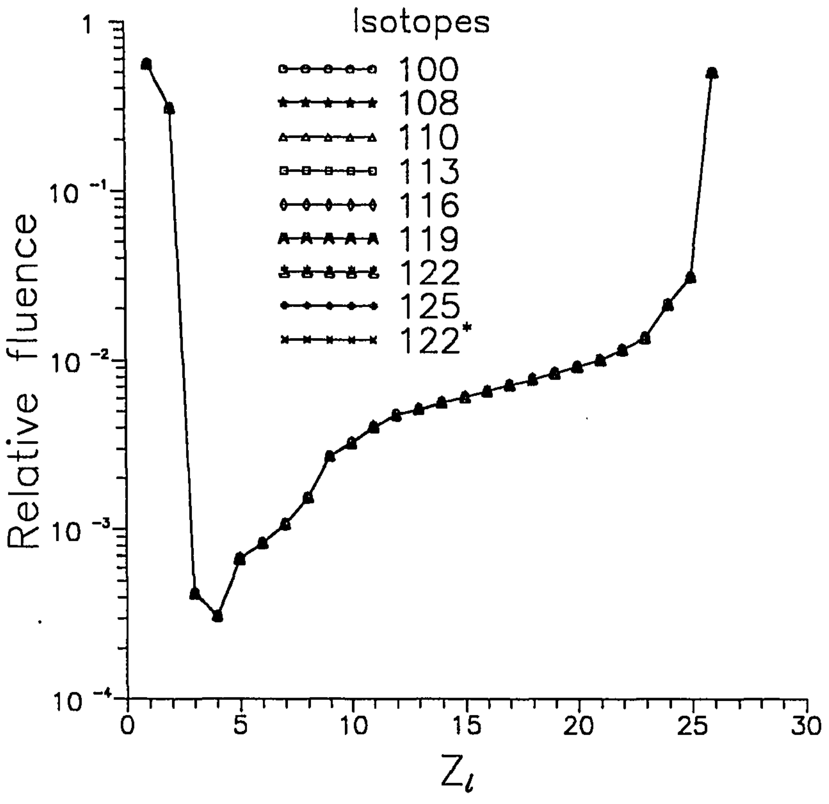

Figure 18. Convergence of charge distribution of 505 MeV/amu iron beams in 5 g/cm^2 of epoxy above 100 isotopes

Reproduced with permission of the copyright owner. Further reproduction prohibited without permission.

3.4 Results and Discussion

Interaction with structural materials is a recognized means of reducing exposure risk from HZE particles in space. A theoretical study was initiated to investigate the alteration of space radiations by shield materials in order to prepare an evaluation of risk reduction through materials selection.

It has been shown that light hydrogenous compounds show great promise as a high performance shield material. Thus, the effects of hydrogen-bearing compounds as potential space structural components were examined by comparing the total ion fluence after passing through the shield. For energetic ion beams a polyethylene target with its high hydrogen density is the most effective absorber for thick shields, while a polytetrafluoroethylene target with the heavier fluorine atoms appears to be more effective for thin shields with respect to the production of secondary radiation. Adding an epoxy to bind lunar regolith in a composite enhances its shielding properties from HZE particles. The inclusion of boron in a polymeric material diminishes only slightly the material's capacity to absorb HZE particles. Lunar regolith is a less effective shield material for HZE particles than the hydrogen-containing polymers studied. Therefore, a material with a high percentage of lighter atoms such as hydrogen would be effective for a thick shield while a material with a heavier atomic composition might yet prove to be more effective in thin

Reproduced with permission of the copyright owner. Further reproduction prohibited without permission.

shields for energetic ion beams with respect to the number of secondary particles without considering their radiation quality. The effect of each radiation quality is evaluated in chapters 4 and 5. Pilot experiments to validate these theoretical results have been performed but data reduction is not yet complete (Thibeault, S. A., private communication).

Computational precision of charge and mass distribution was achieved by increasing the size of the isotope table. However, each additional isotope requires additional computation time to generate the nonperturbative Green's functions for the selected isotope table. An optimal choice of isotope table is needed for both computational precision and practical computation time.

The detailed isotope selections are shown in tables 7 and 8. Figures 17 to 19 show that a useful choice is the revised table of 122 isotopes. In figures 17 and 19, the integral output spectra converge within 5 percent compared with the 125-isotope list over the entire projectile fragment nuclear mass range of 1 to 56. In figure 18, integral output spectra are plotted over the charge range of 1 to 26, where the maximum difference between successive tests is 2.7 percent over the entire projectile fragment nuclei range for tables with 100 or more isotopes. A similar plot for 80 isotopes (figure 10) gives a maximum difference of 3.1 percent compared to that for 125 isotopes. Although the largest list considered (125 isotopes) may not be fully converged, the error introduced by

Reproduced with permission of the copyright owner. Further reproduction prohibited without permission.

the 125-isotope list is believed to be much less than 5 percent in mass and 2 percent in charge distribution.

Improvements in the treatment of the nuclear database are required so that space radiation codes will agree even with the sparse experiments that have been carried out so far[26, 27]. The improvement addressed in this section was the determination of a useful isotope table to generate the nuclear database that gives both computational precision and practical computation time. An iron beam in a cured epoxy was chosen to study the effects of isotope list selection on the mass and charge distributions of the transmitted fluence computed by nonperturbative methods in the transport of high-charge and high-energy ions. A table of 80 isotopes enables the charge versus fluence spectra to converge within 3.1 percent; a table of 100 isotopes converges within 2.7 percent. A table of 122 isotopes yields nuclear mass versus fluence spectra that converge within 5 percent. These tables also result in practical computation times. Iron is the most abundant massive ion in space and the fragmentation event is dominated by the nuclear structure of the projectiles; so these results are generally applicable to other materials and ions important to the space radiation problem.

Reproduced with permission of the copyright owner. Further reproduction prohibited without permission.

Table 7. Detailed index for isotopes 59-110

Z	Number of isotopes					
	59	80	85	100	108	110
0	^{1}n	^{1}n	^{1}n	^{1}n	^{1}n	^{1}n
1	^{1}H	^{1}H	^{1}H	^{1}H	^{1}H	^{1}H
	^{2}H	^{2}H	^{2}H	^{2}H	^{2}H	^{2}H
	^{3}H	^{3}H	^{3}H	^{3}H	^{3}H	^{3}H
2	^{3}He	^{3}He	^{3}He	^{3}He	^{3}He	^{3}He
	^{4}He	^{4}He	^{4}He	^{4}He	^{4}He	^{4}He
3	^{6}Li	^{6}Li	^{6}Li	^{6}Li	^{6}Li	^{6}Li
	^{7}Li	^{7}Li	^{7}Li	^{7}Li	^{7}Li	^{7}Li
4					^{7}Be	^{7}Be
	^{8}Be	^{8}Be	^{8}Be	^{8}Be	^{8}Be	^{8}Be
	^{9}Be	^{9}Be	^{9}Be	^{9}Be	^{9}Be	^{9}Be
5	^{10}B	^{10}B	^{10}B	^{10}B	^{10}B	^{10}B
	^{11}B	^{11}B	^{11}B	^{11}B	^{11}B	^{11}B
						^{12}B
6					^{11}C	^{11}C
	^{12}C	^{12}C	^{12}C	^{12}C	^{12}C	^{12}C
	^{13}C	^{13}C	^{13}C	^{13}C	^{13}C	^{13}C
7						^{13}N
	^{14}N	^{14}N	^{14}N	^{14}N	^{14}N	^{14}N
	^{15}N	^{15}N	^{15}N	^{15}N	^{15}N	^{15}N
8					^{15}O	^{15}O
	^{16}O	^{16}O	^{16}O	^{16}O	^{16}O	^{16}O
	^{17}O	^{17}O	^{17}O	^{17}O	^{17}O	^{17}O
9	^{18}F	^{18}F	^{18}F	^{18}F	^{18}F	^{18}F
	^{19}F	^{19}F	^{19}F	^{19}F	^{19}F	^{19}F
10					^{19}Ne	^{19}Ne
	^{20}Ne	^{20}Ne	^{20}Ne	^{20}Ne	^{20}Ne	^{20}Ne
	^{21}Ne	^{21}Ne	^{21}Ne	^{21}Ne	^{21}Ne	^{21}Ne
	^{22}Ne	^{22}Ne	^{22}Ne	^{22}Ne	^{22}Ne	^{22}Ne
11					^{22}Na	^{22}Na
	^{23}Na	^{23}Na	^{23}Na	^{23}Na	^{23}Na	^{23}Na
12					^{23}Mg	^{23}Mg
	^{24}Mg	^{24}Mg	^{24}Mg	^{24}Mg	^{24}Mg	^{24}Mg
	^{25}Mg	^{25}Mg	^{25}Mg	^{25}Mg	^{25}Mg	^{25}Mg
	^{26}Mg	^{26}Mg	^{26}Mg	^{26}Mg	^{26}Mg	^{26}Mg

Reproduced with permission of the copyright owner. Further reproduction prohibited without permission.

Table 7. Continued

Z	Number of isotopes					
	59	80	85	100	108	110
13					^{26}Al	^{26}Al
	^{27}Al	^{27}Al	^{27}Al	^{27}Al	^{27}Al	^{27}Al
		^{28}Al	^{28}Al	^{28}Al	^{28}Al	^{28}Al
14					^{27}Si	^{27}Si
	^{28}Si	^{28}Si	^{28}Si	^{28}Si	^{28}Si	^{28}Si
		^{29}Si	^{29}Si	^{29}Si	^{29}Si	^{29}Si
			^{30}Si	^{30}Si	^{30}Si	^{30}Si
			^{31}Si	^{31}Si	^{31}Si	^{31}Si
15	^{29}P	^{29}P	^{29}P	^{29}P	^{29}P	^{29}P
		^{30}P	^{30}P	^{30}P	^{30}P	^{30}P
		^{31}P	^{31}P	^{31}P	^{31}P	^{31}P
			^{32}P	^{32}P	^{32}P	^{32}P
			^{33}P	^{33}P	^{33}P	^{33}P
			^{34}P	^{34}P	^{34}P	^{34}P
16	^{30}S					
	^{31}S	^{31}S	^{31}S	^{31}S	^{31}S	^{31}S
	^{32}S	^{32}S	^{32}S	^{32}S	^{32}S	^{32}S
		^{33}S	^{33}S	^{33}S	^{33}S	^{33}S
		^{34}S	^{34}S	^{34}S	^{34}S	^{34}S
			^{35}S	^{35}S	^{35}S	^{35}S
			^{36}S	^{36}S	^{36}S	^{36}S
				^{37}S	^{37}S	^{37}S
17	^{33}Cl					
		^{34}Cl	^{34}Cl	^{34}Cl	^{34}Cl	^{34}Cl
	^{35}Cl	^{35}Cl	^{35}Cl	^{35}Cl	^{35}Cl	^{35}Cl
		^{36}Cl	^{36}Cl	^{36}Cl	^{36}Cl	^{36}Cl
		^{37}Cl	^{37}Cl	^{37}Cl	^{37}Cl	^{37}Cl
			^{38}Cl	^{38}Cl	^{38}Cl	^{38}Cl
				^{39}Cl	^{39}Cl	^{39}Cl
18	^{34}Ar					
	^{36}Ar	^{36}Ar		^{36}Ar	^{36}Ar	^{36}Ar
	^{38}Ar	^{38}Ar		^{38}Ar	^{38}Ar	^{38}Ar
		^{39}Ar	^{39}Ar	^{39}Ar	^{39}Ar	^{39}Ar
		^{40}Ar	^{40}Ar	^{40}Ar	^{40}Ar	^{40}Ar
			^{41}Ar	^{41}Ar	^{41}Ar	^{41}Ar
				^{42}Ar	^{42}Ar	^{42}Ar

Reproduced with permission of the copyright owner. Further reproduction prohibited without permission.

Table 7. Continued

Z	Number of isotopes					
	59	80	85	100	108	110
19	^{37}K	^{37}K	^{37}K	^{37}K	^{37}K	^{37}K
	^{39}K	^{39}K	^{39}K	^{39}K	^{39}K	^{39}K
		^{40}K	^{40}K	^{40}K	^{40}K	^{40}K
		^{41}K	^{41}K	^{41}K	^{41}K	^{41}K
			^{42}K	^{42}K	^{42}K	^{42}K
			^{43}K	^{43}K	^{43}K	^{43}K
20	^{40}Ca	^{40}Ca	^{40}Ca	^{40}Ca	^{40}Ca	^{40}Ca
	^{41}Ca	^{41}Ca	^{41}Ca	^{41}Ca	^{41}Ca	^{41}Ca
	^{42}Ca	^{42}Ca	^{42}Ca	^{42}Ca	^{42}Ca	^{42}Ca
		^{43}Ca	^{43}Ca	^{43}Ca	^{43}Ca	^{43}Ca
			^{44}Ca	^{44}Ca	^{44}Ca	^{44}Ca
			^{45}Ca	^{45}Ca	^{45}Ca	^{45}Ca
21	^{43}Sc	^{43}Sc		^{43}Sc	^{43}Sc	^{43}Sc
		^{44}Sc		^{44}Sc	^{44}Sc	^{44}Sc
		^{45}Sc	^{45}Sc	^{45}Sc	^{45}Sc	^{45}Sc
		^{46}Sc	^{46}Sc	^{46}Sc	^{46}Sc	^{46}Sc
			^{47}Sc	^{47}Sc	^{47}Sc	^{47}Sc
			^{48}Sc	^{48}Sc	^{48}Sc	^{48}Sc
22	^{44}Ti	^{44}Ti		^{44}Ti	^{44}Ti	^{44}Ti
	^{45}Ti	^{45}Ti		^{45}Ti	^{45}Ti	^{45}Ti
	^{46}Ti	^{46}Ti		^{46}Ti	^{46}Ti	^{46}Ti
	^{47}Ti	^{47}Ti	^{47}Ti	^{47}Ti	^{47}Ti	^{47}Ti
		^{48}Ti	^{48}Ti	^{48}Ti	^{48}Ti	^{48}Ti
		^{49}Ti	^{49}Ti	^{49}Ti	^{49}Ti	^{49}Ti
			^{50}Ti	^{50}Ti	^{50}Ti	^{50}Ti
23	^{48}V	^{48}V		^{48}V	^{48}V	^{48}V
	^{49}V	^{49}V		^{49}V	^{49}V	^{49}V
		^{50}V	^{50}V	^{50}V	^{50}V	^{50}V
		^{51}V	^{51}V	^{51}V	^{51}V	^{51}V
		^{52}V	^{52}V	^{52}V	^{52}V	^{52}V
24	^{50}Cr	^{50}Cr		^{50}Cr	^{50}Cr	^{50}Cr
	^{51}Cr	^{51}Cr		^{51}Cr	^{51}Cr	^{51}Cr
	^{52}Cr	^{52}Cr	^{52}Cr	^{52}Cr	^{52}Cr	^{52}Cr
		^{53}Cr	^{53}Cr	^{53}Cr	^{53}Cr	^{53}Cr
			^{54}Cr	^{54}Cr	^{54}Cr	^{54}Cr

Reproduced with permission of the copyright owner. Further reproduction prohibited without permission.

Table 7. Concluded

	Number of isotopes					
Z	59	80	85	100	108	110
25	^{53}Mn	^{53}Mn		^{53}Mn	^{53}Mn	^{53}Mn
	^{54}Mn	^{54}Mn	^{54}Mn	^{54}Mn	^{54}Mn	^{54}Mn
		^{55}Mn	^{55}Mn	^{55}Mn	^{55}Mn	^{55}Mn
26	^{55}Fe	^{55}Fe	^{55}Fe	^{55}Fe	^{55}Fe	^{55}Fe
	^{56}Fe	^{56}Fe	^{56}Fe	^{56}Fe	^{56}Fe	^{56}Fe
27	^{57}Co	^{57}Co	^{57}Co	^{57}Co	^{57}Co	^{57}Co
28	^{58}Ni	^{58}Ni	^{58}Ni	^{58}Ni	^{58}Ni	^{58}Ni

Reproduced with permission of the copyright owner. Further reproduction prohibited without permission.

Table 8. Detailed index for isotopes 113-125

Z	Number of isotopes					
	113	116	119	122	125	122*
0	^{1}n	^{1}n	^{1}n	^{1}n	^{1}n	^{1}n
1	^{1}H	^{1}H	^{1}H	^{1}H	^{1}H	^{1}H
	^{2}H	^{2}H	^{2}H	^{2}H	^{2}H	^{2}H
	^{3}H	^{3}H	^{3}H	^{3}H	^{3}H	^{3}H
2	^{3}He	^{3}He	^{3}He	^{3}He	^{3}He	^{3}He
	^{4}He	^{4}He	^{4}He	^{4}He	^{4}He	^{4}He
3	^{6}Li	^{6}Li	^{6}Li	^{6}Li	^{6}Li	^{6}Li
	^{7}Li	^{7}Li	^{7}Li	^{7}Li	^{7}Li	^{7}Li
4	^{7}Be	^{7}Be	^{7}Be	^{7}Be	^{7}Be	^{7}Be
	^{8}Be	^{8}Be	^{8}Be	^{8}Be	^{8}Be	^{8}Be
	^{9}Be	^{9}Be	^{9}Be	^{9}Be	^{9}Be	^{9}Be
5			^{8}B			
	^{9}B	^{9}B	^{9}B	^{9}B	^{9}B	^{9}B
	^{10}B	^{10}B	^{10}B	^{10}B	^{10}B	^{10}B
	^{11}B	^{11}B	^{11}B	^{11}B	^{11}B	^{11}B
	^{12}B	^{12}B	^{12}B	^{12}B	^{12}B	^{12}B
6	^{11}C	^{11}C	^{11}C	^{11}C	^{11}C	^{11}C
	^{12}C	^{12}C	^{12}C	^{12}C	^{12}C	^{12}C
	^{13}C	^{13}C	^{13}C	^{13}C	^{13}C	^{13}C
7	^{13}N	^{13}N	^{13}N	^{13}N	^{13}N	^{13}N
	^{14}N	^{14}N	^{14}N	^{14}N	^{14}N	^{14}N
	^{15}N	^{15}N	^{15}N	^{15}N	^{15}N	^{15}N
			^{16}N	^{16}N	^{16}N	^{16}N
8	^{15}O	^{15}O	^{15}O	^{15}O	^{15}O	^{15}O
	^{16}O	^{16}O	^{16}O	^{16}O	^{16}O	^{16}O
	^{17}O	^{17}O	^{17}O	^{17}O	^{17}O	^{17}O
	^{18}O	^{18}O	^{18}O	^{18}O	^{18}O	^{18}O
		^{19}O	^{19}O	^{19}O	^{19}O	^{19}O
9			^{17}F	^{17}F	^{17}F	^{17}F
	^{18}F	^{18}F	^{18}F	^{18}F	^{18}F	^{18}F
	^{19}F	^{19}F	^{19}F	^{19}F	^{19}F	^{19}F
					^{20}F	^{20}F

*Resulting 122-isotope list that is adequate for ion beams.

Reproduced with permission of the copyright owner. Further reproduction prohibited without permission.

Table 8. Continued

	Number of isotopes					
Z	113	116	119	122	125	122*
10	^{19}Ne	^{19}Ne	^{19}Ne	^{19}Ne	^{19}Ne	^{19}Ne
	^{20}Ne	^{20}Ne	^{20}Ne	^{20}Ne	^{20}Ne	^{20}Ne
	^{21}Ne	^{21}Ne	^{21}Ne	^{21}Ne	^{21}Ne	^{21}Ne
	^{22}Ne	^{22}Ne	^{22}Ne	^{22}Ne	^{22}Ne	^{22}Ne
				^{23}Ne	^{23}Ne	^{23}Ne
11	^{22}Na	^{22}Na	^{22}Na	^{22}Na	^{22}Na	^{22}Na
	^{23}Na	^{23}Na	^{23}Na	^{23}Na	^{23}Na	^{23}Na
				^{24}Na	^{24}Na	^{24}Na
12				^{22}Mg	^{22}Mg	
	^{23}Mg	^{23}Mg	^{23}Mg	^{23}Mg	^{23}Mg	^{23}Mg
	^{24}Mg	^{24}Mg	^{24}Mg	^{24}Mg	^{24}Mg	^{24}Mg
	^{25}Mg	^{25}Mg	^{25}Mg	^{25}Mg	^{25}Mg	^{25}Mg
	^{26}Mg	^{26}Mg	^{26}Mg	^{26}Mg	^{26}Mg	^{26}Mg
	^{27}Mg	^{27}Mg	^{27}Mg	^{27}Mg	^{27}Mg	^{27}Mg
			^{28}Mg	^{28}Mg	^{28}Mg	^{28}Mg
13				^{25}Al	^{25}Al	
	^{26}Al	^{26}Al	^{26}Al	^{26}Al	^{26}Al	^{26}Al
	^{27}Al	^{27}Al	^{27}Al	^{27}Al	^{27}Al	^{27}Al
	^{28}Al	^{28}Al	^{28}Al	^{28}Al	^{28}Al	^{28}Al
			^{29}Al	^{29}Al	^{29}Al	^{29}Al
14	^{27}Si	^{27}Si	^{27}Si	^{27}Si	^{27}Si	^{27}Si
	^{28}Si	^{28}Si	^{28}Si	^{28}Si	^{28}Si	^{28}Si
	^{29}Si	^{29}Si	^{29}Si	^{29}Si	^{29}Si	^{29}Si
	^{30}Si	^{30}Si	^{30}Si	^{30}Si	^{30}Si	^{30}Si
	^{31}Si	^{31}Si	^{31}Si	^{31}Si	^{31}Si	^{31}Si
15	^{29}P	^{29}P	^{29}P	^{29}P	^{29}P	^{29}P
	^{30}P	^{30}P	^{30}P	^{30}P	^{30}P	^{30}P
	^{31}P	^{31}P	^{31}P	^{31}P	^{31}P	^{31}P
	^{32}P	^{32}P	^{32}P	^{32}P	^{32}P	^{32}P
	^{33}P	^{33}P	^{33}P	^{33}P	^{33}P	^{33}P
	^{34}P	^{34}P	^{34}P	^{34}P	^{34}P	^{34}P

*Resulting 122-isotope list that is adequate for ion beams.

Reproduced with permission of the copyright owner. Further reproduction prohibited without permission.

Table 8. Continued

Z	Number of isotopes					
	113	116	119	122	125	122*
16	^{31}S	^{31}S	^{31}S	^{31}S	^{31}S	^{31}S
	^{32}S	^{32}S	^{32}S	^{32}S	^{32}S	^{32}S
	^{33}S	^{33}S	^{33}S	^{33}S	^{33}S	^{33}S
	^{34}S	^{34}S	^{34}S	^{34}S	^{34}S	^{34}S
	^{35}S	^{35}S	^{35}S	^{35}S	^{35}S	^{35}S
	^{36}S	^{36}S	^{36}S	^{36}S	^{36}S	^{36}S
	^{37}S	^{37}S	^{37}S	^{37}S	^{37}S	^{37}S
		^{38}S				
17	^{34}Cl	^{34}Cl	^{34}Cl	^{34}Cl	^{34}Cl	^{34}Cl
	^{35}Cl	^{35}Cl	^{35}Cl	^{35}Cl	^{35}Cl	^{35}Cl
	^{36}Cl	^{36}Cl	^{36}Cl	^{36}Cl	^{36}Cl	^{36}Cl
	^{37}Cl	^{37}Cl	^{37}Cl	^{37}Cl	^{37}Cl	^{37}Cl
	^{38}Cl	^{38}Cl	^{38}Cl	^{38}Cl	^{38}Cl	^{38}Cl
	^{39}Cl	^{39}Cl	^{39}Cl	^{39}Cl	^{39}Cl	^{39}Cl
18	^{36}Ar	^{36}Ar	^{36}Ar	^{36}Ar	^{36}Ar	^{36}Ar
					^{37}Ar	^{37}Ar
	^{38}Ar	^{38}Ar	^{38}Ar	^{38}Ar	^{38}Ar	^{38}Ar
	^{39}Ar	^{39}Ar	^{39}Ar	^{39}Ar	^{39}Ar	^{39}Ar
	^{40}Ar	^{40}Ar	^{40}Ar	^{40}Ar	^{40}Ar	^{40}Ar
	^{41}Ar	^{41}Ar	^{41}Ar	^{41}Ar	^{41}Ar	^{41}Ar
	^{42}Ar	^{42}Ar	^{42}Ar	^{42}Ar	^{42}Ar	^{42}Ar
19	^{37}K	^{37}K	^{37}K	^{37}K	^{37}K	^{37}K
	^{39}K	^{39}K	^{39}K	^{39}K	^{39}K	^{39}K
	^{40}K	^{40}K	^{40}K	^{40}K	^{40}K	^{40}K
	^{41}K	^{41}K	^{41}K	^{41}K	^{41}K	^{41}K
	^{42}K	^{42}K	^{42}K	^{42}K	^{42}K	^{42}K
	^{43}K	^{43}K	^{43}K	^{43}K	^{43}K	^{43}K
20	^{40}Ca	^{40}Ca	^{40}Ca	^{40}Ca	^{40}Ca	^{40}Ca
	^{41}Ca	^{41}Ca	^{41}Ca	^{41}Ca	^{41}Ca	^{41}Ca
	^{42}Ca	^{42}Ca	^{42}Ca	^{42}Ca	^{42}Ca	^{42}Ca
	^{43}Ca	^{43}Ca	^{43}Ca	^{43}Ca	^{43}Ca	^{43}Ca
	^{44}Ca	^{44}Ca	^{44}Ca	^{44}Ca	^{44}Ca	^{44}Ca
	^{45}Ca	^{45}Ca	^{45}Ca	^{45}Ca	^{45}Ca	^{45}Ca
		^{46}Ca			^{48}Ca	

*Resulting 122-isotope list that is adequate for ion beams.

Reproduced with permission of the copyright owner. Further reproduction prohibited without permission.

Table 8. Concluded

Z	Number of isotopes					
	113	116	119	122	125	122*
21	$^{43}\mathrm{Sc}$	$^{43}\mathrm{Sc}$	$^{43}\mathrm{Sc}$	$^{43}\mathrm{Sc}$	$^{43}\mathrm{Sc}$	$^{43}\mathrm{Sc}$
	$^{44}\mathrm{Sc}$	$^{44}\mathrm{Sc}$	$^{44}\mathrm{Sc}$	$^{44}\mathrm{Sc}$	$^{44}\mathrm{Sc}$	$^{44}\mathrm{Sc}$
	$^{45}\mathrm{Sc}$	$^{45}\mathrm{Sc}$	$^{45}\mathrm{Sc}$	$^{45}\mathrm{Sc}$	$^{45}\mathrm{Sc}$	$^{45}\mathrm{Sc}$
	$^{46}\mathrm{Sc}$	$^{46}\mathrm{Sc}$	$^{46}\mathrm{Sc}$	$^{46}\mathrm{Sc}$	$^{46}\mathrm{Sc}$	$^{46}\mathrm{Sc}$
	$^{47}\mathrm{Sc}$	$^{47}\mathrm{Sc}$	$^{47}\mathrm{Sc}$	$^{47}\mathrm{Sc}$	$^{47}\mathrm{Sc}$	$^{47}\mathrm{Sc}$
	$^{48}\mathrm{Sc}$	$^{48}\mathrm{Sc}$	$^{48}\mathrm{Sc}$	$^{48}\mathrm{Sc}$	$^{48}\mathrm{Sc}$	$^{48}\mathrm{Sc}$
22	$^{44}\mathrm{Ti}$	$^{44}\mathrm{Ti}$	$^{44}\mathrm{Ti}$	$^{44}\mathrm{Ti}$	$^{44}\mathrm{Ti}$	$^{44}\mathrm{Ti}$
	$^{45}\mathrm{Ti}$	$^{45}\mathrm{Ti}$	$^{45}\mathrm{Ti}$	$^{45}\mathrm{Ti}$	$^{45}\mathrm{Ti}$	$^{45}\mathrm{Ti}$
	$^{46}\mathrm{Ti}$	$^{46}\mathrm{Ti}$	$^{46}\mathrm{Ti}$	$^{46}\mathrm{Ti}$	$^{46}\mathrm{Ti}$	$^{46}\mathrm{Ti}$
	$^{47}\mathrm{Ti}$	$^{47}\mathrm{Ti}$	$^{47}\mathrm{Ti}$	$^{47}\mathrm{Ti}$	$^{47}\mathrm{Ti}$	$^{47}\mathrm{Ti}$
	$^{48}\mathrm{Ti}$	$^{48}\mathrm{Ti}$	$^{48}\mathrm{Ti}$	$^{48}\mathrm{Ti}$	$^{48}\mathrm{Ti}$	$^{48}\mathrm{Ti}$
	$^{49}\mathrm{Ti}$	$^{49}\mathrm{Ti}$	$^{49}\mathrm{Ti}$	$^{49}\mathrm{Ti}$	$^{49}\mathrm{Ti}$	$^{49}\mathrm{Ti}$
	$^{50}\mathrm{Ti}$	$^{50}\mathrm{Ti}$	$^{50}\mathrm{Ti}$	$^{50}\mathrm{Ti}$	$^{50}\mathrm{Ti}$	$^{50}\mathrm{Ti}$
23	$^{48}\mathrm{V}$	$^{48}\mathrm{V}$	$^{48}\mathrm{V}$	$^{48}\mathrm{V}$	$^{48}\mathrm{V}$	$^{48}\mathrm{V}$
	$^{49}\mathrm{V}$	$^{49}\mathrm{V}$	$^{49}\mathrm{V}$	$^{49}\mathrm{V}$	$^{49}\mathrm{V}$	$^{49}\mathrm{V}$
	$^{50}\mathrm{V}$	$^{50}\mathrm{V}$	$^{50}\mathrm{V}$	$^{50}\mathrm{V}$	$^{50}\mathrm{V}$	$^{50}\mathrm{V}$
	$^{51}\mathrm{V}$	$^{51}\mathrm{V}$	$^{51}\mathrm{V}$	$^{51}\mathrm{V}$	$^{51}\mathrm{V}$	$^{51}\mathrm{V}$
	$^{52}\mathrm{V}$	$^{52}\mathrm{V}$	$^{52}\mathrm{V}$	$^{52}\mathrm{V}$	$^{52}\mathrm{V}$	$^{52}\mathrm{V}$
24	$^{50}\mathrm{Cr}$	$^{50}\mathrm{Cr}$	$^{50}\mathrm{Cr}$	$^{50}\mathrm{Cr}$	$^{50}\mathrm{Cr}$	$^{50}\mathrm{Cr}$
	$^{51}\mathrm{Cr}$	$^{51}\mathrm{Cr}$	$^{51}\mathrm{Cr}$	$^{51}\mathrm{Cr}$	$^{51}\mathrm{Cr}$	$^{51}\mathrm{Cr}$
	$^{52}\mathrm{Cr}$	$^{52}\mathrm{Cr}$	$^{52}\mathrm{Cr}$	$^{52}\mathrm{Cr}$	$^{52}\mathrm{Cr}$	$^{52}\mathrm{Cr}$
	$^{53}\mathrm{Cr}$	$^{53}\mathrm{Cr}$	$^{53}\mathrm{Cr}$	$^{53}\mathrm{Cr}$	$^{53}\mathrm{Cr}$	$^{53}\mathrm{Cr}$
	$^{54}\mathrm{Cr}$	$^{54}\mathrm{Cr}$	$^{54}\mathrm{Cr}$	$^{54}\mathrm{Cr}$	$^{54}\mathrm{Cr}$	$^{54}\mathrm{Cr}$
25	$^{53}\mathrm{Mn}$	$^{53}\mathrm{Mn}$	$^{53}\mathrm{Mn}$	$^{53}\mathrm{Mn}$	$^{53}\mathrm{Mn}$	$^{53}\mathrm{Mn}$
	$^{54}\mathrm{Mn}$	$^{54}\mathrm{Mn}$	$^{54}\mathrm{Mn}$	$^{54}\mathrm{Mn}$	$^{54}\mathrm{Mn}$	$^{54}\mathrm{Mn}$
	$^{55}\mathrm{Mn}$	$^{55}\mathrm{Mn}$	$^{55}\mathrm{Mn}$	$^{55}\mathrm{Mn}$	$^{55}\mathrm{Mn}$	$^{55}\mathrm{Mn}$
26	$^{55}\mathrm{Fe}$	$^{55}\mathrm{Fe}$	$^{55}\mathrm{Fe}$	$^{55}\mathrm{Fe}$	$^{55}\mathrm{Fe}$	$^{55}\mathrm{Fe}$
	$^{56}\mathrm{Fe}$	$^{56}\mathrm{Fe}$	$^{56}\mathrm{Fe}$	$^{56}\mathrm{Fe}$	$^{56}\mathrm{Fe}$	$^{56}\mathrm{Fe}$
27	$^{57}\mathrm{Co}$	$^{57}\mathrm{Co}$	$^{57}\mathrm{Co}$	$^{57}\mathrm{Co}$	$^{57}\mathrm{Co}$	$^{57}\mathrm{Co}$
28	$^{58}\mathrm{Ni}$	$^{58}\mathrm{Ni}$	$^{58}\mathrm{Ni}$	$^{58}\mathrm{Ni}$	$^{58}\mathrm{Ni}$	$^{58}\mathrm{Ni}$

*Resulting 122-isotope list that is adequate for ion beams.

Reproduced with permission of the copyright owner. Further reproduction prohibited without permission.

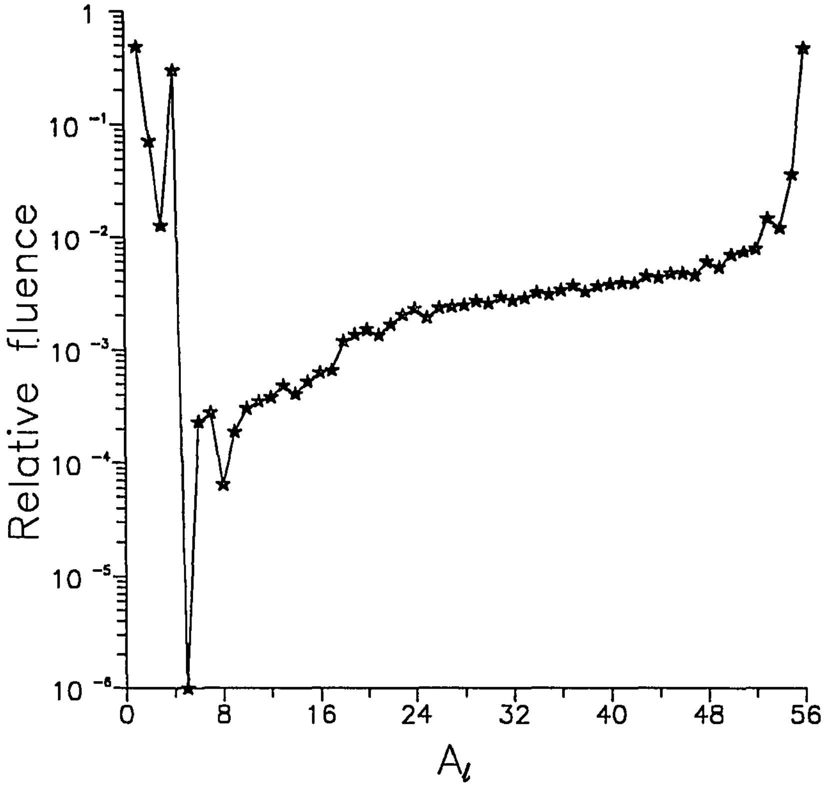

Figure 19. Mass distribution of 505 MeV/amu iron beams in 5 g/cm^2 of epoxy for revised table with 122 isotopes

Reproduced with permission of the copyright owner. Further reproduction prohibited without permission.

CHAPTER 4. APPLICATION TO STATIC RANDOM ACCESS MEMORY DEVICES IN HZE EXPOSURE

4.1 Introduction

Single event upsets (SEUs), or soft errors, are mainly logic upset errors due to a spurious charge produced by the transit of a single ionizing particle in static random access memory (SRAM) in high-density integrated circuitry. Thus, SEUs are a serious consequence of galactic cosmic radiation (GCR) for missions involving miniature spacecraft. The SEU error rate increases with the packing density of integrated circuits and affects the costs for mission plans and for future designs in the small spacecraft program because of the SEU-hardening problem. The accurate prediction of SEU rates would minimize parts and device test requirements to resolve radiation-related problems. With the Langley Research Center cosmic ray code (HZETRN[18]), the transmitted galactic cosmic ray environment at the 1977 solar minimum has been accurately modeled for integral LET flux of different ions with the same LET and for those of each charge group behind various thicknesses of different shield materials. The current status of shielding technology and its impact on the SRAM upset rate are compared with dosimetric calculations because SEUs occur through the physical energy transfer process with device materials during the transit of a single ionizing particle through the chip. The specific energy transfer depends on the radiation type and the reactions induced in the device

Reproduced with permission of the copyright owner. Further reproduction prohibited without permission.

material. The resultant LET spectra from the HZETRN[18] are coupled with a measured upset cross section versus LET curve[56] to calculate the SEU error rate for IMS1601EPI SRAM devices.

The IMS1601EPI device used in the space shuttle computer is an epitaxial substrate version made by Inmos Corp. and a non-radiation hardened 64kx1 SRAM built using a conventional four-transistor cell approach and 1.3 micron complementary metal oxide semiconductor (CMOS) technology[56]. This device has been used in the shuttle SRAM, because it was not susceptible to latchup for LET values up to 100 MeV cm^2/mg when irradiated with heavy ions[57]. In CMOS/epi devices, the sensitive region for a complementary transistor is taken to be the silicon for a conservative calculation[58]. The SEU error rate prediction is calculated by a modified path-length distribution method[58]. This SEU prediction methodology has been compared with actual upset rate data from space shuttle flights and has proven to be capable of accurately predicting the upset rate[56].

The upset rate behind shield materials relative to that in free space gives the estimation of upset rate reduction and also indicates the shield performance of materials for CMOS/epi SRAM devices. The shielding analysis of the SRAM devices is done below by comparison of upset rate contributions from each atomic charge group behind various thickness of shield materials.

Reproduced with permission of the copyright owner. Further reproduction prohibited without permission.

4.2 Energy Absorption on SRAM Devices

The interaction data for ionization and nuclear collisions were combined in the Boltzmann equation with the 1977 solar minimum incident galactic cosmic ray spectrum[59] to evaluate the transmitted radiation field passing through various target materials at different thickness. The physical energy transferred to the silicon of the device is termed its dose. The specific energy transfer depends on both the type and intensity of the transmitted radiation environment which induces reactions in the silicon of the device. Contributions to the dose come from propagating neutrons, protons, alpha particles, and heavy ions (HZE). These particles are target nuclear fragments, primary particles, or their secondaries. Nuclear recoil nuclei (e.g., Al, Mg) in the silicon of the device also contribute to the dose. All secondary particles from HZE interactions are presently assumed to be produced with a velocity equal to that of the incident particle. The assumption for neutrons underestimates the exposure, because the lateral dispersion is strongly affected, particularly by the low energy neutrons[18]. Although the result is underestimated, the doses relative to that in free space are useful for estimating relative shield effectiveness to compare different materials.

The absorbed dose in a SRAM device behind different thickness relative to that in free space is shown in figure 20 for several shield materials. In this figure, the dose behind

Reproduced with permission of the copyright owner. Further reproduction prohibited without permission.

the target materials with large mass, such as lead, copper, iron, and aluminum, exceeds the dose absorbed in free space at all thicknesses up to 30 g/cm^2. Thus, the energy absorbed by microelectronics is not reduced by a spacecraft shield. This is due to the multitude of secondary particles produced in the projectile breakup by the shield nuclei. Dose is a slowly decreasing function of shield thickness for shield materials with light mass, such as polyethylene, lithium hydride, and liquid hydrogen. This is a result of many processes of secondary particle production whereby the heavier GCR nuclei are broken into nucleons and lighter nuclear fragments by nuclear and Coulombic interactions with the shield material. The absorbed dose, *D*, due to energy deposition at a given location, *x*, by all particles is given by

$$D(x) = \sum_j \int_0^\infty S_j(E)\phi_j(x,E)dE. \tag{4.1}$$

The absorbed dose does not effectively represent the harmful effects on microelectronics, because each LET component of a given particle does not cause an SEU. Therefore, a useful LET spectrum is defined for estimating of the SEU error rate. The relative SEU error rate is compared below for various shield materials.

Reproduced with permission of the copyright owner. Further reproduction prohibited without permission.

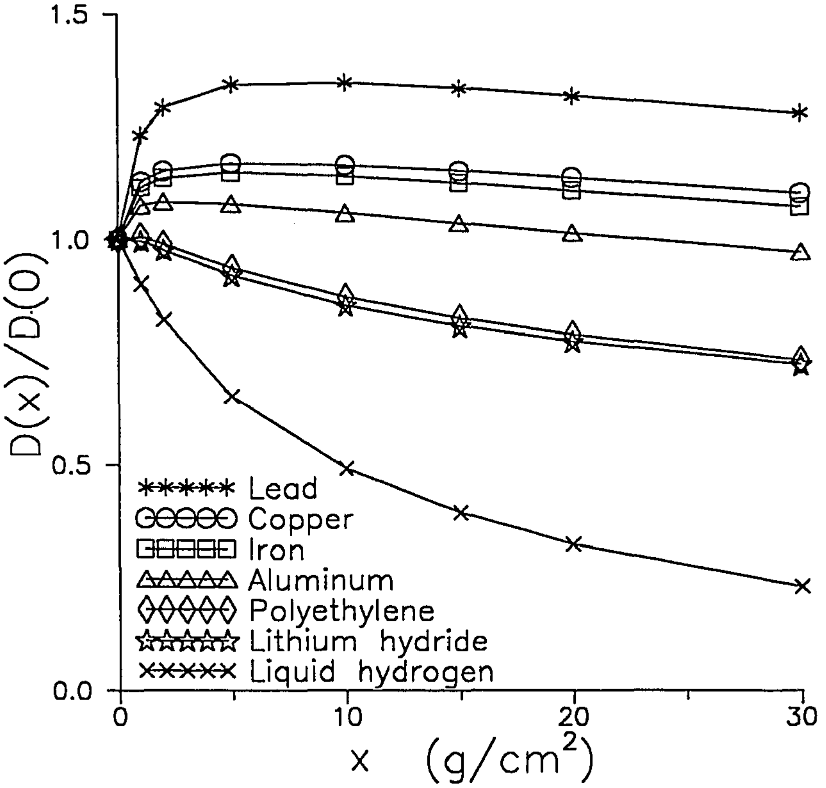

Figure 20. Attenuation of absorbed dose on SRAM behind several shield materials

Reproduced with permission of the copyright owner. Further reproduction prohibited without permission.

4.3 SEU Rate Prediction Methodology

To cause an SEU error, the incident particle must deposit enough ionization energy in the node-sensitive neighborhood[60] of the material to produce the required amount of SEU-inducing charge, Q_c. This means that the particular incident particle must possess sufficient stopping power in the semiconductor material to liberate the critical charge required for an SEU error. For the cosmic ray particles and semiconductors of interest, LET is usually an adequate approximation for stopping power. LET for an ion is its rate of energy loss in a semiconductor. This depends on its Z, A, and energy, and on the material properties of the device. Ions with the same LET are assumed to have the same SEU effect. The energy deposition is commonly expressed in terms of the effective LET, L_{eff}, which is the LET normal to the device face. By assuming that the device is a thin parallelepiped, a particle normally incident (θ=0) on the device would have had to give the energy actually deposited, so that all particles pass through the same depth, the minimum beam ion track length through the device (the device thickness). As the device normal is rotated an angle θ from the beam direction, the track length is increased for the beam ion and the effective LET is increased as $L_{\text{eff}} = L / \cos\theta$, where L is a particle LET. Since the particle flux is isotropic at the device, the path-length distribution function[58], which is the probability distribution of all possible track chord lengths in the parallelepiped sensitive region, is a function of its dimensions.

Reproduced with permission of the copyright owner. Further reproduction prohibited without permission.

The measured upset cross-section represents an upset susceptibility for all particles of a given effective LET. Typically a part is exposed to higher angles of incidence (θ) to increase the effective LET. Then, a higher LET particle is chosen at normal incidence (θ=0) to further increase the LET and so on[56]. The experimental SEU cross section versus effective LET is a semi-empirical function and regarded as measuring a population of device sensitivities, not a distribution of actual cross-sections. The cross-section curve is considered as resulting from hits on very many cells that have the same area, with the spread of LETs that lead to upset resulting from a distribution of critical charges and a distribution of amounts of charge collected. Measurements of heavy ion upset cross-sections as a function of effective LET sometimes show discontinuities in the cross-section curve for two different ions[56], where the ions have different LETs but the same effective LET. These discontinuities can be explained on the basis of geometry effects on large thin devices[60]. When the sensitive volume, which includes the depletion regions of vulnerable junctions, has a thickness (t_i) which is not small compared to one of the lateral dimensions, the actual projection responsible for upset is reduced by a factor of $t_i \sin \theta$ [60], since ions passing through the edges will not have sufficient energy to upset the part. The reduction of the projected area leads to the correction of the measured upset cross sections by using the edge effect[56] determination of P_k, which is the ratio of sensitive volume thickness to width. The value of P_k is estimated based on the device technology[56]. The corrected sensitivity distribution (cross-section curve), which includes the results of simple geometrical effects, appears to be the description of the sensitive volume that leads to the variation of charge collection across the sensitive volume[60]. The failure of a

Reproduced with permission of the copyright owner. Further reproduction prohibited without permission.

population of identical components may be described by a statistical distribution. Each component can fail independently, and all of the components must function for the device not to fail. That is the integral Weibull distribution, which is appropriate to describe upset cross-section measurements[60]. The maximum values of limiting cross-section correspond to the expected sensitive area for the entire chip.

Another LET parameter, important with respect to SEU accelerator and other heavy ion source tests, is the onset threshold LET, L_{th}, and is defined as the minimum LET for which an SEU is assumed to occur. The onset threshold only characterizes the most sensitive cell hit in its most sensitive region. The cross-section curve is broken up into a number of steps in order to more accurately represent several sensitive volumes[60], each with different upset thresholds (L_{thi}) and cross-sections (σ_i)[56]. At a particular LET step there are a few bits newly able to upset. Since the generated charge is directly proportional to the path through the sensitive volume, it is equal to the product of the LET of the ion and the effective chord[58]. The SEU error rate[56] is computed using the upset rate of individual sensitive regions summed over the integral distribution of sensitivities with the knowledge of the SEU cross section and the incident cosmic ray flux.

In the computer memory device, upsets may be caused by two distinct processes[56]. One process is called direct ionization in which the projectile fragment ions of galactic cosmic rays behind the shield material deposit energy directly in the sensitive volume by ionization. The other process is light-ion secondary upsets. In this process energy is

Reproduced with permission of the copyright owner. Further reproduction prohibited without permission.

deposited by heavy ions that are produced in the device as fragments resulting from the interactions called spallation reaction between light ions and silicon nuclei of a SRAM device. These two processes are treated separately in the following sections.

Reproduced with permission of the copyright owner. Further reproduction prohibited without permission.

4.3.1 Direct Ionization

The SEU cross-section was measured by T. Scott as a function of effective LET at the Berkeley 88"-Cyclotron for seven IMS1601EPI devices and referenced by O'Neill and Badhwar[56]. The average measured SEU cross-section for heavy ions versus effective LET[56] are shown in figure 21. It is well known that the upset cross-section is accurately represented by the integral Weibull distribution[60] (see figure 21)

$$\sigma(L) = 1 - \exp\left\{-\left[\frac{(L-L_{th})}{W}\right]^{s}\right\} \qquad \text{for } L > L_{th}$$

$$\sigma(L) = 0 \qquad \text{for } L < L_{th} \qquad (4.2)$$

with L_{th}=2.75 MeV cm^2/mg, W=140.0, and s=0.95. Since the actual cross-section is not a step function but varies with effective LET, the modification takes into account for the Weibull distribution cross-section[56]. The cross-section is modified by dividing it into multiple steps rather than a single upset threshold[60]. The average SEU cross-sections for heavy ions accurately approximate multiple thresholds and cross-sections for each step[56].

Another modification takes into account for the sensitive volume thickness of the device. The sensitive volume thickness (t_i) for each step is found from the computed geometric parameter, P_k. The value of P_k for the IMS1601EPI was determined to be about 0.1 based on edge effect measurements and comparison of predicted and actual upset rates[51]. It was reasonably consistent with the 1.3 μm thick device technology[56].

Reproduced with permission of the copyright owner. Further reproduction prohibited without permission.

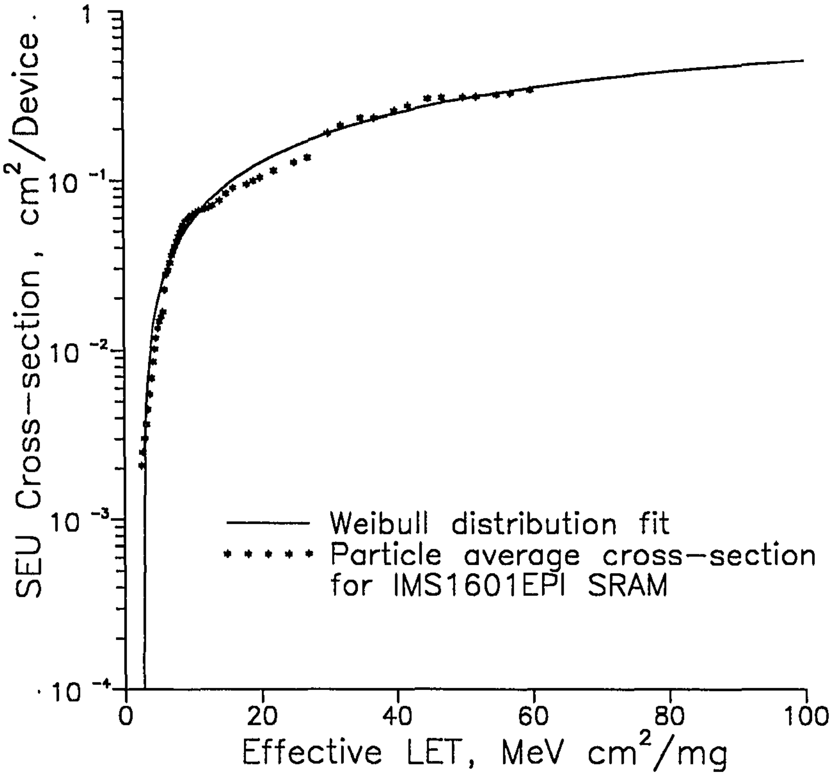

Figure 21. Heavy ion single event upset integral cross-section versus effective linear energy tansfer (LET)

Reproduced with permission of the copyright owner. Further reproduction prohibited without permission.

With the assumption of a very thin and square-shaped sensitive volume, the thickness t_i is found from

$$t_i = P_k\sqrt{\Delta\sigma_i} \tag{4.3}$$

for each step *i*.

A critical charge, Q_c, liberated by a flux of particles incident on the integrated circuit is the quantity of charge necessary to change a binary "one" to a zero, or vice-versa, at a particular storage node. SEU errors are explained as the deposition of Q_c at a storage node by electrons or holes produced in the track made by the incident particle in the device material. In silicon, 3.6 eV of ionization energy is required to produce one electron-hole pair (where the electron charge is $1.6\text{x}10^{-19}$ coulombs). For an incident cosmic ray depositing an amount of energy, E (in MeV), in the device material, the resulting charge generated in silicon in picocoulombs (pC) is $Q = E / 22.5$. A corresponding LET of 96.6 MeV cm^2/mg for silicon with a density of 2.33 g/cm^3 yields 1 pC/μm (Linear Charge Deposition). The critical charge for upsets to the path (t_i) through the i^{th} sensitive volume is the product of $L_{thi} / 96.6$ (i^{th} LCD threshold) and t_i. The minimum LET that can produce an upset to the i^{th} sensitive part by passing across it diagonally is

$$L_{\min_i} = L_{th_i} \times \frac{t_i}{s_{\max}} \tag{4.4}$$

where $s_{\max}$ = the largest path-length found in the i^{th} sensitive volume

= the diagonal of a thin parallelepiped of dimensions *a*, *b*, and *c*

$= (a^2+b^2+c^2)^{½}$.

Reproduced with permission of the copyright owner. Further reproduction prohibited without permission.

Note that in relation (4.4) and subsequent equations it is assumed that LET is constant throughout the volume. The maximum LET is the cutoff LET for the particular LET spectrum used, where the cross-section is saturated at a high effective LET with high angles of incidence. For the IMS1601EPI, the cross section reaches its asymptotic value for an $L_{\max}$ of about 50-100 MeV cm^2/mg.

Since the particle flux is isotropic at the device, the semiconductor chip will have particles passing through it from all directions. The path-length distribution function is the probability distribution of all possible track chord lengths in the sensitive region and is a function of its dimension. The path-length probability density, $D(s_i(L))$, depends on the shape of the sensitive region of the part. $s_i(L)$ is the path-length for which a particle of LET, L, can deposit enough energy within the sensitive volume to cause an upset. This is related to the ion stopping power by

$$s_i(L) = \frac{L_{th_i}}{L} \times t_i \,. \qquad (4.5)$$

Analytical forms for $D(s_i(L))$ for a thin parallelepiped of dimensions a, b, and c have been published[58]. The modified path-length distribution is used to calculate the error rate[56]. The direct deposition SEU rate per device is the sum of the SEU rate of each step and is given by[56]

$$\text{SEU rate (direct deposition)} = \pi \sum_{i=1}^{n} \left\{ A_i L_{th_i} t_i \int_{L_{\min_i}}^{L_{\max}} D[s_i(L)] I(L) L^{-2} dL \right\} \qquad (4.6)$$

where i is the step index, L_{th_i} is the effective LET threshold for the i^{th} step in MeV cm^2/mg, A_i is the surface area of the i^{th} sensitive volume, $D(s_i(L))$ is a modified differential path length distribution for a square and very thin sensitive volume, and $I(L)$ is the radiation environment LET spectrum determined by the HZETRN code[18] (figure 22).

Reproduced with permission of the copyright owner. Further reproduction prohibited without permission.

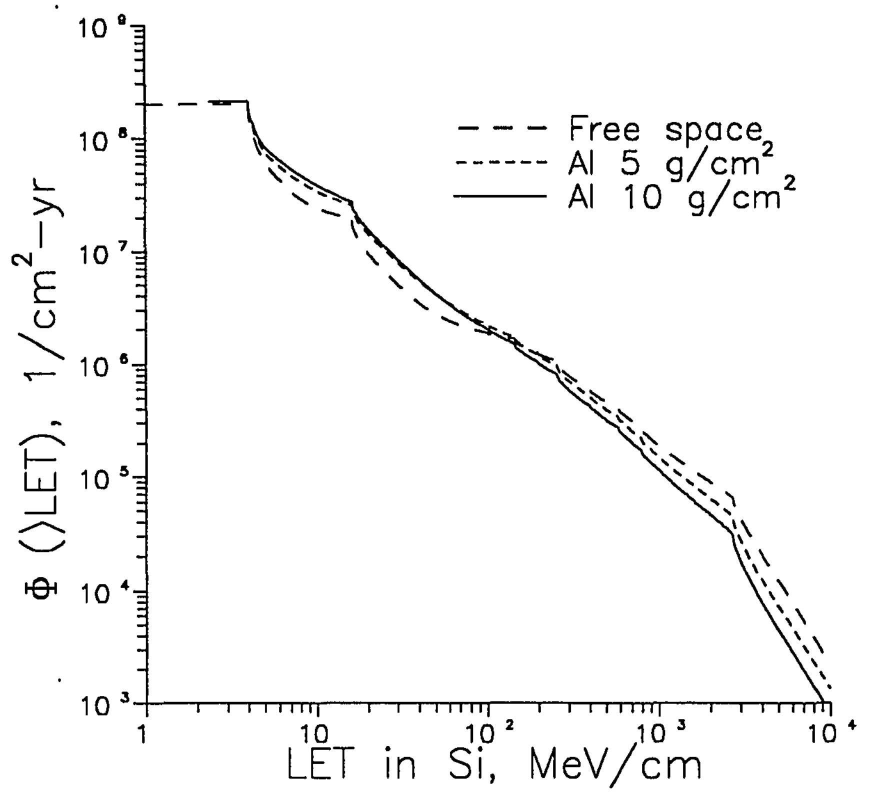

Figure 22. LET-spectra for annual GCR integral flux in free space and behind different thicknesses of aluminum shield at the 1977 solar minimum

Reproduced with permission of the copyright owner. Further reproduction prohibited without permission.

4.3.2 Light-Ion Secondaries

Fast neutrons and protons are produced when galactic cosmic rays pass through a shield material. These particles can produce energetic reaction fragment ions which can cause an SEU indirectly. The reaction products in silicon include ions of sufficient energy and mass number, such as magnesium and aluminum, that can cause an SEU. Alpha particle-induced SEU errors also appear in integrated circuits of high packing density and low powered spacecraft if upset threshold decreases when power supply voltage becomes low. A single alpha particle can ionize enough silicon atoms to produce about 3 million electron hole pairs within a circuit element to create a charge sufficient to cause an upset.

The measured SEU cross-section represents an upset susceptibility for protons of a given energy[56]. The differential SEU cross-section versus energy is calculated analytically by the Weibull distribution based on Harvard cyclotron tests for a proton beam and is given by[56]

$$\begin{aligned} \sigma_p(E) &= 1-\exp\left\{-\left[\frac{(E-E_{th})}{W}\right]^s\right\} && \text{for } E > E_{th} \\ \sigma_p(E) &= 0 && \text{for } E < E_{th} \qquad (4.7) \end{aligned}$$

with E_{th}= 30 MeV, W=100 , and s=2. This is shown in figure 23. With the particle-flux energy distribution of light ions (n, p, ^{2}H, ^{3}H, ^{3}He, ^{4}He) at the sensitive volume, the integral upset rate due to light-ion secondaries is computed as

Reproduced with permission of the copyright owner. Further reproduction prohibited without permission.

SEU rate (light ion secondaries) $=\int_0^{E_{\max}} A^{0.4}\sigma_p(E)J(E)dE.$ (4.8)

$J(E)$ is the differential energy distribution of light ion flux at the sensitive volume in number of particles/(cm^2-day-MeV/amu), $\sigma_p(E)$ is the proton cross-section as a function of energy (MeV/amu), A is the mass of each light ion, and $E_{\max}$ is the highest energy of the proton spectrum which is about 500-1000 MeV/amu.

Reproduced with permission of the copyright owner. Further reproduction prohibited without permission.

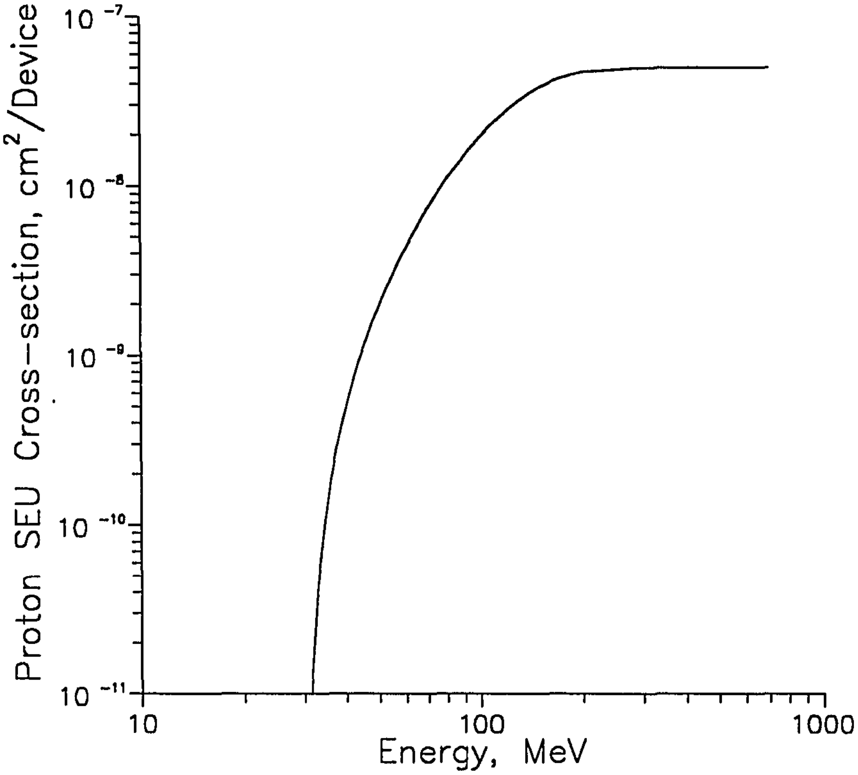

Figure 23. Differential proton single event upset cross-section versus energy

Reproduced with permission of the copyright owner. Further reproduction prohibited without permission.

4.4 Results and Discussion

The high-LET radiation components are usually degraded to lower-LET as a result of nuclear interactions between projectile and target nuclei and such processes become more significant as the particles penetrate further into the shield medium. This is illustrated in figure 22 where integral fluxes of all the ions are plotted as a function of LET at different depths (0, 5, 10 g/cm^2) of aluminum. When transmitted GCR fluences at the 1977 solar minimum through 10 g/cm^2 of iron are compared with respect to aluminum, the iron is the less effective high-LET degrader as shown in figure 24. On the other hand, polyethylene is more effective than aluminum. High-LET ions in GCRs are very instrumental in causing SEUs as seen in figure 21. Thus, a high-LET degrader such as polyethylene can provide better shielding for reducing SEU rates.

By using the SEU rate prediction methodology[56] with the radiation environment determined from HZETRN[18], the relative upset rate behind shield materials can be compared to that in free space. This is shown in figure 25. This relative upset rate gives an estimation of the upset rate reduction achieved by selecting an appropriate shield material. It also indicates the shield performance of materials for SRAM devices which affects costs both for new engineering design and for testing guidelines. SEU is a decreasing function of shield thickness as shown in figure 25. The SEU rate contributions

Reproduced with permission of the copyright owner. Further reproduction prohibited without permission.

from each atomic charge group emerging from the back side of a shield are shown in figures 26 to 29 for four diverse shield materials (lead, aluminum, polyethylene, and liquid hydrogen). The shield efficiency results from the rapid attenuation of SEU contributions from the HZE components of the radiation environment. In lead, contributions from HZE components to the SEU rate are attenuated much more slowly than in the other three shield materials. The SEU rates are attenuated by liquid hydrogen for all radiation components. The SEU rates for heavier radiation components are attenuated more rapidly with shield thickness than for the lighter components. The most efficient shielding is provided by liquid hydrogen; however, hydrogen-containing materials such as polymers will provide relatively good shielding efficiency for SEU.

Reproduced with permission of the copyright owner. Further reproduction prohibited without permission.

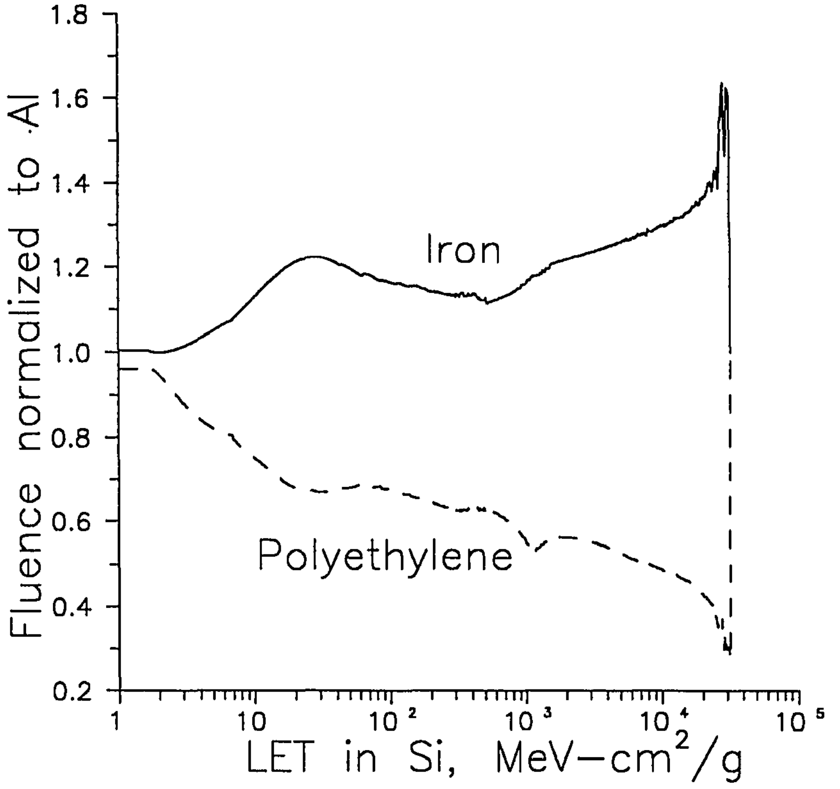

Figure 24. Comparison of transmitted GCR fluence through 10 g/cm^2 of material with respect to aluminum at the 1977 solar minimum

Reproduced with permission of the copyright owner. Further reproduction prohibited without permission.

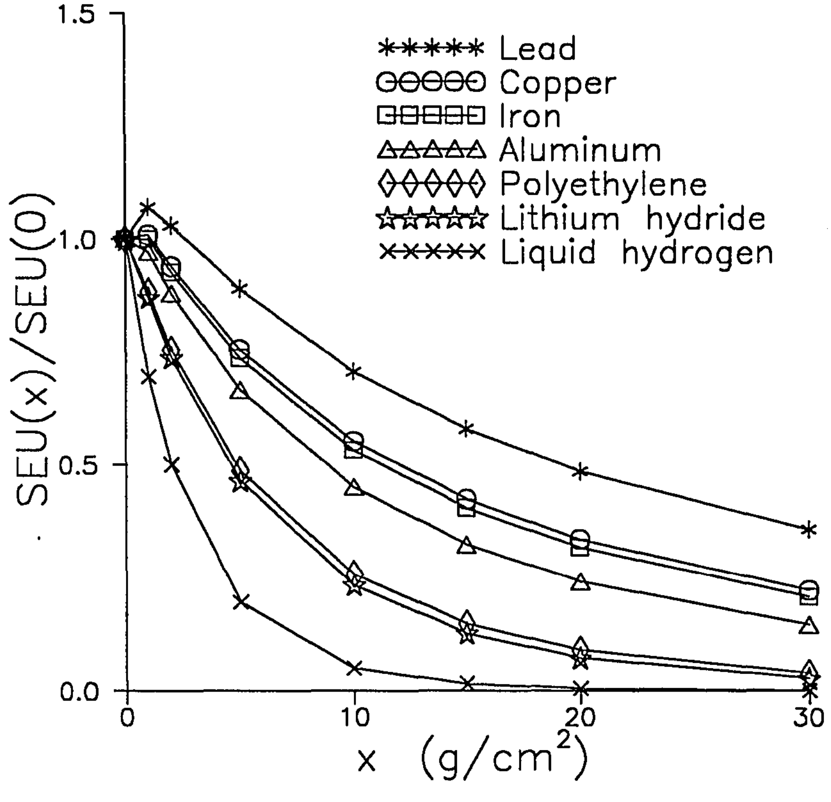

Figure 25. Attenuation of single event upset behind several shield materials

Reproduced with permission of the copyright owner. Further reproduction prohibited without permission.

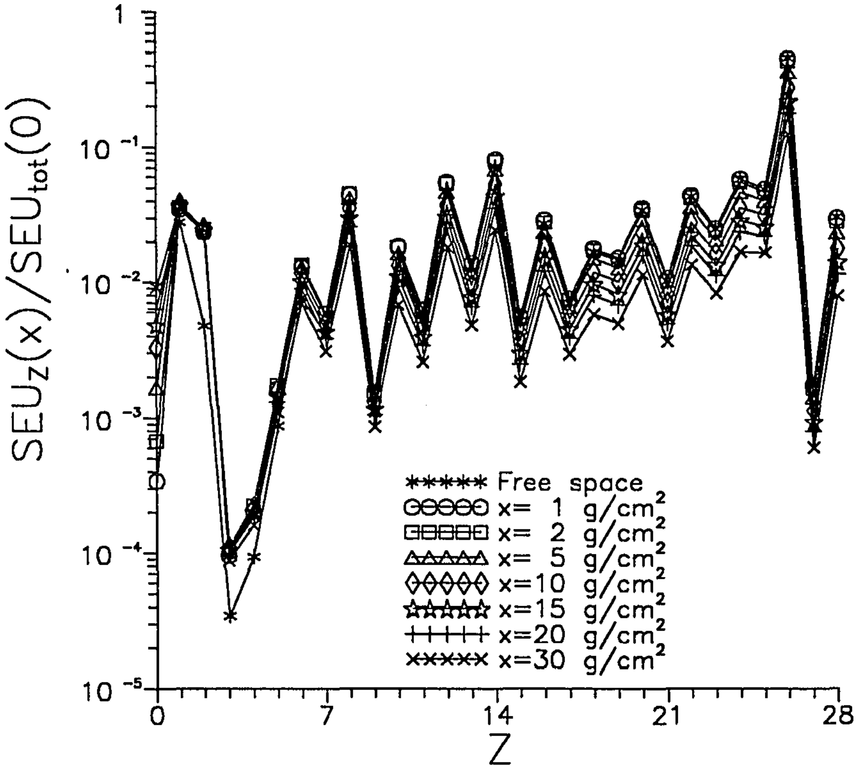

Figure 26. The contributions of SEU from each charge group of the environment

(Lead)

Reproduced with permission of the copyright owner. Further reproduction prohibited without permission.

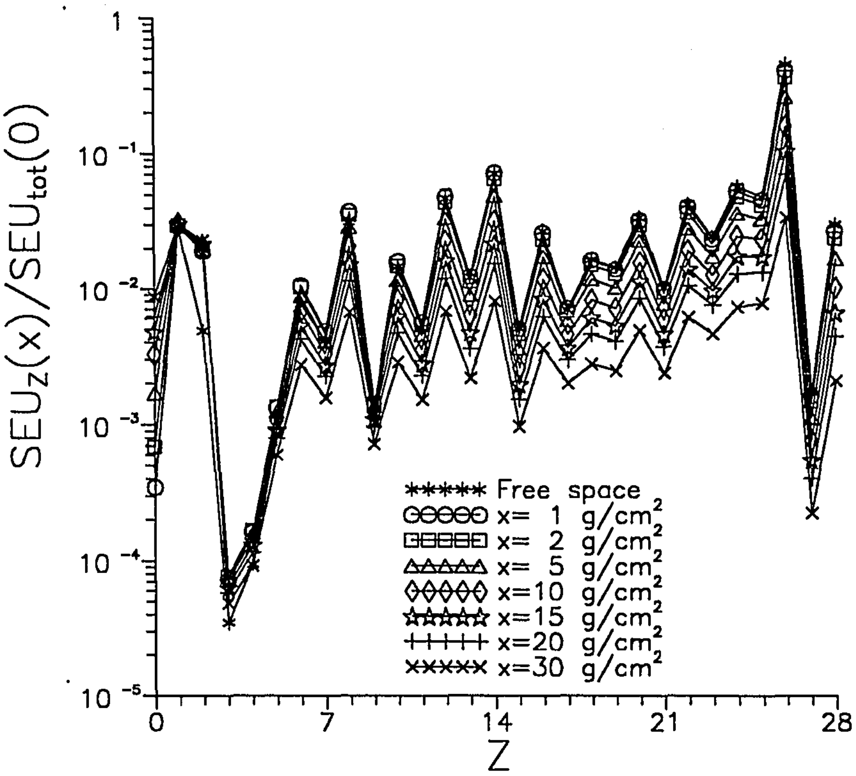

Figure 27. The contributions of SEU from each charge group of the environment (Aluminum)

Reproduced with permission of the copyright owner. Further reproduction prohibited without permission.

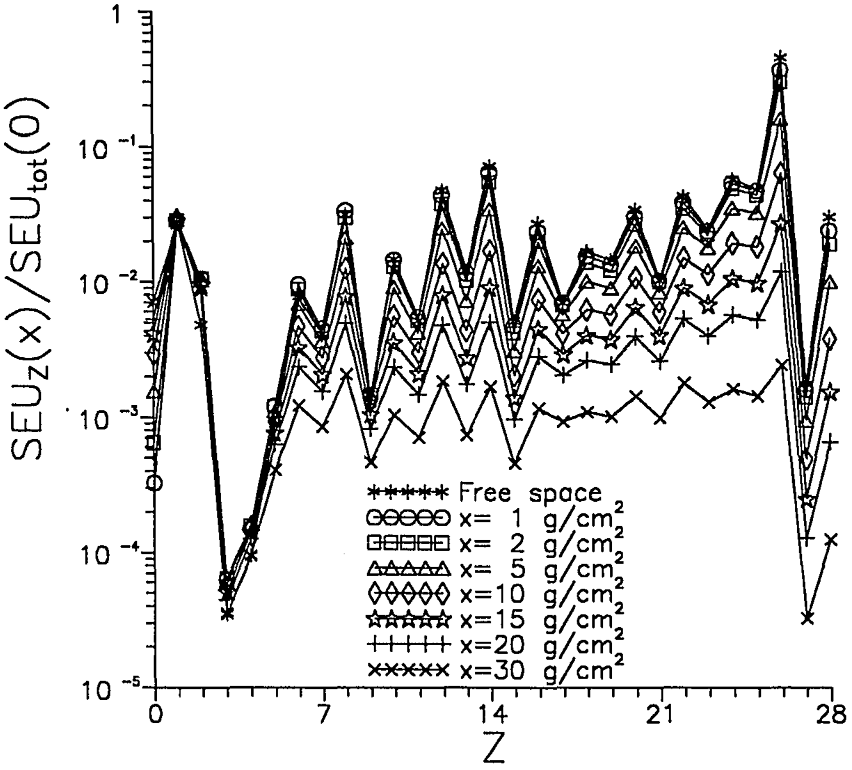

Figure 28. The contributions of SEU from each charge group of the environment (Polyethylene)

Reproduced with permission of the copyright owner. Further reproduction prohibited without permission.

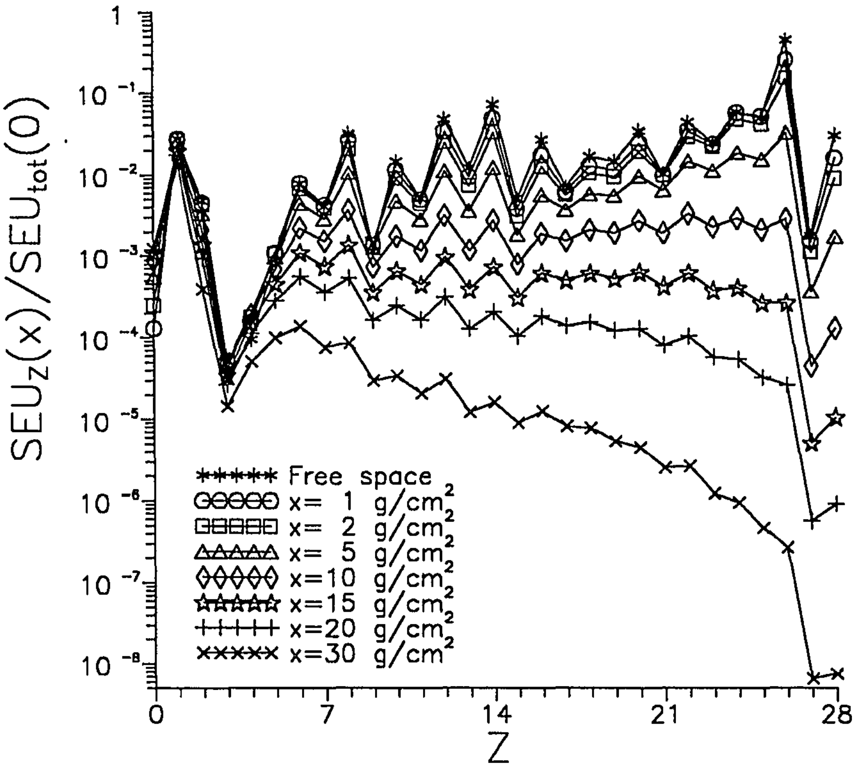

Figure 29. The contributions of SEU from each charge group of the environment

(Liquid hydrogen)

Reproduced with permission of the copyright owner. Further reproduction prohibited without permission.

CHAPTER 5. APPLICATION TO BIOLOGICAL SYSTEM IN HZE EXPOSURE

5.1 Introduction

The principal radiation protection issues were the control of early somatic effects of radiation exposure and their impact on mission safety in past exploratory manned space missions. Early somatic effects are usually seen on whole organs or body systems promptly after an acute, high-radiation exposure, and a definite link between the cause and the effects can be established[14]. It was reasoned by NASA that few, if any, astronauts would make more than one high profile trip to the Moon so that career exposures were of secondary importance. In this context, the galactic cosmic ray (GCR) background (exposures at rates of 150 to 200 mGy/yr) were not of great concern[5,6]. Late somatic effects such as cancer, which would not be immediately observable and occur according to the laws of probability, would be the ultimate limiting factor of career exposure limits for space workers on long-term mission activity. Such a radical shift in astronaut exposure patterns led to a re-evaluation of the importance of low level GCR background exposures.

Within a few years of the discovery of particles of high charge and energy (HZE) as components of the GCR, their unique pattern of energy deposition on the microscopic scale raised issues with respect to their effects on living cells[12]. Although radiobiological knowledge has greatly improved, the risk estimation to the astronaut from such exposures

Reproduced with permission of the copyright owner. Further reproduction prohibited without permission.

is still quite uncertain[61]. Even a crude estimate[6], using the linear energy transfer (LET) dependent quality factor, results in exposures as high as 1.2 Sv/yr near solar minimum. This of course depends on the shielding and makes a large potential impact on the allowable career exposure of a space worker or a deep space explorer.

Evidence that the usual extrapolation of risk from the γ-ray database[62,63] is inadequate has been provided by several experiments[19-21]. In those examples, a quality factor related to RBE becomes meaningless because at doses comparable to that delivered by one particle or a few particles, and for radiation effects that are not manifest for low-LET radiation (e.g., X-rays), the RBE becomes infinite. Thus, new methods to predict the risk resulting from exposure to GCR radiation must be developed.

Apart from the issues of the astronaut's self-shielding factors and uncertainty in the human response to the HZE particles, some control over the radiation environment to which the astronaut is exposed is obtained by shielding. The dose at solar minimum from an annual GCR exposure behind a traditional aluminum shield is shown in figure 30. The absorbed dose increases to a maximum at 3-4 g/cm^2 and declines to the free space value at about 30 g/cm^2. Clearly, no shielding advantage is found in reducing the energy absorbed by the astronaut and, if any protection is provided, it results from changes in the microscopic pattern of the energy absorption events[44].

Reproduced with permission of the copyright owner. Further reproduction prohibited without permission.

Below, the modification of the physical parameters of the attenuated GCR environment at the 1977 solar minimum in various materials are examined to develop an understanding of the qualitative changes in the environmental components as a function of shield composition including tissue equivalent shields. In this context, the role of nuclear cross sections is important in modifying the local environment and the associated microscopic fluctuation in the energy absorption events. The importance of these local environmental modifications is assessed on biological systems in terms of conventional dosimetry using defined quality factors and a track-structure dependent biological model[64].

Radiobiology experiments with immortal cell cultures, which can be sustained indefinitely, have yielded biological data suitable for estimating GCR exposure effects on those specific cell populations, although the human risk associated with such exposure is uncertain. The response of the C3H10T1/2 mouse cell cultures[64] has been used to evaluate shield properties for the biological end points of clonogenic death and neoplastic transformation[44]. Clonogenic death is closely associated with the early response of radiation sickness and neoplastic transformation is related to cancer induction. A cell repair kinetics model including track structure effects for the C3H10T1/2 system[64-66] provides a basis for studying shield performance.

The problem of radiation risk assessment is discussed in the context of microdosimetry. Then the shield parameters related to shield performance are examined and performance is evaluated on the basis of conventional risk assessment and the

Reproduced with permission of the copyright owner. Further reproduction prohibited without permission.

C3H10T1/2 cell model. The effects of shield material selection on shield design are examined on this basis.

The importance of hydrogenous materials in modifying the biologically important components of ion beams makes these studies also important to the evaluation of the therapeutic value of heavy ion beams in medical applications. Indeed, the computational procedures used, the quality of the nuclear database, and the biological response models should be useful in the design of therapeutic procedures.

Reproduced with permission of the copyright owner. Further reproduction prohibited without permission.

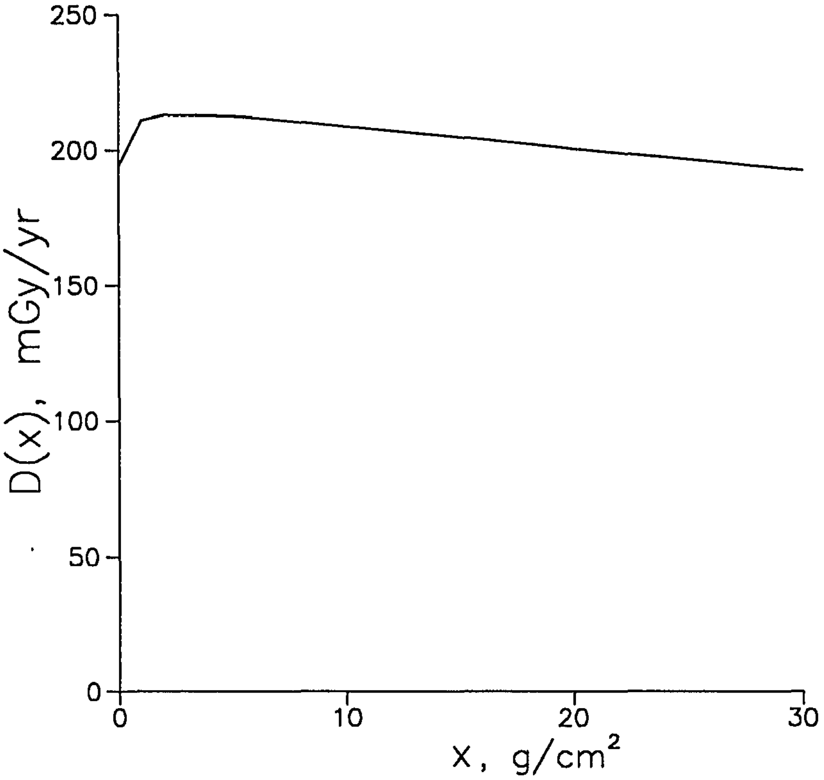

Figure 30. Annual absorbed dose due to GCR exposure at solar minimum behind aluminum shield

Reproduced with permission of the copyright owner. Further reproduction prohibited without permission.

5.2 Microscopic Fluctuations and Biological Response Models

The response of living tissue to a dose D_γ with low LET is represented by a sensitivity coefficient k_γ and a quadratic coefficient D_0 as

$$R_\gamma = k_\gamma D_\gamma \left(1 + \frac{D_\gamma}{D_0}\right) \tag{5.1}$$

where R_γ is either the risk of inducing a specific end point or the level of severity[14, 63]. The parameter D_0 is dose-rate dependent and is on the order of 1.2 Gy for dose rates > 50 mGy/day[14, 63]. Herein a low dose rate is assumed, so that D_γ^2 may be neglected, and

$$R_\gamma = k_\gamma D_\gamma. \tag{5.2}$$

The concept of dose as a physical or chemical insult per unit mass of tissue is a carryover from the concepts of pharmacology and assumes that dose is a measure of the effects on individual cells[67]. Tissue cells are in fact not all equal at low exposures because the energy deposits are quantized and energy is deposited in only a fraction of cells. Further, volumes within a given cell are not all equally sensitive. In general, absorbed dose, D, is not a good measure of biological damage because this average quantity can be decomposed[67] as follows:

$$D = \frac{\Sigma \varepsilon_i}{V N_E} = \frac{\Sigma \varepsilon_i}{V N_H} \frac{N_H}{N_E} \tag{5.3}$$

where V is the sensitive site volume (unit density), ε_i is the energy absorbed per site hit (referred to as the hit size of the i^{th} event), and N_E is the number of exposed sites. At low

Reproduced with permission of the copyright owner. Further reproduction prohibited without permission.

dose, not all sites are hit, so that the number of sites hit N_H is less than the number of sites exposed. Only as $N_H \rightarrow N_E$ is D meaningful in terms of individual cell response[67]. The fraction of sites that are hit at low exposure, that is $N_H << N_E$, is

$$\frac{N_H}{N_E} \approx \sigma_g \phi \qquad (5.4)$$

where σ_g is the site geometric cross section and ϕ is the charged-particle fluence within the tissue system. In reality, the nuclear cross section can be larger than the geometric cross section due to the δ-ray diffusion for which the number of site hits is increased by sites hit far from the ionizing particles path. The fluence ϕ is related to the macroscopic absorbed dose, D, and the value of LET, L, (unrestricted LET) as

$$\phi = 6.24\frac{D}{L} \qquad (5.5)$$

for ϕ in particles/μm^2, D in Gy, and L in keV/μm. The conversion factor 6.24 is for a tissue equivalent material (1Gy = 6.24 keV/μm^3). For γ-rays, L_γ corresponds to the secondary electrons generated and has a value of about 0.25 keV/μm. The corresponding ϕ_γ is an effective secondary electron fluence that is dependent on the photoabsorption coefficient and the γ-ray fluence.

The average hit size is given as

$$\bar{\varepsilon} = \sum_i \frac{\varepsilon_i}{N_H} \qquad (5.6)$$

and is known from basic physical principles and specifications of the site volume V. The mean number of hits per exposed site is then

$$\frac{N_H}{N_E} = \frac{DV}{\bar{\varepsilon}} \qquad (5.7)$$

and is related to the number of hit sites assuming Poisson statistics. $\bar{\varepsilon}$ is estimated from the theory of Xapsos et al.[68] for various ion types as shown in figures 31 and 32 for a 1 Gy

Reproduced with permission of the copyright owner. Further reproduction prohibited without permission.

exposure and a 0.1 μm site size corresponding approximately to the width of a single chromatin strand and its immediate environment. In figures 31 to 34, contributions from fragmenting nuclei of the biological target are ignored. The effect of site size is shown by comparing a 0.1 μm site size with a 0.5 μm site size in figures 33 and 34. Note that the hit size and average number of hits increase with the site size. Also shown in figure 35 are the most recently defined quality factors[62]. The region of unit quality factor ($L \leq 10$ keV/μm) for the 1 Gy exposure shown in figure 35 is characterized by a large fraction of sites hit (figures 32 and 34) with a fraction of 1 keV mean hit size (figures 31 and 33). The corresponding excess fatal cancer risk to this exposure would be about 3 percent. In comparison, the 100 keV/μm exposure has a quality factor around 20 to 30 and would result in an estimated 60 to 90 percent excess cancer risk. The mean hit size in this case is several tens of keV and a small fraction, less than 1 percent, of the sites are in fact hit. The HZE particles show a smaller mean hit size due to their range and δ-ray diffusion than the smaller ions at the same LET, but there is a corresponding increase in the number of sites hit. A further distinction of HZE exposure is that a clustered group of contiguous cells or sites is affected by a single ion passage due to their range and δ-ray diffusion[69] in comparison to smaller ions of the same LET.

The great variability of the microscopic fluctuations, expressed above as mean hit size and fraction of sites hit for various radiation field components, is aptly illustrated in figures 31 to 34. Although the meaning of this variability is somewhat represented by the quality factor as noted in the figure 35, an added distinctive feature of the HZE exposures

Reproduced with permission of the copyright owner. Further reproduction prohibited without permission.

is that large clusters of contiguous cells are affected. The radiation response of many of the GCR components is not yet understood, but surely the changes wrought by shielding materials on these microscopic fluctuations which will serve as the primary means of radiation protection and not a decline in the energy absorbed with the addition of shield material as shown in figure 30.

Reproduced with permission of the copyright owner. Further reproduction prohibited without permission.

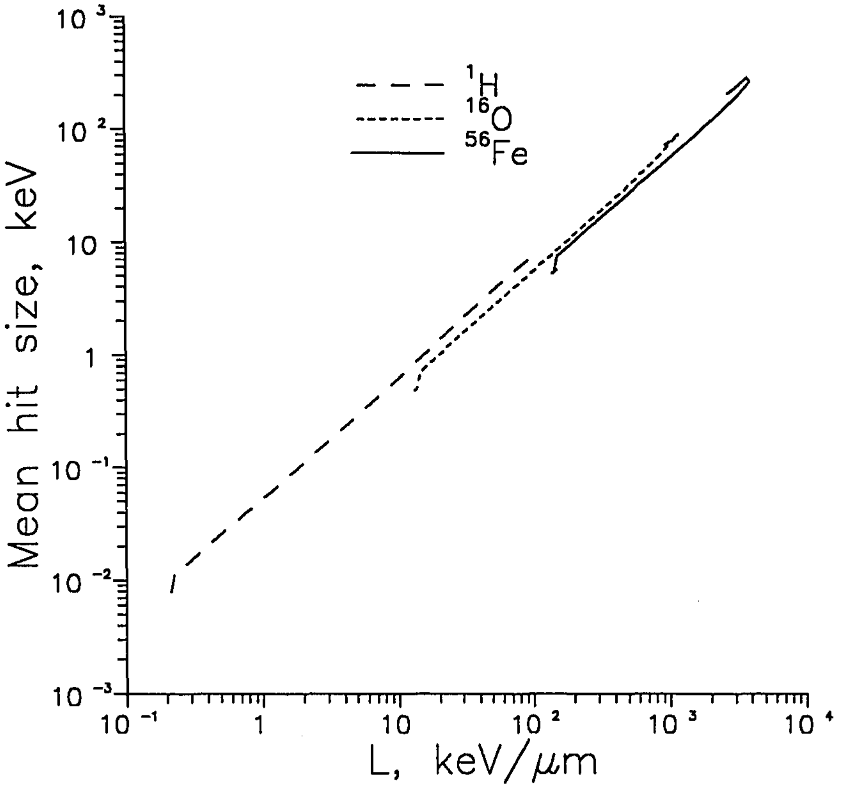

Figure 31. Mean hit size for various ion types as a function of LET (0.1 μm site size)

Reproduced with permission of the copyright owner. Further reproduction prohibited without permission.

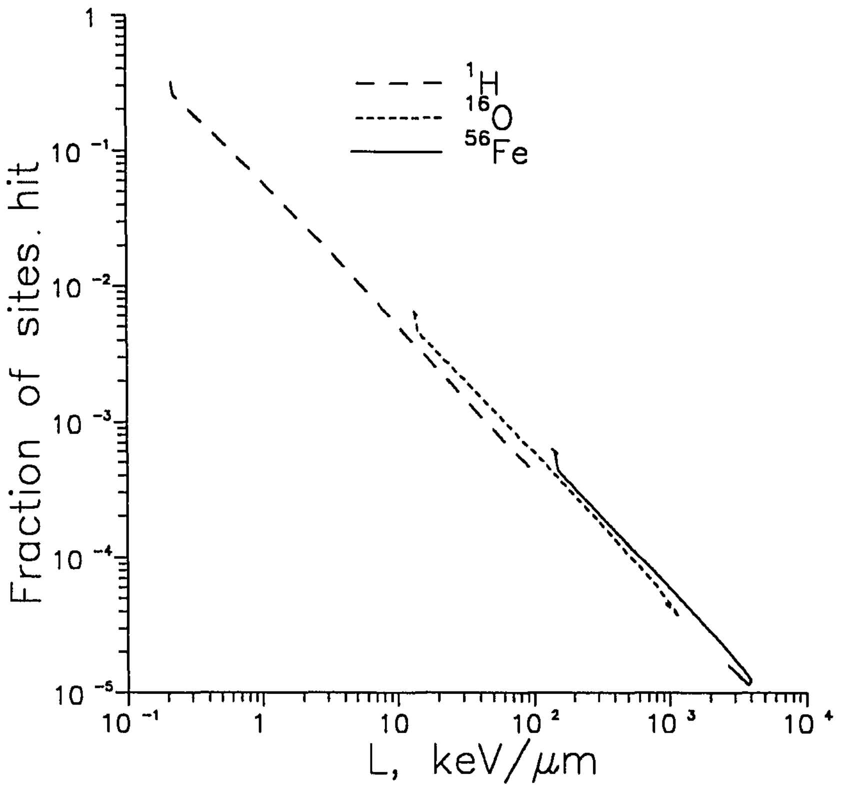

Figure 32. Fraction of sites hit for various ion types as a function of LET

(0.1 μm site size)

Reproduced with permission of the copyright owner. Further reproduction prohibited without permission.

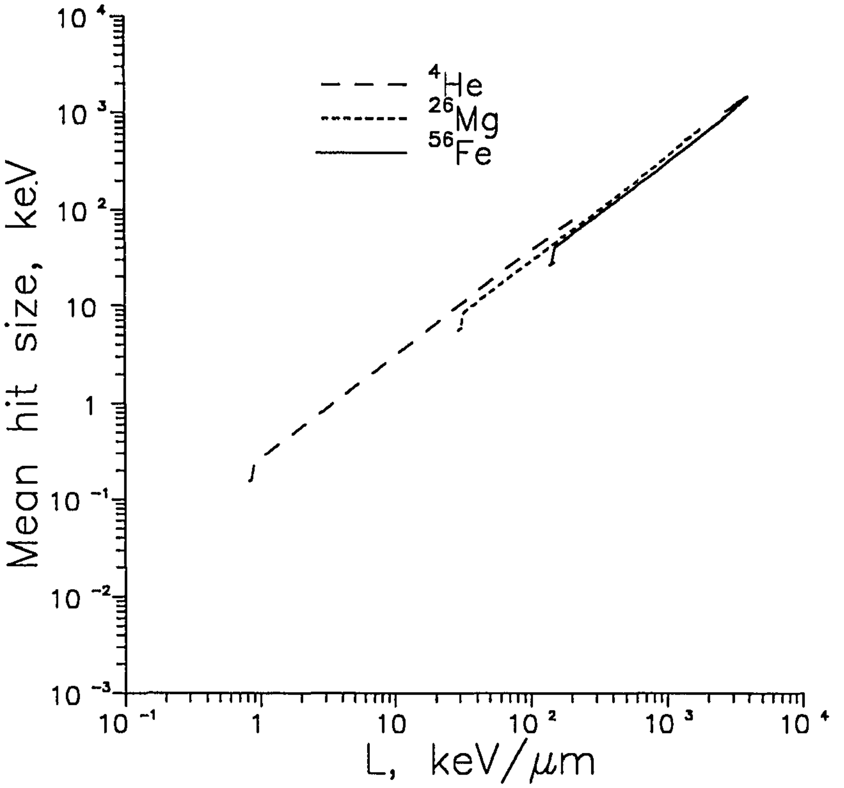

Figure 33. Mean hit size for various ion types as a function of LET (0.5 μm site size)

Reproduced with permission of the copyright owner. Further reproduction prohibited without permission.

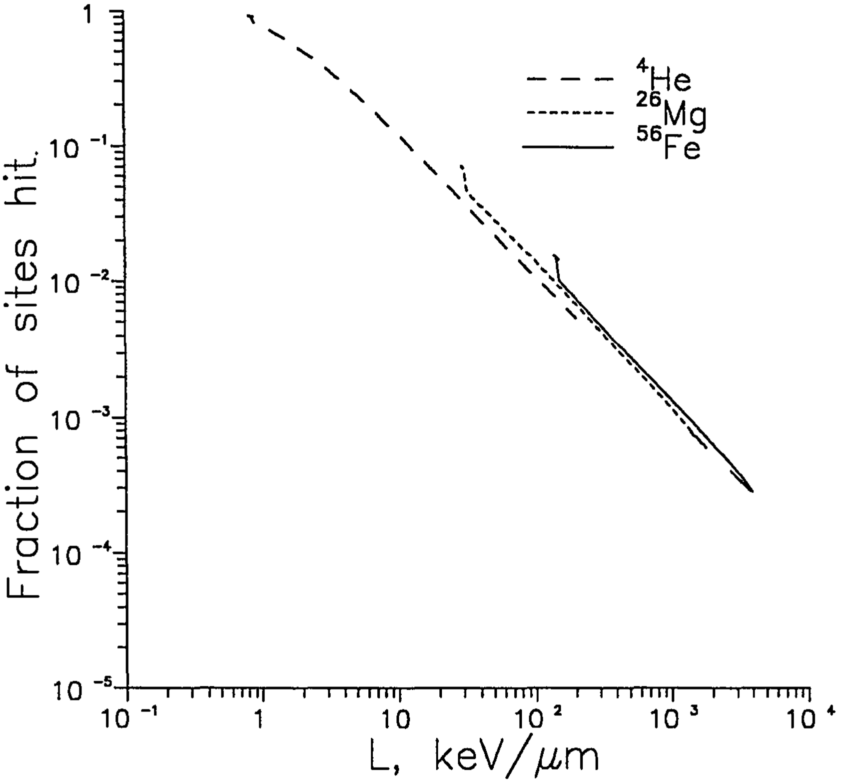

Figure 34. Fraction of sites hit for various ion types as a function of LET (0.5 μm site size)

Reproduced with permission of the copyright owner. Further reproduction prohibited without permission.

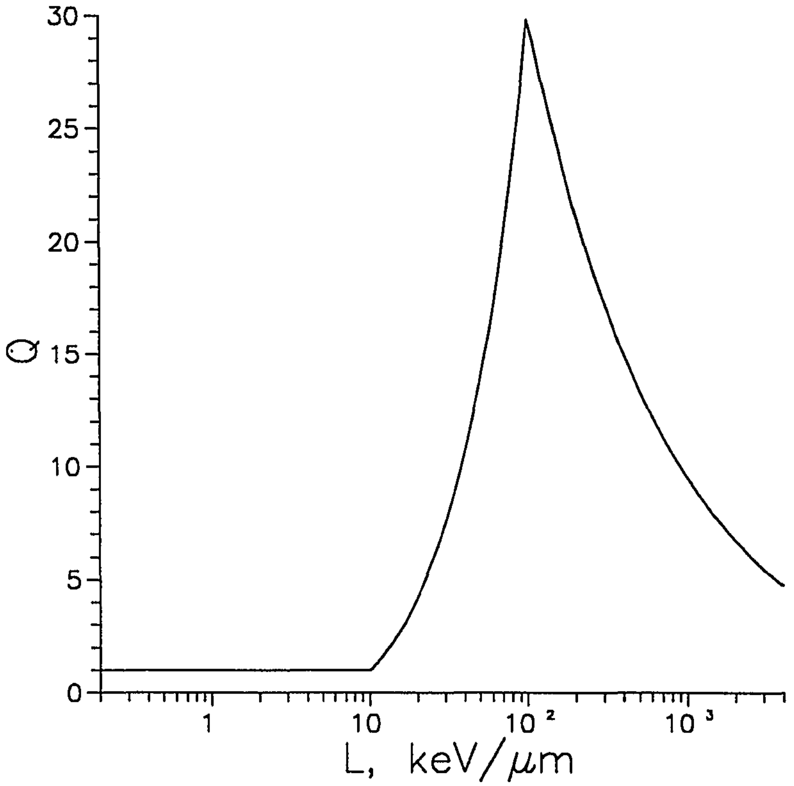

Figure 35. Quality factor as a function of LET

Reproduced with permission of the copyright owner. Further reproduction prohibited without permission.

5.2.1 Conventional Risk Assessment

Excess cancer risks in humans are estimated according to equation (5.1) based on coefficients derived from X-ray and γ-ray exposures. The conventional method of extrapolating the human database to high-LET exposures is to replace D_γ in equation (5.1) by the dose equivalent H given by

$$H = QD \tag{5.8}$$

where Q is the LET-dependent quality factor[62] shown in figure 35. Equation (5.8) follows from analogy with the relative biological effectiveness given for γ-ray and ion exposure levels D_γ and D_i which result in the same biological end point by

$$\text{RBE}=\frac{D_\gamma}{D_i}. \tag{5.9}$$

The quality factor is a defined function[62] chosen to represent trends of measured RBE in cell culture, plant, and animal experiments. The RBE values depend on end point, dose, dose rate, and quality of the radiation usually represented by LET. It is usually assumed that RBE reaches a maximum value denoted by $(\text{RBE})_M$ at a sufficiently low dose as related to the initial slopes of the response curves of each radiation type[14, 70]. Furthermore, the dose at which $(\text{RBE})_M$ is achieved is assumed to be dose rate dependent [66]. The values of RBE from which Q is defined as a function of LET are largely for high dose rates at the 0.1 Gy level of exposure for which fission neutrons have $\overline{Q} = 25$ corresponding to a γ-ray exposure of 2.5 Gy. RBE values for fission neutrons of lower level of exposure and/or lower dose rate are much larger[70], as shown in table 9, and occur for lower exposure and

Reproduced with permission of the copyright owner. Further reproduction prohibited without permission.

dose rate than were used in deriving Q. Since the achievement of $(\mathrm{RBE})_M$ is accelerated at low dose rates, the RBE values in table 9 may, in fact, be more appropriate for space exposures. This is one source of the rather large uncertainties in space radiation exposure risks. The second source of uncertainty concerns the response to HZE exposures for which little is known. It is postulated that there are possible single ion track effects for which γ-ray exposures have no analog. One such mechanism was suggested by Todd[69] in which cells exposed at 0.25 Gy outside the track core have a high probability of being transformed, while the dead cells of the track core must be replaced, causing promotion to a cancer growth by this one event. The RBE for such effects is undefined (infinite) and extrapolation from the human database is not possible.

The use of an LET-dependent quality factor as related to dose equivalent implies additivity of diverse components in estimating risk. Such assumptions may underestimate the actual risk as was discussed by Scott[72]. However, risks associated with different time intervals are not additive, especially if radiation proves to be an effective promotion factor in carcinogenic response[73]. For low LET particles, substantial repair is often operative which results in reduced risk. For high LET exposures, there are possible dose rate enhancement effects in which risk is substantially increased at lower dose rates[74].

The uncertainties in radiation-induced risk have been estimated in the NASA Space Radiation Health Program[61]. In their estimate, the risk is assumed to be related to the total value of dose equivalent. This assumes that the dose response curve is of similar shape for

Reproduced with permission of the copyright owner. Further reproduction prohibited without permission.

Table 9. $(\mathrm{RBE})_M$ for fission neutrons

Tumor induction	~3 - ~200
Life shortening	15 - 45
Transformation	35 - 70
Cytogenic studies	40 - 50
Genetic endpoints in mammalian systems	10 - 45
Other endpoints	
Lens opacification	25 - 200
Micronucleus assay	6 - 60
Testes weight loss	5 - 20

Reproduced with permission of the copyright owner. Further reproduction prohibited without permission.

each radiation component which at low dose and dose rate is linear. The excess risk, that is the added risk due to exposure, is then

$$R = k_\gamma H = k_\gamma(H_x + H_Z) \tag{5.10}$$

where k_γ is the sensitivity coefficient, H is the dose equivalent in Sv, H_x is the component of dose equivalent due to low-LET radiation, and H_Z is the dose equivalent due to the HZE component of the radiation. A further approximation is made that the uncertainties in k_γ and H_x are negligible in comparison with the uncertainty in H_Z. With this, one obtains from equation (5.10)

$$\Delta R = k_\gamma \Delta H \approx k_\gamma \Delta H_Z = k_\gamma \frac{\Delta H_Z}{H_Z} H_Z \equiv k_\gamma U H_Z \ , \tag{5.11}$$

so that the net effect of the uncertainty in R is to increase the relative risk, which becomes

$$R + \Delta R = k_\gamma H + k_\gamma U H_Z = k_\gamma H_U . \tag{5.12}$$

This equation defines an effective dose equivalent, H_U, corresponding to the increased risk due to uncertainties. If a limit, $\mathcal{L}$, is defined on the basis of excess risk R, then it is required that

$$R + \Delta R \leq \mathcal{L} \tag{5.13}$$

where $\mathcal{L}$ is the defined limit of acceptable risk. A safety factor, S, can be defined with reference to equation (5.12). Let S be an upper bound on the estimated value of the uncertainty in HZE dose equivalent, so that $S=nU$, where $n=1,2...$ corresponds to the number of standard deviations required to establish an acceptable safety margin. Then equation (5.12) becomes

$$R + \Delta R = k_\gamma H + k_\gamma S H_Z = k_\gamma H_S \tag{5.14}$$

where the effective dose equivalent, including the safety factor, is given by $H_S=H+SH_Z$.

Alternatively, the HZE component in equation (5.10) can be increased as

$$H'_Z=H_Z+SH_Z=(1+S)H_Z. \tag{5.15}$$

Reproduced with permission of the copyright owner. Further reproduction prohibited without permission.

This formulation suggests the possibility of using the ratio between experimental values of RBE as appropriate for GCR exposure and $\bar{Q}$ as an approximation for 1+S, so that

$$H_z' = (1+S)H_z \sim \frac{RBE}{\bar{Q}} H_z \ . \tag{5.16}$$

For example, the measured RBE for life shortening in mice has been reported to be as large as 80 for fission neutrons[74], while the estimated value of $\bar{Q}$ is on the order of 20. Thus, an estimate for the value of S would be 3 from equation (5.16) which corresponds to an effective dose equivalent 300 percent greater for HZE exposure than would be obtained from currently accepted conventional dosimetric analyses. Such a value of 300 percent might be considered reasonable from a radiobiological point of view and may not be too restrictive on mission design and operations[71].

In the present study, the uncertainty is ignored in risk estimates, i.e., S=0 and the quality factor, $\bar{Q}$, is applied in estimating the dose equivalent that is assumed to be linearly related to risk. The variation of dose equivalent with shield thickness and composition will be one means of estimating shield effectiveness.

Reproduced with permission of the copyright owner. Further reproduction prohibited without permission.

5.2.2 Track-Structure Repair Model

Although the use of quality factors may give some indication of the attenuation of biologically important components, their use in space protection against HZE particles has specifically not been recommended[14] and a test biological system is considered below for the study of shield properties. Ionizing radiation interacts with matter through the formation and interaction of radicals called nascent lesions. These highly active chemical species may result in structural changes occurring within the DNA which cannot be repaired by enzymatic processes. Then, subsequent generations may exhibit new characteristics, or the cell may be unable to undergo cell division in which case, clonogenic death occurs.

There are many ways in which the DNA could be changed to cause cell death but only a few specific changes are allowed to reach other biological end points. First, those lesions are treated which lead to cell death. Kinetic equations[64] are written for the time development of the cell population $n_i(t)$ with i-fold lesions as

$$\dot{n}_0 = \sum_{i=1}^{\infty} \alpha_{r_i} n_i - k n_0 \tag{5.17}$$

$$\dot{n}_i = \sum_{j=0}^{i-1} k_{i-j} n_j - k n_i - \alpha_i n_i \tag{5.18}$$

$$\dot{n}_d = \sum_{i=1}^{\infty} \alpha_{m_i} n_i \tag{5.19}$$

Reproduced with permission of the copyright owner. Further reproduction prohibited without permission.

where the k_i are proportional to the charged particle flux of primary and secondary radiations, α_{r_i} are the repair rates, α_{m_i} are the misrepair rates, and n_d is the population of misrepaired cells. Conservation of cells within a given cell cycle requires k=k_1+k_2+... and $\alpha_i = \alpha_{r_i} + \alpha_{m_i}$. The ratio $\alpha_{r_i}\alpha_i^{-1}$ is the kinetic repair efficiency and m_d is the smallest i for which the repair efficiency is zero.

The k_i kinetic coefficients are related to the Katz model[75] for the highly repair-efficient stationary G_1 phase cells as

$$k_1 = (m_d!)^{\frac{1}{m_d}} \dot{D}_\gamma / D_0 \tag{5.20}$$

$$k_{m_d} = \sigma\phi \tag{5.21}$$

where all other k_i's are taken as zero[45, 76]. The remaining quantities are all given by Katz as

$$\dot{D}_\gamma = \left(1 - \frac{\sigma}{\sigma_0}\right) L\phi \tag{5.22}$$

where ϕ is the local charged particle flux of primary and secondary radiations, L is their corresponding LET, and σ is approximated using the Katz model[64]. σ_0 is Katz "saturation" value of the cross section[75] as given in table 10.

The cellular track model of Katz et al.[75] attributes biological damage from energetic ions to the secondary electrons (δ-rays) produced along the ion's path. The effects caused by energetic ions are correlated with those of γ-rays by assuming that the response in sensitive sites near the ion's path is part of a larger system irradiated with γ-rays at the same dose. The response due to ion effects is then approximately related to the γ-ray response and the δ-ray dose surrounding the ion's path. For a core of the ion track with the number of hits m, the inactivation of cells by γ rays is assumed to follow a

Reproduced with permission of the copyright owner. Further reproduction prohibited without permission.

Poisson distribution reflecting the random accumulation of sublethal damage, with a radiosensitivity parameter D_0.

For the inactivation of cells by ions, two models are identified: "ion-kill" which corresponds to intratrack effects and "gamma-kill" which corresponds to intertrack effects. Here, the ion-kill mode is unique to ions corresponding to single particle inactivation of cells described by the cross section σ. The inactivation cross section for a sensitive site whose response to radiation is ahistoric is determined as[64]

$$\sigma = \int_0^\infty 2\pi t \, dt \, (1 - e^{-\overline{D}/D_0})^m \tag{5.23}$$

where $\overline{D}$ is the average dose at the sensitive site from the ion's δ-rays. The evaluation of the cross section is separated by Katz, et al.[75], into a so-called grain-count regime, where inactivation occurs randomly along the path of the particle, and into the so-called track-width regime, where many inactivations occur and are said to be distributed like a "hairy-rope". In the grain-count regime, σ may be parameterized as[64]

$$\sigma = \sigma_0 (1 - e^{-Z^{*2}/\kappa\beta^2})^m \tag{5.24}$$

where σ_0 is the Katz "saturation" value of the cross section. The effective charge number, Z^*, is given by[64]

$$Z^* = Z(1 - e^{-125\beta/Z^{2/3}}) \tag{5.25}$$

where β is the ion velocity in units of the velocity of light, and the parameter κ is a non-dimensional size parameter related to the radius of the sensitive site, a_0, by

$$D_0 \, a_0^2 / \kappa \cong 2 \times 10^{-7} \text{erg/cm} \tag{5.26}$$

The transition from the grain-count regime to the track-width regime is observed to take place at a value of $Z^{*2}/\kappa\beta^2$ about 4; at lower values it is in the grain-count regime and at

Reproduced with permission of the copyright owner. Further reproduction prohibited without permission.

higher values the track-width regime. The fraction of the cells damaged in the ion-kill mode[45] is $P = \sigma/\sigma_0$. Note that in the track-width regime $\sigma > \sigma_0$ and it is assumed that $P = 1$. The track model assumes that a fraction of the ion's dose, (1-P), acts cumulatively with that for other particles to inactivate cells in the gamma-kill mode[45].

The repair coefficients are found to be cell phase dependent and the G_1 phase repair efficiencies are near the maximum for $i < m_a$ and near zero otherwise. In analyzing the repair-dependent experiments of Yang et al.[65], one sees that the exponential population shows a relatively high single-lesion repair efficiency and much lower multiple-lesion repair efficiencies as shown in table 10. These results are compared between the G_1 phase repair-enhanced exposures and exponential phase repair exposures for various ions[64] and with X-ray fractionated exposures[65]. The G_1 phase repair-enhanced exposures are performed using the process of delayed *plating* in which G_1 exposed cells are delayed in the G_1 phase for 24 hours after exposure[66]. In exponential phase repair exposures, there is immediate *plating* whereby G_1 exposed cells are separated and immediately introduced to nutrients after exposure. This model is used to study the functional dependence of RBE at low total dose and low dose rate for the G_1 phase and exponential phase repair processes.

Special solutions of equations (5.17) to (5.19) are considered for an exposure field with a low constant dose rate ($\alpha_i >> k_j$ for all i, j). At low dose rates the populations of cells with lesions can be approximated as[64]

$$n_1(t) \approx k_1\, n_0(t)/\alpha_1 \tag{5.27}$$

$$n_2(t) \approx k_1^2\, n_0(t)/\alpha_1\alpha_2 \tag{5.28}$$

Reproduced with permission of the copyright owner. Further reproduction prohibited without permission.

$$n_3(t) \approx (k_1^3/\alpha_1\alpha_2\alpha_3 + k_3/\alpha_3)\, n_0(t) \tag{5.29}$$

In the case of low total exposure, $n_0(t)$ may be taken as constant and the accumulation of misrepaired cells is written as[64]

$$\frac{n_m(t)}{n_0} \approx \frac{\alpha_{m_1}}{\alpha_1} 6^{\frac{1}{3}} \frac{(1-P)D}{D_0} + \frac{\alpha_{m_2}}{\alpha_2} 6^{\frac{2}{3}} \frac{(1-P)^2 \dot{D} D}{D_0^2 \alpha_1} + \frac{\alpha_{m_3}}{\alpha_3} 6 \frac{(1-P)^3 \dot{D}^2 D}{D_0^3 \alpha_1 \alpha_2} + \frac{\alpha_{m_3}}{\alpha_3} \frac{\sigma}{L} D \tag{5.30}$$

where $\dot{D}$ is the dose rate and $P = \sigma/\sigma_0$. In the case of an exponential population $\frac{\alpha_{m_1}}{\alpha_1} \approx 0.3$ so that the first term is always dominant over the second and third term for very low dose rate exposures[64] ($\dot{D}\alpha_i^{-1} << D_0$). The $(\mathrm{RBE})_{\mathrm{M}}$ is found to be

$$(\mathrm{RBE})_{\mathrm{M}} = 1 - P + 6^{-\frac{1}{3}} \frac{\alpha_{m_3}}{\alpha_3} \frac{\alpha_1}{\alpha_{m_1}} \frac{\sigma}{L} D_0 \tag{5.31}$$

as was found for the earlier result[76]. If the repair efficiency of the G_1 phase is high ($\frac{\alpha_{m_1}}{\alpha_1} << \frac{\dot{D}}{\alpha_i D_0}$) then the higher order terms of equation (5.30) cannot be ignored in determining RBE for which there are important dose rate dependent factors whenever $\dot{D} >> \alpha_i D_0 \approx 0.01\,\mathrm{Gy\ min^{-1}}$. At much lower dose rates, $\dot{D} << 0.01 \frac{\alpha_{m_1}}{\alpha_1}\,\mathrm{Gy\ min^{-1}}$, the $(\mathrm{RBE})_{\mathrm{M}}$ given by equation (5.31) is obtained. A parameter study shows that when $\frac{\alpha_{m_1}}{\alpha_1} < 0.03$, the repair efficiency is 97 percent as noted in table 10.

In exposures to galactic cosmic rays, the dose rate is very small,

$$\dot{D} \approx 0.5\ \mathrm{mGy\ min^{-1}} << \alpha_i D_0 \approx 10\ \mathrm{mGy\ min^{-1}}\ , \tag{5.32}$$

and the nonsurviving fraction of cells is[64]

$$\frac{n_m(t)}{n_0} \approx \frac{\alpha_{m_1}}{\alpha_1} 6^{\frac{1}{3}} \frac{(1-P)D}{D_0} + \frac{\alpha_{m_3}}{\alpha_3} \frac{\sigma}{L} D\,. \tag{5.33}$$

Note that $(1 - \alpha_{m_1}\alpha_1^{-1})$ and $\alpha_{m_1}\alpha_1^{-1}$ are the branching ratios of the reaction for completely repaired and completely misrepaired states respectively. The fraction of transformed cells in the low dose rate limit is given by the same functional form as $n_m(t)/n_0$ with appropriate kinetic parameters for transformation. The low dose rate limit parameters are given in table 10.

Reproduced with permission of the copyright owner. Further reproduction prohibited without permission.

Table 10a. Survival repair rates (hr^{-1}) and repair efficiency

	G_1 Phase			Exponential Phase		
i	1	2	$\geq m_d$	1	2	$\geq m_d$
α_i	0.25	.125	$< .08$	.25	.125	$< .08$
$\alpha_{ri}\alpha_i^{-1}$	$> .97$	$> .84$	~ 0	.7	.118	~ 0

Table 10b. Katz C3H10T1/2 cell parameters

	σ_0, cm^2	k	m_d	D_0, Gy
Survival	$5\text{x}10^{-7}$	750	3	2.8
Transformation	$7\text{x}10^{-11}$	475	3	150

Table 10c. Transformation repair rates (hr^{-1}) and repair efficiency

	G_1 Phase			Exponential Phase		
i	1	2	$\geq m_d$	1	2	$\geq m_d$
α_i	.25	.125	≤ 0.08	.25	.125	≤ 0.08
$\alpha_{ri}\alpha_i^{-1}$	1.0	1.0	0.0	.99	.70	0.0

Reproduced with permission of the copyright owner. Further reproduction prohibited without permission.

5.3 Shield Material Characteristics

Shielding the work area of an astronaut crew will always result in a wall thickness that is small in comparison with the linear dimension of the crew compartment. The shield mass is proportional to the areal density (g/cm^2) which is the appropriate measure of shield thickness.

Shield properties depend on the basic atomic/molecular and nuclear cross sections. Atomic/molecular stopping cross sections depend on the number of electrons per unit volume, the electron mean excitation energy, and binding corrections for the inner shell electrons. Materials with the most electrons per unit mass, the least mean excitation energy, and the lowest binding corrections make the best energy absorbers. Thus, liquid hydrogen is the best material while lead is much less efficient as an energy absorber[47]. For example, a 825 MeV/amu iron ion will come to rest in 10 g/cm^2 of liquid hydrogen but requires 38 g/cm^2 of lead[77].

The nuclear cross sections relate not only to the mean free paths for nuclear reactions but to the nature of the reaction products. The total nuclear cross section projected by the nuclei in a unit mass of material (cm^2/g) is the appropriate parameter for nuclear interaction. The nature of the reaction products is equally important. In the

Reproduced with permission of the copyright owner. Further reproduction prohibited without permission.

production cross sections per unit mass of shield at high energy, the low Z-shields are favored because of the short mean free paths of the particle[47].

The microscopic fluctuations in the energy absorption events of several ions are represented parametrically as a function of LET in figures 31 to 34. Although LET is a less than perfect indicator of the microscopic damage, it is a useful physical quantity to indicate "radiation quality", is still the focus of many biological investigations, and serves as the basis of conventional radiation protection practice[62]. The transmitted differential LET spectra for GCR particles through four shield materials are shown in figures 36 to 39. The attenuation of the highest LET components is seen in each material with liquid hydrogen being the most efficient and lead the least. The left hand discontinuities are associated with the minimum ionization at relativistic energies for each ion type[46]. The left most discontinuity at 0.2 keV/μm is due to the hydrogen isotopes followed by helium at 0.8 keV/μm and so on through the nickel isotopes. The smaller right hand discontinuities are associated with maximum ionization in the stopping region (Bragg peak). For example, the first such peak at 100 keV/μm is due to the hydrogen isotopes, and the second peak at 200 keV/μm is due to the helium isotopes. It was once thought that the ions in the stopping region may be the primary hazard[12]. Figures 36 to 39 show that these stopping ions make a rather small contribution to the total exposure. Beyond the Bragg peak, there is a significant buildup of secondary particles, since the secondary lighter ions penetrate to large depths. The quality factor of these secondary particles is not always smaller than that of the primary ions, because the maximum quality factor is at an LET

Reproduced with permission of the copyright owner. Further reproduction prohibited without permission.

value around 100 keV/μm. Thus, the total exposure would increase beyond this stopping region. A factor of 2-3 uncertainty exists for the LET region above 100 keV/μm due to uncertainty in the nuclear cross sections[78]. Adding energy dependence in the nuclear cross sections results in a 50 percent increase above 100 keV/μm[42, 54]. From figure 38 one sees that ,e.g., for 30 g/cm^2 of shielding the particles with LET less than 10 keV/μm are more abundant while those with greater LET are less abundant. This defines 10 keV/μm as a pivotal LET for that shield thickness. This pivotal LET value, above which the differential LET values decrease and below which they increase as a shield thickness increases, is a function of the shield composition increasing to 40-50 keV/μm for lead and less than 1 keV/μm for liquid hydrogen. The pivotal LET value is associated with the loss and production of a given species by nuclear events. The pivotal LET is thus a useful parameter in the consideration of the microscopic energy absorption events which ultimately affects biological response. Clearly, the shield effectiveness for biological exposure is intimately related to the nature of the nuclear cross sections. Although the absolute human risk is not known due to biological uncertainty, the relative effectiveness of added shielding under two diverse model types will be judged.

Reproduced with permission of the copyright owner. Further reproduction prohibited without permission.

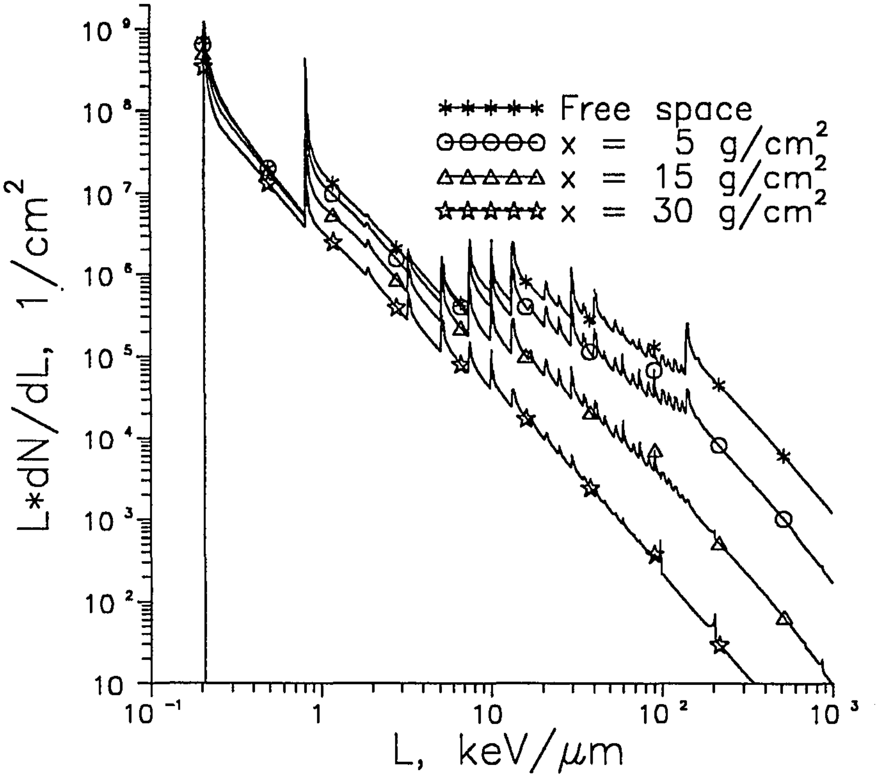

Figure 36. Annual transmitted GCR differential LET spectrum (Liquid hydrogen)

Reproduced with permission of the copyright owner. Further reproduction prohibited without permission.

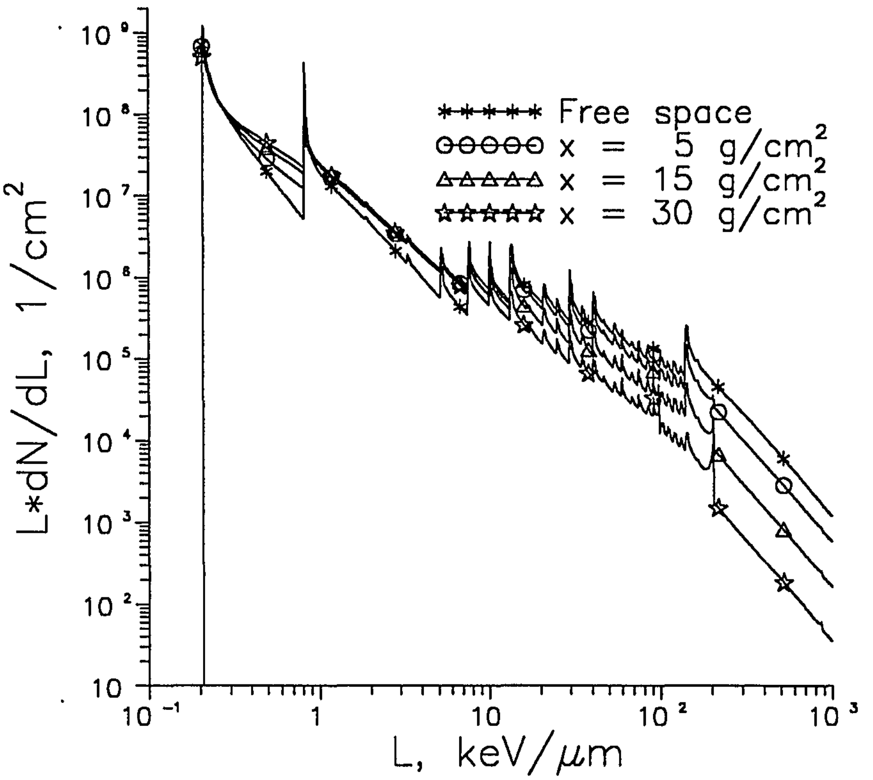

Figure 37. Annual transmitted GCR differential LET spectrum (Water)

Reproduced with permission of the copyright owner. Further reproduction prohibited without permission.

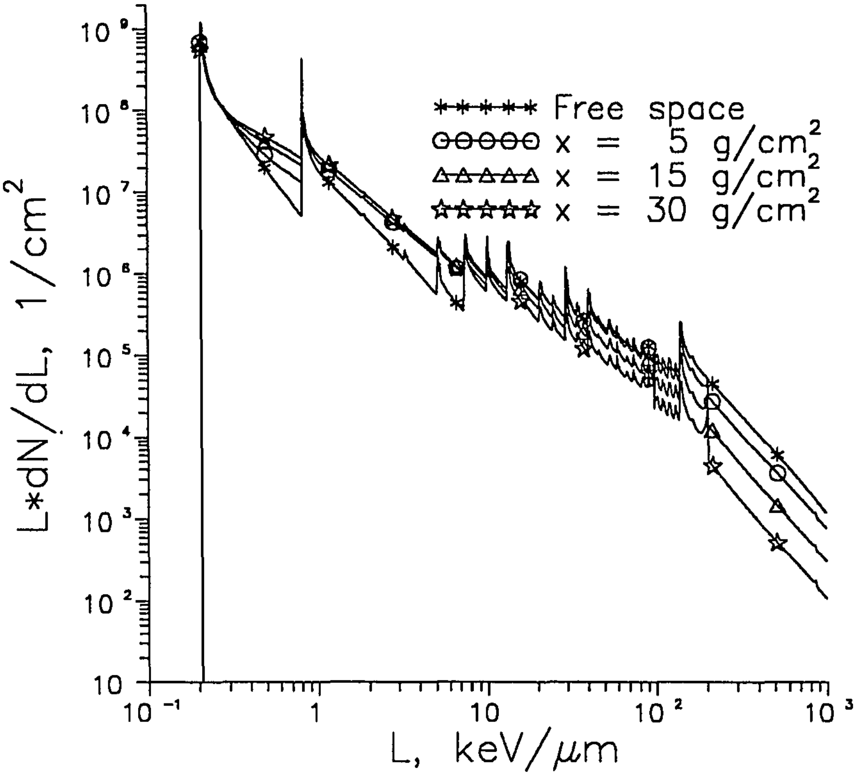

Figure 38. Annual transmitted GCR differential LET spectrum (Aluminum)

Reproduced with permission of the copyright owner. Further reproduction prohibited without permission.

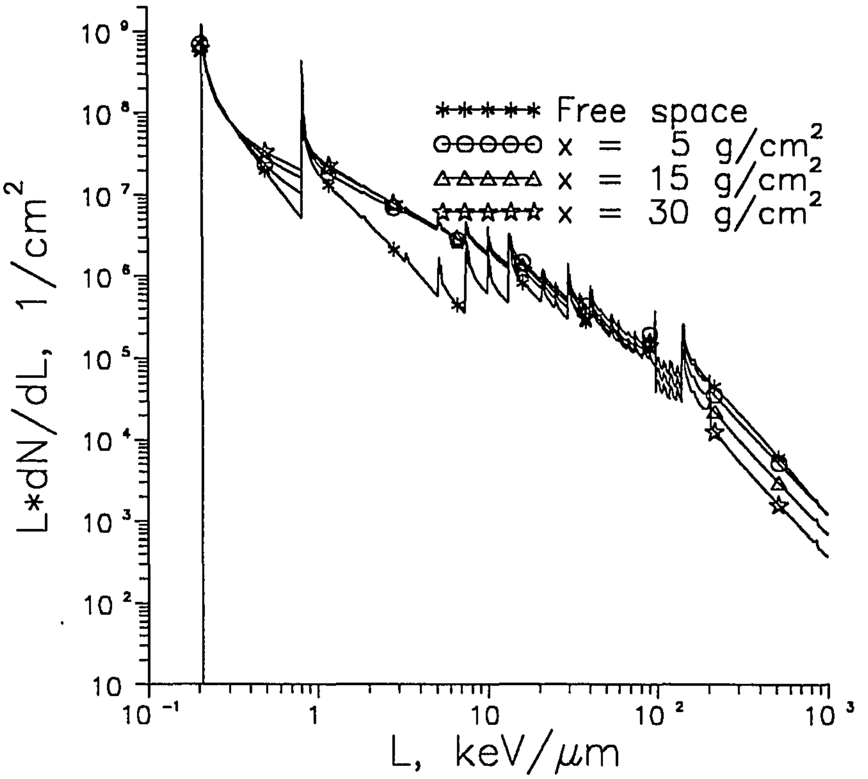

Figure 39. Annual transmitted GCR differential LET spectrum (Lead)

Reproduced with permission of the copyright owner. Further reproduction prohibited without permission.

5.3.1 Illustrations of Shield Effectiveness

Shield material characteristics are examined in terms of two biological models above in section 5.2. The first model is the conventional risk assessment method[62] and uses quality factor as a function of LET. The second model is a track-structure repair kinetic model[64] for the mouse cell C3H10T1/2 for which there is a large body of experimental data with various ions in which repair kinetic studies were made[65, 66]. The shield effectiveness is evaluated as a function of the shield mass necessary to reduce the biological effects using these biological response models.

The first illustration is found using the conventional risk assessment method. The distribution of particle fluence behind a 5 g/cm^2 aluminum shield is converted to distribution of absorbed dose over the same LET intervals[54] as shown in figure 40. Then, the dose equivalent distribution is obtained by multiplying the absorbed dose at each LET by the corresponding quality factor[62] as shown in figure 35. The quality factor estimates the effect of a few cells being hit with large mean hit size by high LET components. A large contribution to dose equivalent results from ions in the LET interval from 10 to 10^3 keV/μm. These are the most significant components by conventional dosimetry.

Reproduced with permission of the copyright owner. Further reproduction prohibited without permission.

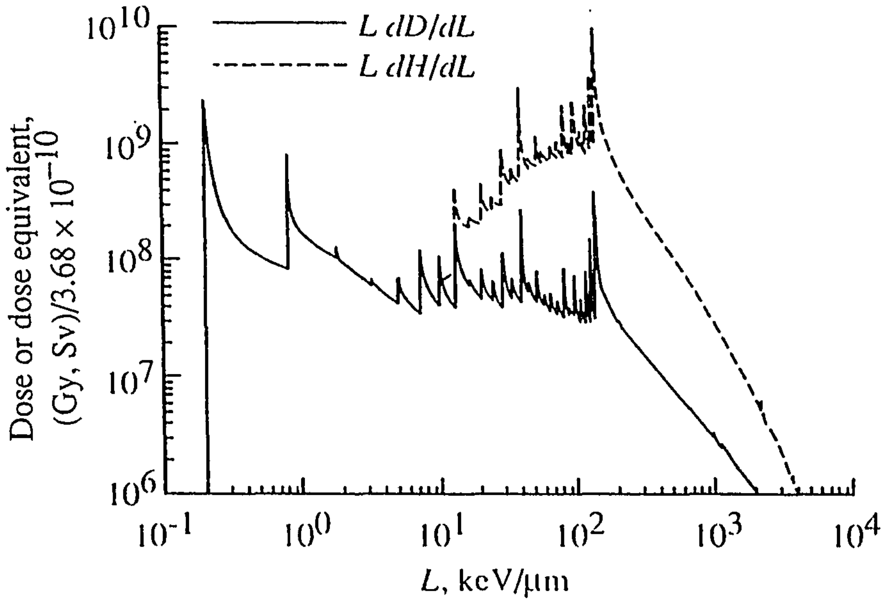

Figure 40. Differential LET-spectra for annual dose and dose equivalent with 5 g/cm^2 aluminum shield

Reproduced with permission of the copyright owner. Further reproduction prohibited without permission.

The relative attenuation of dose equivalent as a function of areal density, $H(x)/H(0)$, is shown in figure 41. It is clear that modification of the LET distribution depends upon the shield composition. Lead shielding in which the LET pivot point is near the peak of the LET contributions to dose equivalent is a poor shield material for the GCR environment. Clearly, the lower the LET pivot point, the better is the shield performance of the material. On this basis, liquid hydrogen is the optimal selection. Liquid hydrogen is of course a difficult material to use because its low boiling temperature. For practical spaceflight, it is important to evaluate less than optimal shield materials which are more useful in vehicle construction. Furthermore, the adequacy of results derived using quality factors to represent biological systems is still in question for HZE particles.

A second illustration is found using a model for the survival and neoplastic transformation of the C3H10T1/2 mouse cell for which there is sufficient experimental data for developing a reasonable model[64]. Unlike conventional dosimetric analysis, the repair kinetics model is driven by track-structure dependent injury coefficients. The cellular repair kinetics model was solved at low dose rate for a one-year exposure behind the four shields shown in figures 36 to 39. The geometric hit frequency, the initial level of cell injury, and the unrepaired cell injury leading to clonogenic death in a C3H10T1/2 mouse cell population were calculated[64] as shown in figure 42. This figure shows that, although the cell is most often hit by protons and helium ions, the probability of injury is small and the repair efficiency is high, with little permanent injury[64]. Conversely, silicon and iron ions have a high probability of injury and a near-zero efficiency of repair. As a

Reproduced with permission of the copyright owner. Further reproduction prohibited without permission.

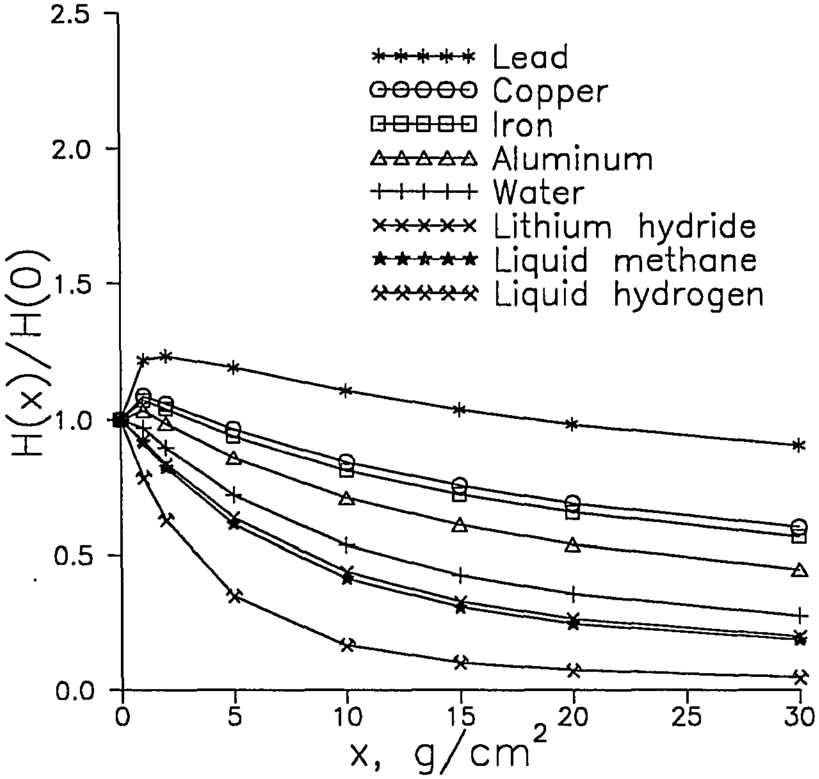

Figure 41. Attenuation of biological effects for a year exposure of GCR behind various materials (Dose equivalents)

Reproduced with permission of the copyright owner. Further reproduction prohibited without permission.

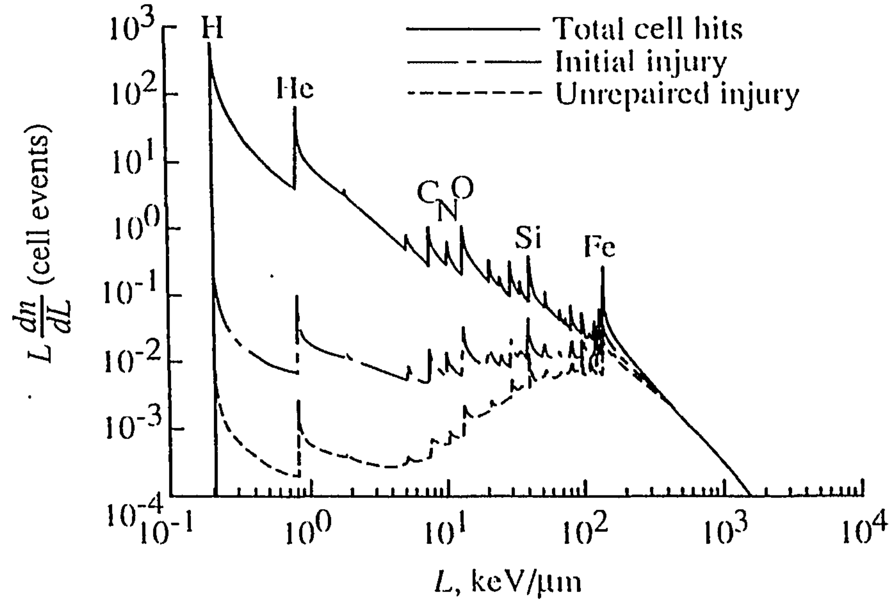

Figure 42. Differential LET contributions to cell events in one year exposure behind 5 g/cm^2 aluminum

Reproduced with permission of the copyright owner. Further reproduction prohibited without permission.

consequence, most clonogenic death from GCR exposure comes from ions with LET above 10 keV/μm (ions above relativistic carbon). Radiation injury from these ions shows minimal cellular repair. Although the two biological models are qualitatively similar in the degree of injury from various LET components, there are important track structure dependent differences. As a result, dose protraction, which is an extended exposure period for the same accumulated dose, will be less effective in reducing the biological response for GCR exposure.

The relative change in radiation-induced transformations, the ratio of $T(x)$ behind a shield of thickness x to $T(0)$ in free space, for a one-year exposure in space is shown in figure 43. Although the attenuation characteristics for various shield materials are qualitatively similar to the attenuation of dose equivalent shown in figure 41, there are important quantitative differences. This is best seen in terms of the attenuation of the transformation rate in a given material compared with attenuation of the dose equivalent in the same material. The relative attenuation for transformation rate and dose equivalent are plotted in figure 44 for the data shown in figures 41 and 43. If the dose equivalent represented the neoplastic transformation data, then all curves in figure 44 would lie on a single line with unit slope. Here, only liquid hydrogen shows good correlation between the two biological models. Therefore, the dose equivalent is not adequate to represent the neoplastic transformation yield for the other shield materials.

Reproduced with permission of the copyright owner. Further reproduction prohibited without permission.

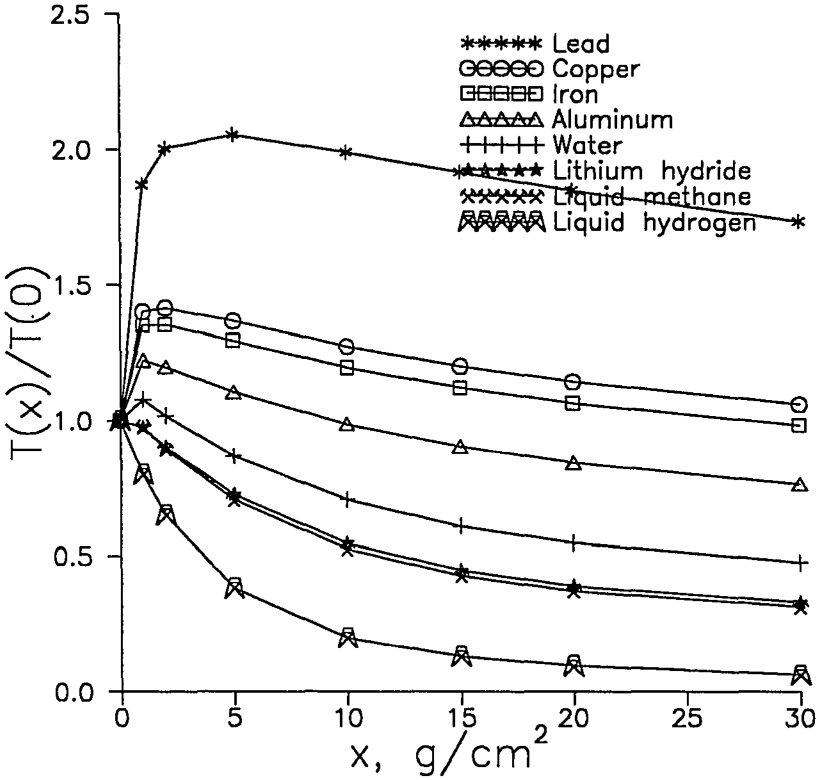

Figure 43. Attenuation of biological effects for a year exposure of GCR behind various materials (Cell transformations)

Reproduced with permission of the copyright owner. Further reproduction prohibited without permission.

The rates of attenuation of biological effects as estimated by the two risk models are similar only for the liquid hydrogen shield, because the hydrogen shield reduces all LET components above a few keV/μm (LET pivotal value). This implies that the ICRP60[62] quality factor in some way represents the dependence on radiation quality in this case. The LET pivotal value increases with the shield atomic number, and the mixture of ion charge and LET are radically altered for different materials. The two biological response models show greatly different results for non-hydrogenous shields as shown in figure 44. The quality factor is less useful for shields containing non-hydrogenous components and is a poor indicator for lead shields to represent the neoplastic transformation ratio. Very similar results are found for clonogenic death of the C3H10T1/2 cells as well[64]. What is very clear from figure 44 is that the use of local materials, such as regolith, for a lunar surface operations or space exploration shielding designs based on quality factors remains in great doubt.

Reproduced with permission of the copyright owner. Further reproduction prohibited without permission.

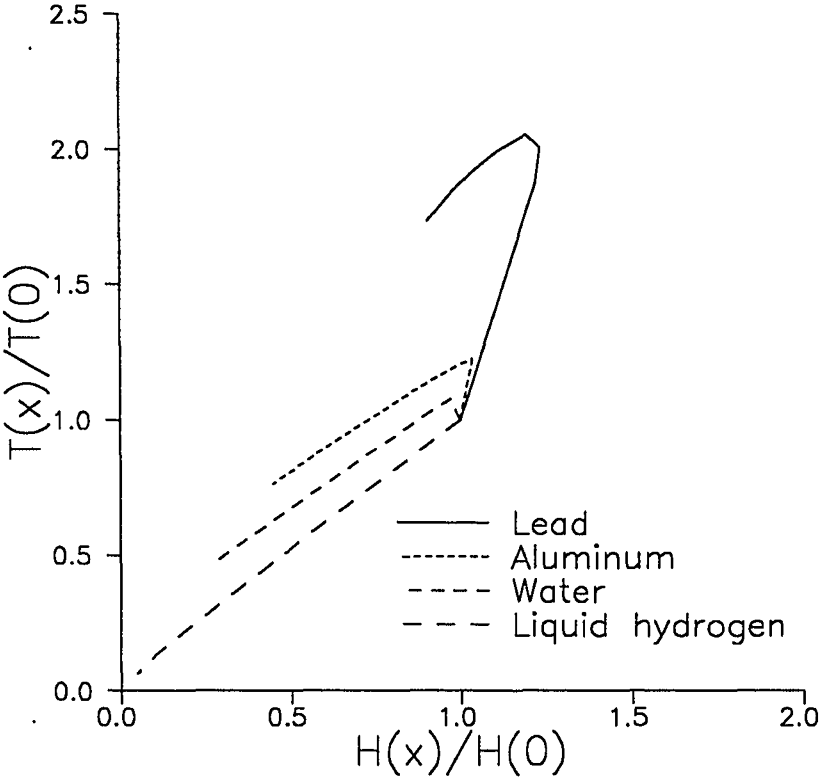

Figure 44. Correlation of biological response models in various materials

Reproduced with permission of the copyright owner. Further reproduction prohibited without permission.

5.3.2 Proposed Shield Performance Index

To assign a quantitative measure of shield performance[44], a track structure kinetics model of the C3H10T1/2 cell system is considered for clonogenic death and neoplastic transformation[64]. This model is evaluated for a one-year exposure for various shield materials at the various depths. Results are shown in figure 43. Note that the depths in units of areal density are proportional to the total shield mass of a large shielded region. The exposure conditions assume a stationary G_1 phase exposure for a constant dose rate over a 1-year period. The cell transformation behind an aluminum shield of areal density x, T_{Al}, compared to that for a different material of the same areal density, $T_m(x)$, is taken as a cell-transformation ratio.

$$\text{Cell-transformation ratio}=\frac{T_{Al}(x)}{T_m(x)}. \tag{5.34}$$

This is a measure of the relative biological protection of the two materials.

It has been shown that the cell-transformation ratio does not correlate well with dose equivalent[44] (also see figure 44 herein). The reductions in absorbed dose and dose equivalent are highly inaccurate to assess shield performance for biological protection of long-term exposure by galactic heavy ions. These conventional practices in radiation protection are considered adequate for the relatively low LET radiations[14]. To assess shield performance by GCR exposure, the biological risk is separated into a

Reproduced with permission of the copyright owner. Further reproduction prohibited without permission.

biology-dependent factor and a factor based on the physical properties of the radiation fields. This separation[44] is accomplished using basic concepts in microdosimetry[14]. The physical risk factors are the moments of the LET distribution and are determined by the material properties alone[44]. The effects of the material properties on the moments are evaluated as a measure of shield performance. The biological factors must be investigated by radiobiologists. A new quantity which correlates well with the cell transformation ratio behind various shield thicknesses and materials will be defined below by using the postulate of Bond, Varma, and Sondhaus[67]. They postulate[67] that the outcome of a specific event of size ε is represented by the hit size effectiveness function, $P(\varepsilon)$. The risk function for occurrence within a cell population for radiation with an LET value, L, is

$$R_L = \frac{N_H}{N_E}\int P(\varepsilon) f_L(\varepsilon)\,d\varepsilon = 6.24\sigma_g \frac{D_L}{L}\int P(\varepsilon) f_L(\varepsilon)\,d\varepsilon \qquad (5.35)$$

where $f_L(\varepsilon)$ is a corresponding hit size distribution. Equation (5.35) provides a clear separation of the properties. $P(\varepsilon)$ incorporates the physiochemical processes used to achieve the end point[67] for cell applications, and it includes factors related to induction and promotion of the tissue system to the final observed end point[67]. The factor $f_L(\varepsilon)$ is a physical quantity related to LET and the geometry of the cell[67]. The factor $P(\varepsilon)$ must be extracted from experimental response data for a sufficiently large dynamic range of $f_L(\varepsilon)$ spectra[44]. $P(\varepsilon)$ is expanded as a power series of terms with coefficients adaptable to experimental response data[67],

$$P(\varepsilon) = \Sigma\, b_i \varepsilon^i \qquad (5.36)$$

for which $b_0 = 0$ because P(0)=0. Then, equation (5.35) is approximated as[44]

$$R_L = 6.24\sigma_g \frac{D_L}{L}\sum b_i \langle \varepsilon^i \rangle\ . \qquad (5.37)$$

Reproduced with permission of the copyright owner. Further reproduction prohibited without permission.

By assuming that the response in the limit of low LET is matched to that of γ-ray exposure, which is given in equation (5.2), then[44]

$$k_\gamma = 6.24\frac{\sigma_g}{L_\gamma} b_1 \langle \varepsilon^1 \rangle . \qquad (5.38)$$

Since the average lineal energy (lineal energy is the event size ε_i divided by cell mean chord) is numerically equal to the LET[70], $<\varepsilon^n>$ is proportional to $<L^n>$, by which equation (5.37) can be simplified. From equation (5.38) and (5.5), the total risk R in a mixed environment is the sum over all LET components as[44]

$$R = 0.16 \int k_\gamma (L + a_2' L^2 + a_3' L^3 + \ldots)\phi_L dL = 0.16 k_\gamma < L > \phi + 0.16 k_\gamma \sum_{i=2}^{n} a_i' < L^i > \phi \qquad (5.39)$$

where ϕ is the total fluence. Within this microdosimetric model, the biological risk is related to physical aspect, which is the LET moments, and the clarification of the biological response would correspond to new values of a'_i. The five lowest moments of LET are shown in table 11. The zeroth-order moment (i=0) is the total particle flux in 1 year. The first-order moment is the locally absorbed dose in a water sample and always equals to $<L>\phi$. The second-order moment is nearly proportional to dose equivalent[44]. The ratio of the second moment to the first moment is approximately related to the average quality factor Q. On the basis of conventional dosimetry, Q would be $1+a'_2<L^2> / <L>$ for the conventional radiation (e.g., relatively low LET radiation) and would leave higher terms undefined. Therefore, the material with the lowest value of $<L^2> / <L>$ would be the best shield by minimizing the dose equivalent. However, the higher order terms are important to assess the shield performance for the GCR environment[44]. A correlation of cell transformation was found in terms of the square of the ratio of the fourth moment to the second moment[44]

Reproduced with permission of the copyright owner. Further reproduction prohibited without permission.

$$p_m(x) = \left[\frac{<L^4>}{<L^2>}\right]^2 . \qquad (5.40)$$

The relative performance index, $P_m(x)$ is defined as

$$P_m(x) = \frac{p_{Al}(x)}{p_m(x)} . \qquad (5.41)$$

The relative performance index in table 11 indicates closely the biological consequences such as the cell transformation ratio. The higher LET moments show increasingly strong material dependence, especially at the larger thicknesses[47]. The material dependence of cell transformation is more characteristic of the higher than the lower LET moments. It suggests that dose and dose equivalent, which require only up to the second order term, are poor indicators of biological risk for the GCR environment[44]. Therefore, a material with the lowest value of equation (5.40) would minimize the cell transformation, and it would be judged the best shield for the GCR environment. For deep-space missions with very high LET radiations, the a'_i terms for $i > 2$ in equation (5.39) must be determined for the end points by biological experiments with very high LET radiations.

The relative performance index correlates well with the cell-transformation ratio[44]. Thus a material with the relative performance index of 2 for a given areal density would provide approximately twice as much biological protection as an aluminum shield without increasing the shield mass. The cell-transformation ratio is shown in figures 45 and 46 as a function of areal density for different shields relative to the aluminum standard. The comparison of cell-transformation ratios for liquid hydrogen, lithium hydride, and lead is shown in figure 46. In this figure, the cell-transformation ratio for liquid hydrogen shows a linear relationship to its areal density, x, with a best fit of

$$T_{Al}(x)/T_{H_2}(x) = 1 + 0.383976x . \qquad (5.42)$$

Reproduced with permission of the copyright owner. Further reproduction prohibited without permission.

For lithium hydride, the ratio has an exponential relationship to x with a best fit of

$$T_{Al}(x)/T_{LiH}(x) = \exp(0.07176x - 0.0014999x^2) \tag{5.43}$$

and for lead, the best fit is

$$T_{Al}(x)/T_{Pb}(x) = \exp(-0.08366x + 0.001965x^2)\,. \tag{5.44}$$

Liquid hydrogen shows great promise as a high performance shield material with increasing shield depth, x. The cell transformation ratio can provide the relative performance index for all shield materials because of the excellent linearity between the cell-transformation ratio and relative performance index for GCR environment.

Reproduced with permission of the copyright owner. Further reproduction prohibited without permission.

Table 11. Moments of LET in units of $(\mathrm{MeV/cm})^i$ cm^{-2} behind various shield materials for a year exposure of GCR at solar minimum and their correlated quantities

Shield material	Shield thickness	$i = 0$, 10^8	$i = 1$, 10^9	$i = 2$, 10^{12}	$i = 3$, 10^{16}	$i = 4$, 10^{19}	$p_m(x)$, 10^{15}	$P_m(x)$
free space		1.29	1	1.7	3.7	118		
Al	2 g/cm^2	1.32	.916	.47	.278	4.84	10.6	1
	5 g/cm^2	1.35	.897	.365	.201	3.42	8.78	1
	10 g/cm^2	1.38	.866	.253	.124	2.05	6.57	1
Fe	2 g/cm^2	1.34	.938	.493	.303	5.41	12	.88
	5 g/cm^2	1.35	.942	.407	.235	4.14	10.4	.85
	10 g/cm^2	1.38	.923	.302	.158	2.72	8.11	.81
Poly-ethylene	2 g/cm^2	1.31	.849	.4	.22	3.65	8.33	1.27
	5 g/cm^2	1.33	.787	.261	.128	2.03	6.05	1.45
	10 g/cm^2	1.34	.716	.143	.0586	.864	3.65	1.80

Reproduced with permission of the copyright owner. Further reproduction prohibited without permission.

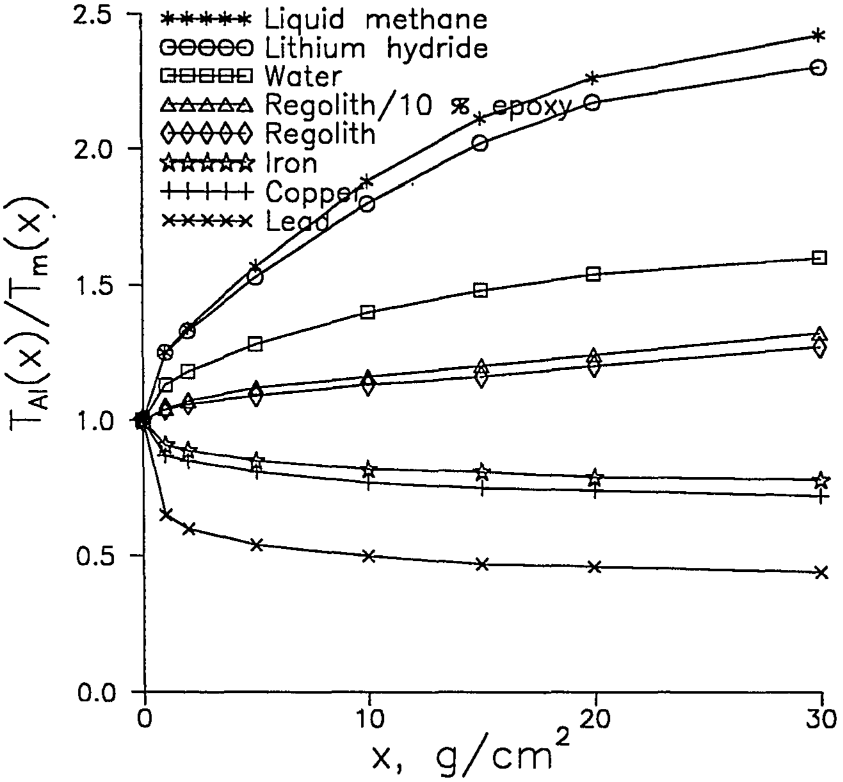

Figure 45. The cell-transformation ratio as a function of areal density relative to the aluminum standard

Reproduced with permission of the copyright owner. Further reproduction prohibited without permission.

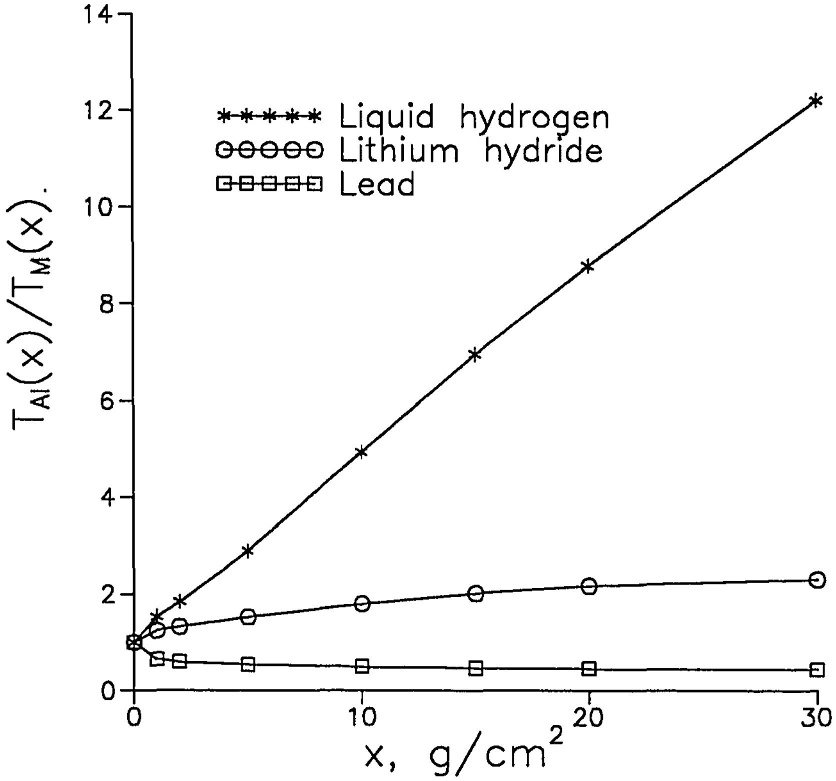

Figure 46. The cell-transformation ratio as a function of areal density relative to the aluminum standard

Reproduced with permission of the copyright owner. Further reproduction prohibited without permission.

5.3.3 Nuclear Attenuation and Shield Performance

The analysis of shield performance in section 5.3.2 above was cast in terms of the microscopic fluctuations of energy deposition in the exposed biological systems. The range of such fluctuations are determined by the particle type and energy as shown in figures 31 to 34. It is difficult to relate any particular LET interval with any particular specie of the radiation field or to the specific nuclear processes by which the field composition is altered.

The nuclear data are represented by two parameters as they affect the radiation field. The first is the mean free paths of individual species to a nuclear reaction site and the second is the array of secondary products of the reactions. The nuclear mean free paths are among the best known nuclear parameters for a limited number of projectile-target combinations and beam energies. Theoretical estimates calculated from the elastic channel amplitudes can be made without a detailed knowledge of the nuclear excitation spectra since the results are little affected by coupling to inelastic processes[79]. Confidence in the calculations is achieved by the fact that the calculated values agree well with the limited number of experimental nuclear absorption cross sections which have been measured[80].

Reproduced with permission of the copyright owner. Further reproduction prohibited without permission.

On the other hand, the nuclear breakup depends on the details of both the discrete and continuous nuclear excitation spectra and except for very light nuclei theoretical calculations are not possible. Fortunately, the charge distribution of any particular fragment mass is dominated by the nuclear binding and not so much by the means through which the fragments are produced. Such charge distributions for proton-induced reactions have been studied extensively by Rudstam[40]. The mass removal cross section could be estimated by a semiempirical liquid drop model in which the surface energy has an empirical correction for highly misshapen nuclei[30]. This semiempirical correction is adjusted to fit the available experimental data though there is a paucity of this data. Therefore the validity of this model is still in question.

In viewing the theoretical calculation of the nuclear mean free paths[47], it is clear that the hydrogen shield presents the greatest cross section per unit mass. In addition, the lighter mass shields are more effective than those of heavier mass in reacting with the heavier ions. However, the fragment distributions produced also affect the results[54].

The effects of the fragment distributions can be studied by looking at the physical limits of the fragmentation event. These limits are an extreme peripheral collision in which a single nucleon is removed per collision and an exact central collision in which the nucleus is completely dissociated into nucleonic components. For a nominal collision, the nuclear fragmentation parameters are generated using the nuclear database (NUCFRG[30, 41] model) in section 2.2.2. The effects of these collision types on several shield materials are

Reproduced with permission of the copyright owner. Further reproduction prohibited without permission.

shown in figures 47 to 50. Because of these limits, there are great effects of the uncertainty in the nuclear fragmentation events on the transformation rates of the C3H10T1/2 cell system. This uncertainty is undoubtedly due to the dependence of the transformation rates on the higher moments of the LET distribution which are sensitive to the distribution of fragments produced in the nuclear events[44]. Although the LET distribution is closely related to the energy fluctuation in specific target sites within the tissue system, there is no direct relation of LET to particle type and it is difficult to relate the LET distribution to the fragmentation process.

An alternate means of representing the biological response data is to use contributions of biological change from each charge group of the environment as shown in figures 51 to 54. It is clear from these figures that the efficiency of the liquid hydrogen shield comes from its ability to rapidly attenuate the HZE components. For example, interactions by the iron flux in free space account for nearly 30 percent of the cell transformations. This is reduced by several orders of magnitude behind a 30 g/cm^2 liquid hydrogen shield compared with a reduction of only a factor of three behind an equivalent mass of lead shielding. In liquid hydrogen, all components are attenuated to some degree while in the lead shield the number of light ions tend to increase as the heavier ions slowly attenuate. In addition, the number of neutrons, protons, and helium ions are greatly increased over their free space values behind a lead shield, in part, due to secondary production from the target nuclei. These charge distributions are intimately related to the reduction of the high LET moments and are closely related to the shield parameters

Reproduced with permission of the copyright owner. Further reproduction prohibited without permission.

studied in laboratory experiments with HZE beams. Clearly, hydrogen-containing materials will play an important role in shielding during long-term space exposure.

Reproduced with permission of the copyright owner. Further reproduction prohibited without permission.

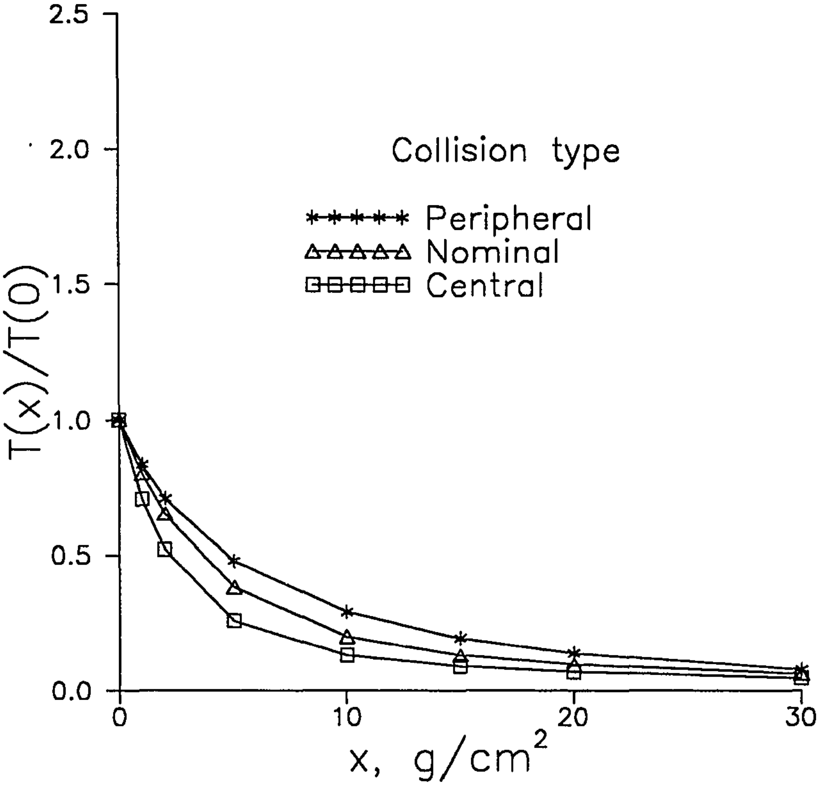

Figure 47. The effects of physical limits on liquid hydrogen

Reproduced with permission of the copyright owner. Further reproduction prohibited without permission.

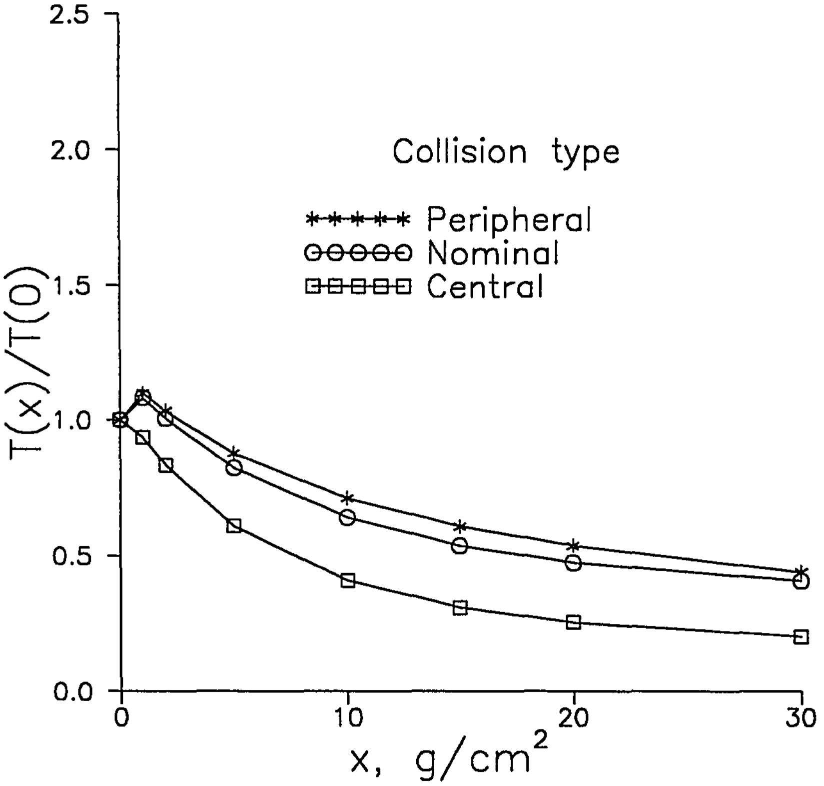

Figure 48. The effects of physical limits on water

Reproduced with permission of the copyright owner. Further reproduction prohibited without permission.

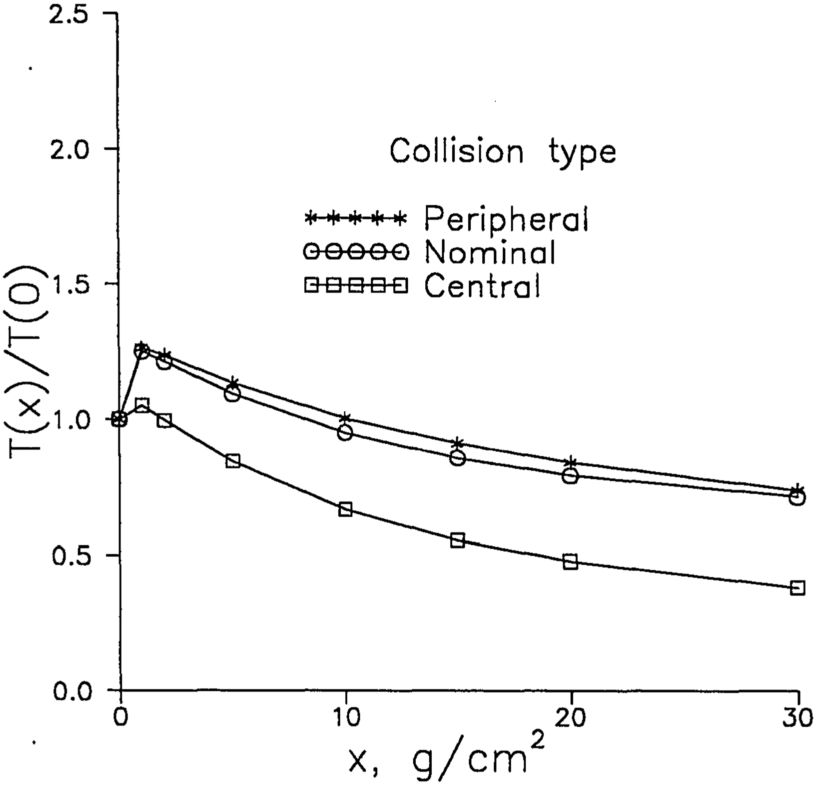

Figure 49. The effects of physical limits on aluminum

Reproduced with permission of the copyright owner. Further reproduction prohibited without permission.

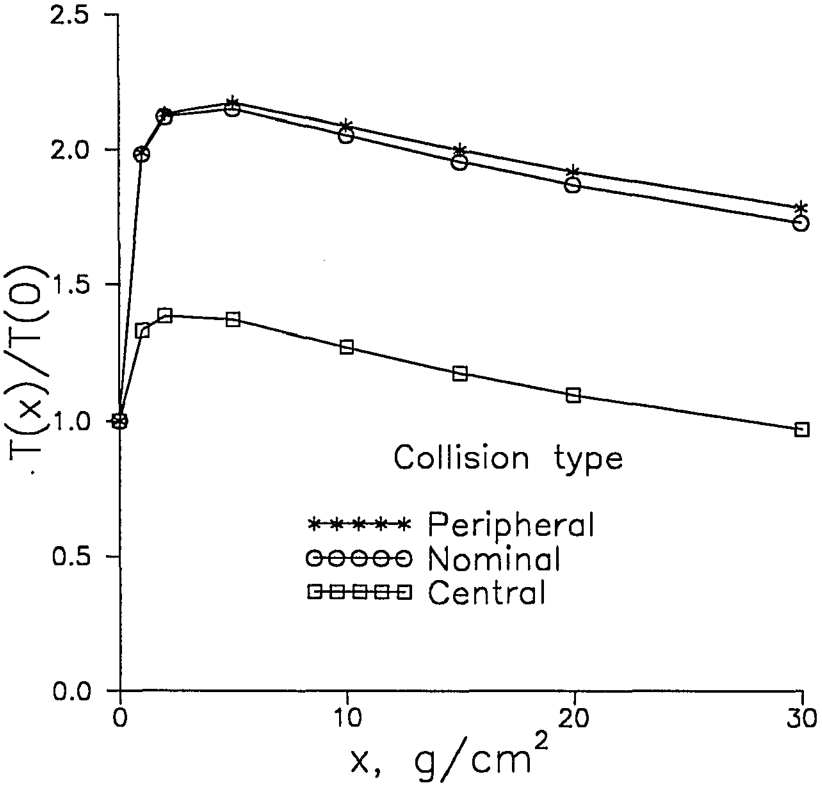

Figure 50. The effects of physical limits on lead

Reproduced with permission of the copyright owner. Further reproduction prohibited without permission.

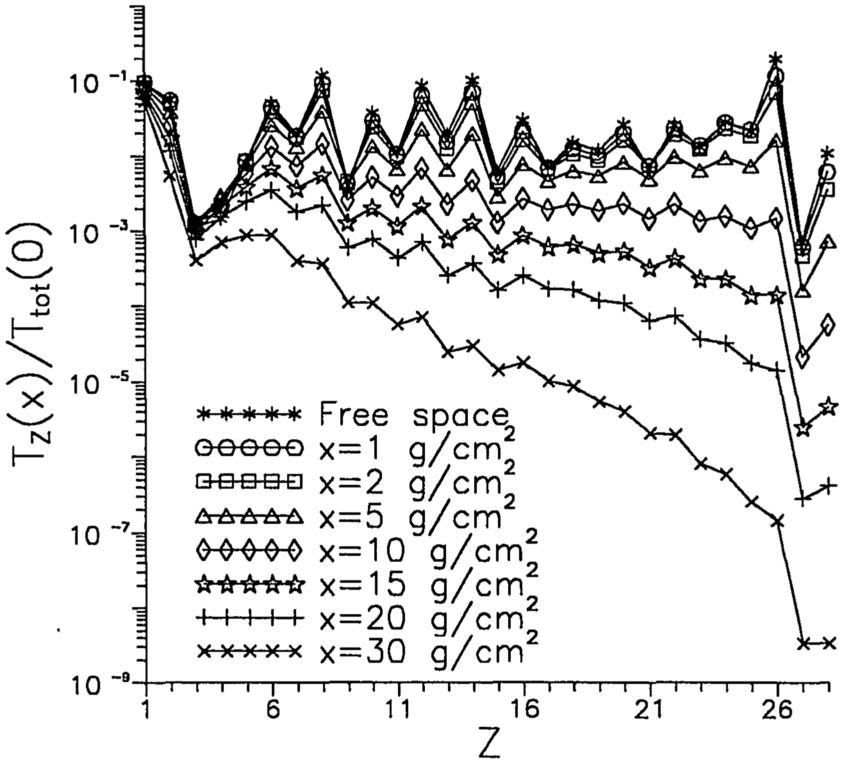

Figure 51. The contributions of biological change from each charge group of the environment (Liquid hydrogen)

Reproduced with permission of the copyright owner. Further reproduction prohibited without permission.

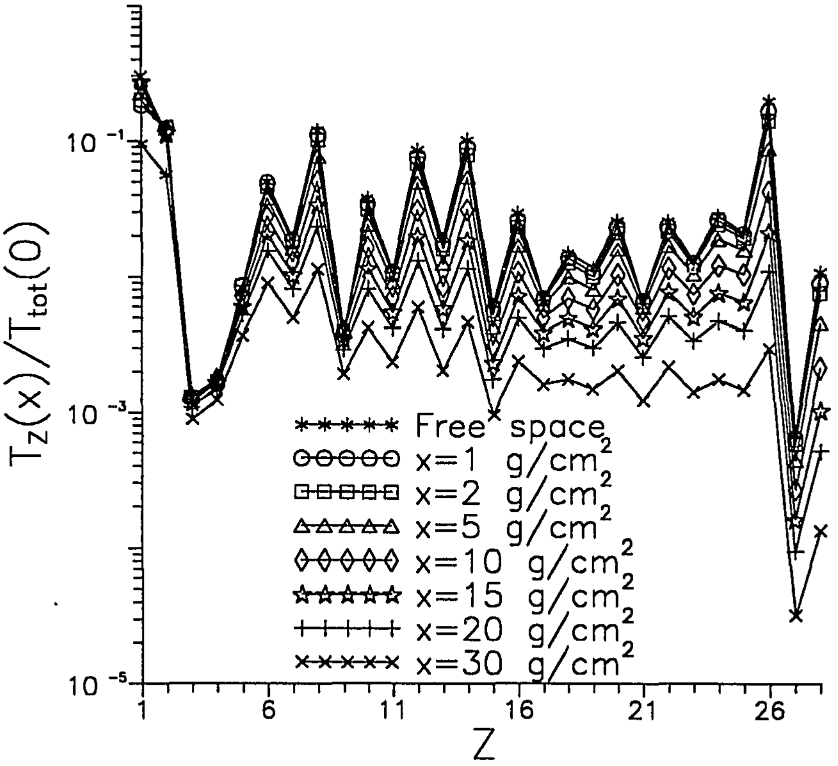

Figure 52. The contributions of biological change from each charge group of the environment (Water)

Reproduced with permission of the copyright owner. Further reproduction prohibited without permission.

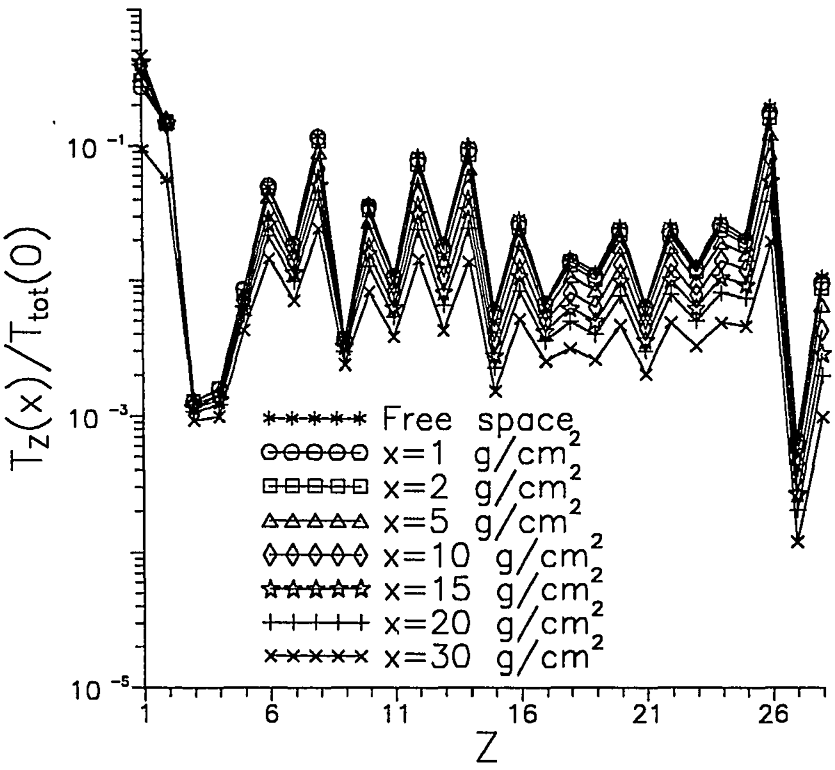

Figure 53. The contributions of biological change from each charge group of the environment (Aluminum)

Reproduced with permission of the copyright owner. Further reproduction prohibited without permission.

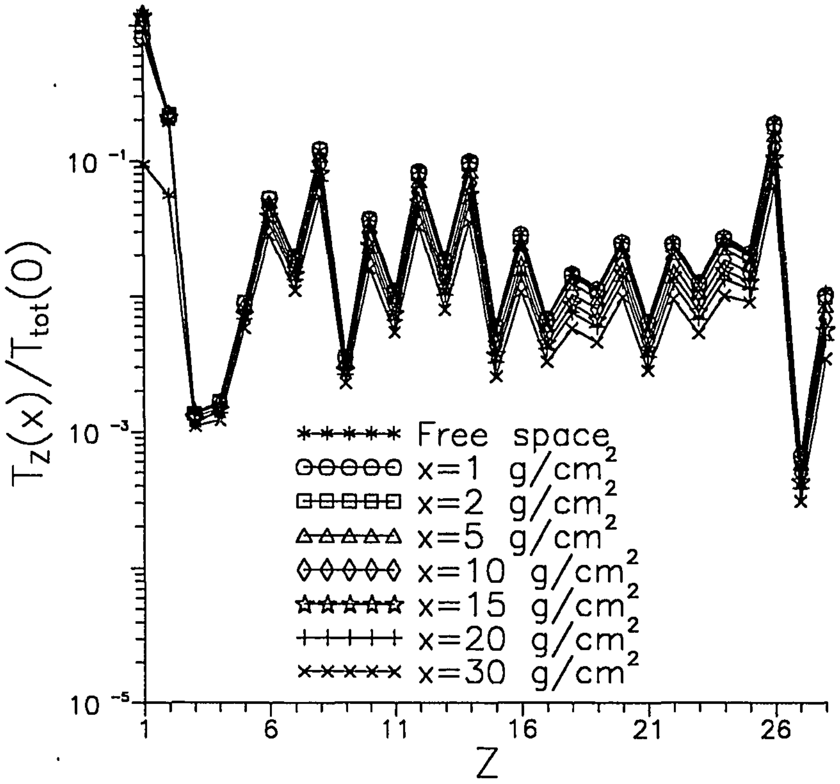

Figure 54. The contributions of biological change from each charge group of the environment (Lead)

Reproduced with permission of the copyright owner. Further reproduction prohibited without permission.

5.4 Results and Discussion

By choosing appropriate compositions for structural materials, the exposure risk for humans from space radiations can be reduced. Based on the shield material characteristics discussed above in section 5.3, polymeric materials and lunar regolith were evaluated for the prediction of the biological effects of a one-year exposure to GCR at the 1977 solar minimum. Six polymeric materials were evaluated ranging from polyethylene, the polymer with the highest hydrogen content, to polytetrafluoroethylene with no hydrogen. As expected from earlier calculations[47] for liquid hydrogen, polyethylene is the most efficient of the materials studied in removing the high LET components from GCR without adding greatly to the low LET radiation fields. Figures 55 and 56 illustrate that to shield against biological effects, polyethylene is the most effective and polytetrafluoroethylene the least.

A lunar-regolith/epoxy mixture is a potential construction material for a habitat during long-term lunar missions. Regolith is able to attenuate the high LET components but also adds to the low LET fields, because it contains significant amount of the elements Si (19.3 mol-%), Al (7.5), Fe (6.1), and Mg (5.5). The results of calculations shown in figures 57 and 58 illustrate that lunar regolith is a less effective shield material for HZE particles than the hydrogen-containing polymers studied. Hydrogen in a polymer such as

Reproduced with permission of the copyright owner. Further reproduction prohibited without permission.

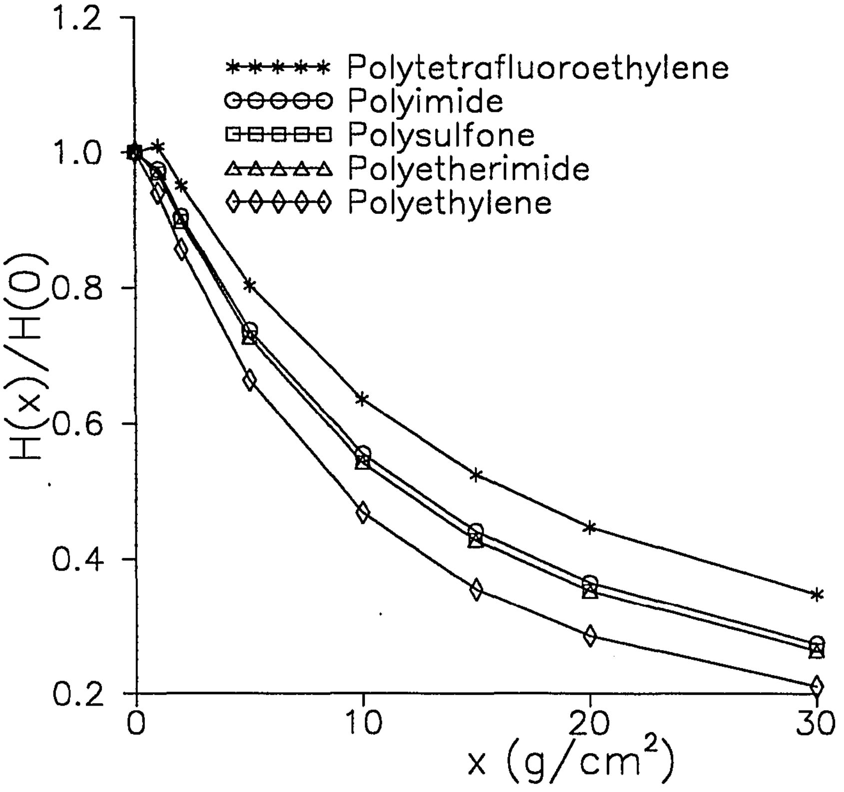

Figure 55. Attenuation of dose equivalent behind polymeric materials as a function of shield thickness

Reproduced with permission of the copyright owner. Further reproduction prohibited without permission.

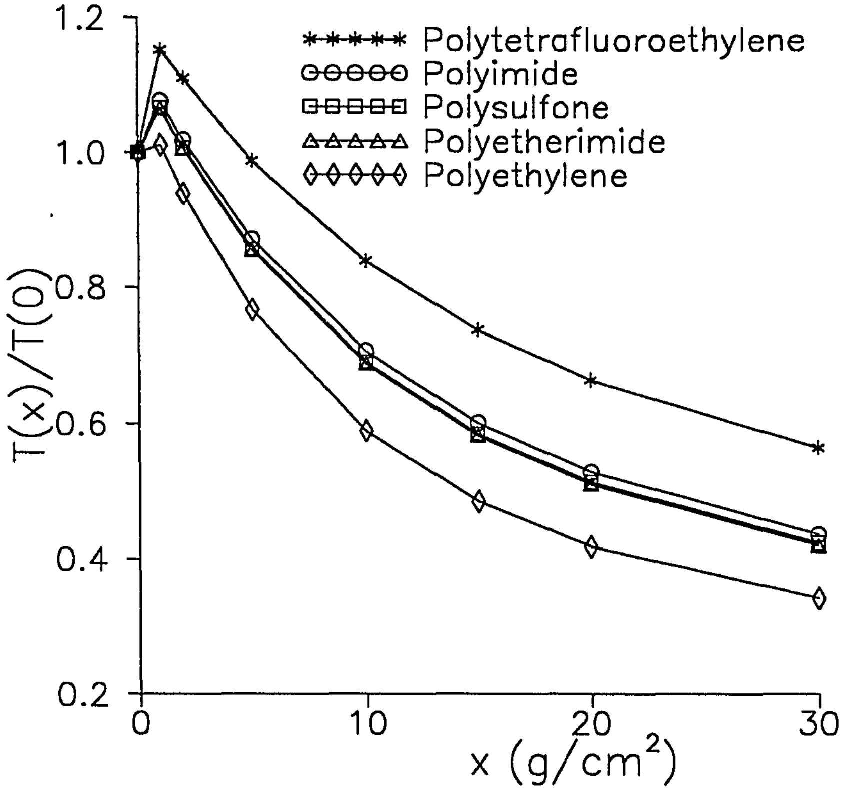

Figure 56. Attenuation of cell transformations behind polymeric materials as a function of shield thickness

Reproduced with permission of the copyright owner. Further reproduction prohibited without permission.

an epoxy improves the shielding capability of regolith as shown in figures 57 and 58. Using an epoxy as a binder, regolith building blocks can be manufactured. This provides structures which are more durable, more versatility in design and utility, and safer in terms of radiation exposure.

Biological effects are reduced efficiently not only by selecting different materials but also by adjusting the thickness of the material. This is shown in figures 55 to 58 where the attenuation of biological effects are measured in terms of dose equivalents (figures 55 and 57) and cell transformations (figures 56 and 58) in a one-year exposure behind various shield materials as a function of shield thickness. The variation in the two measures of biological effects, neoplastic cell transformations and dose equivalents, shows a material's dependence qualitatively. However, there are important quantitative differences in the protective properties of shield materials dependent on the biological model used. Clearly, many shield materials provide only modest reductions in neoplastic transformation ratios as shown in figures 56 and 58; whereas, in figures 55 and 57, the dose equivalent shows much greater reductions for the same shield thickness.

The transmitted annual fluences of particles at various thicknesses are shown in figures 59 to 61 to represent the shield properties for nominal collisions for three potentially important materials for deep space missions: polyethylene, one of the more applicable polymers, aluminum, the usual space construction material, and lunar regolith, the material readily available on the lunar surface. The change in the fluence is shown in

Reproduced with permission of the copyright owner. Further reproduction prohibited without permission.

free space and at shielding thickness of 5, 15, 30 g/cm^2. The uncertainty in the transmitted fluence at 30 g/cm^2 due to the two physical limits is shown in figures 62 to 64 for the three materials. The greatest uncertainties are in the highest LET components where the greatest uncertainty in biological response is expected due to uncertainty in the nuclear cross sections[78]. The effects of the shield material transmission characteristics are shown on dose equivalent in figures 65 to 67 and on cell transformation rate in figures 68 to 70 for the three nuclear collision models. The uncertainty in transmission characteristics of the shield materials would be as large as a factor of two. This modest uncertainty requires excess mass over nominal shielding architectures and must be reduced for efficient space travel.

Using current estimates for nominal collisions has shown that the HZE ions in space pose a significant hazard to biological systems and that the LET distribution above about 10 keV/μm is an important indicator of biological damage. Furthermore, the LET distribution is a function of shield composition, even with materials of the same areal density. Polyethylene, with its short nuclear absorption lengths and higher nuclear attenuation rate, is an efficient shield material for GCR exposure in spite of the large number of heavy projectile fragments produced. The unique role of hydrogenous materials as high-performance shields is clear, even though an accurate evaluation of risk reduction is not possible.

Reproduced with permission of the copyright owner. Further reproduction prohibited without permission.

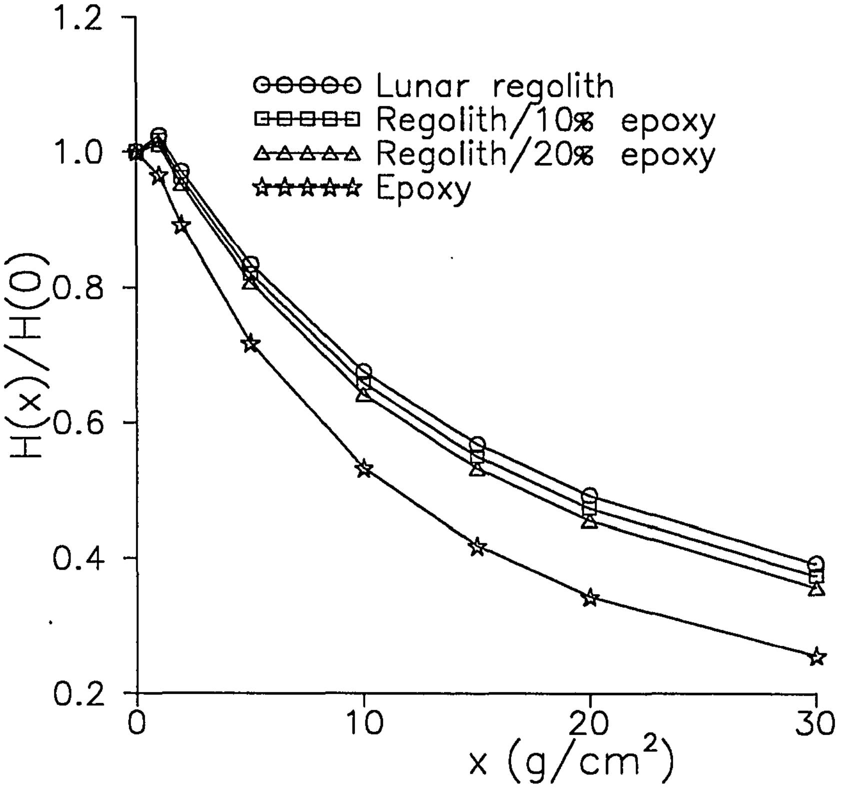

Figure 57. Attenuation of dose equivalent behind lunar construction materials as a function of shield thickness

Reproduced with permission of the copyright owner. Further reproduction prohibited without permission.

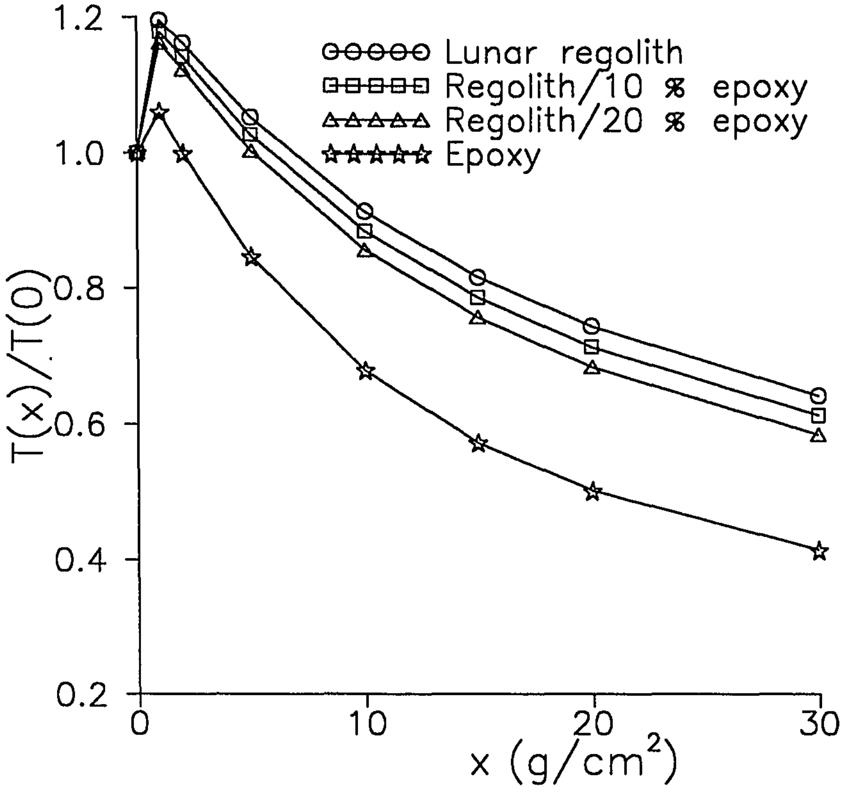

Figure 58. Attenuation of cell transformations behind lunar construction materials as a function of shield thickness

Reproduced with permission of the copyright owner. Further reproduction prohibited without permission.

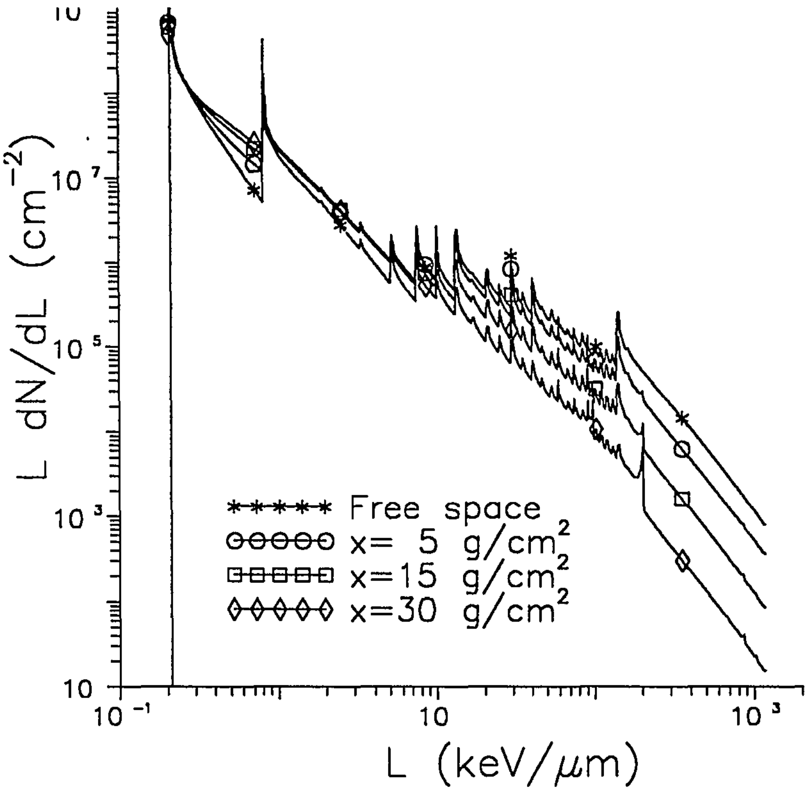

Figure 59. Annual transmitted GCR differential LET spectrum for nominal nuclear cross sections (Polyethylene)

Reproduced with permission of the copyright owner. Further reproduction prohibited without permission.

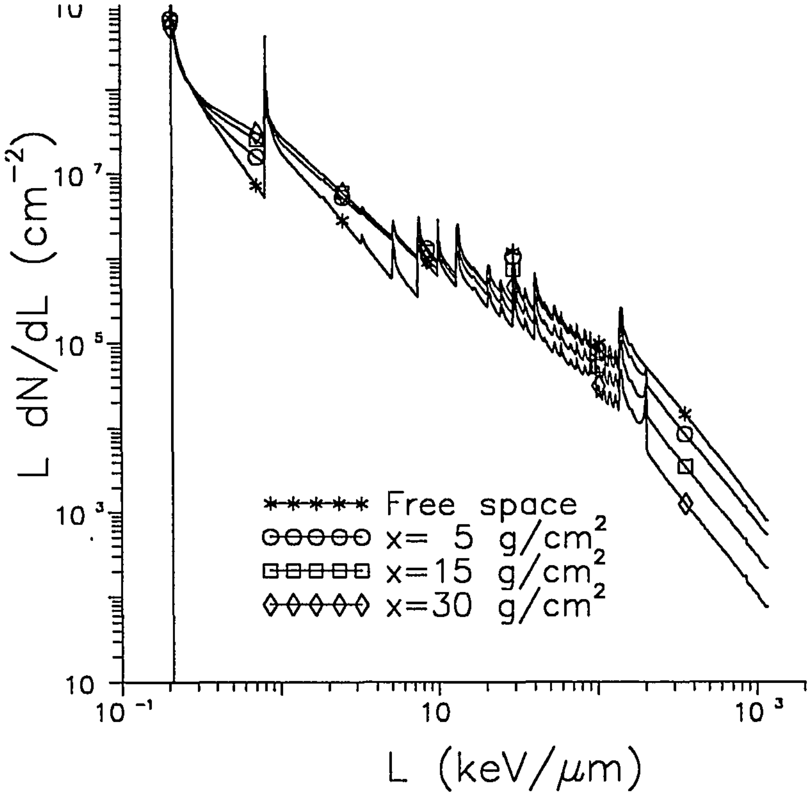

Figure 60. Annual transmitted GCR differential LET spectrum for nominal nuclear cross sections (Aluminum)

Reproduced with permission of the copyright owner. Further reproduction prohibited without permission.

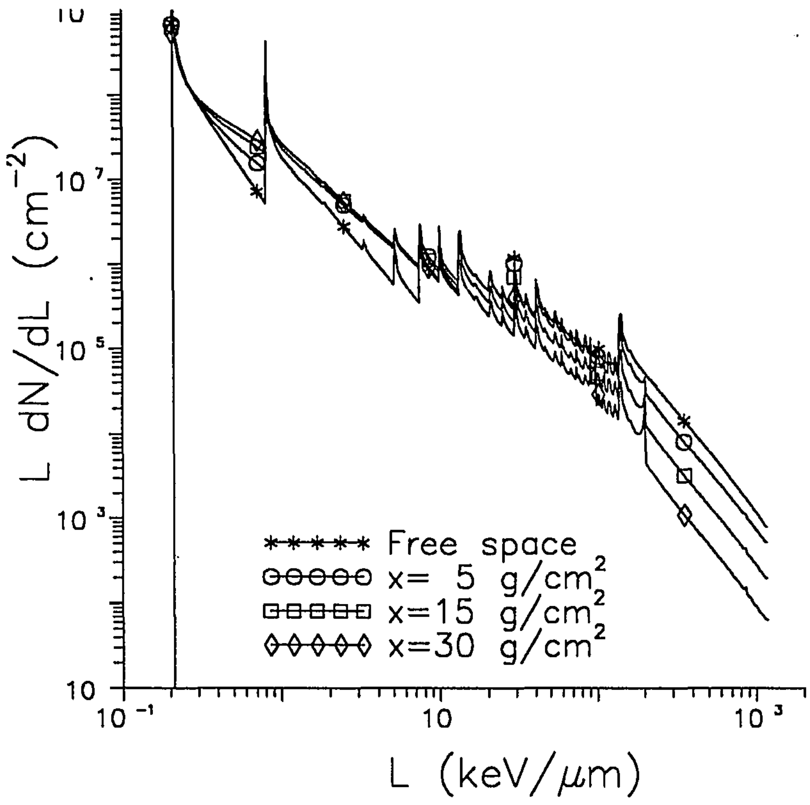

Figure 61. Annual transmitted GCR differential LET spectrum for nominal nuclear cross section (Regolith)

Reproduced with permission of the copyright owner. Further reproduction prohibited without permission.

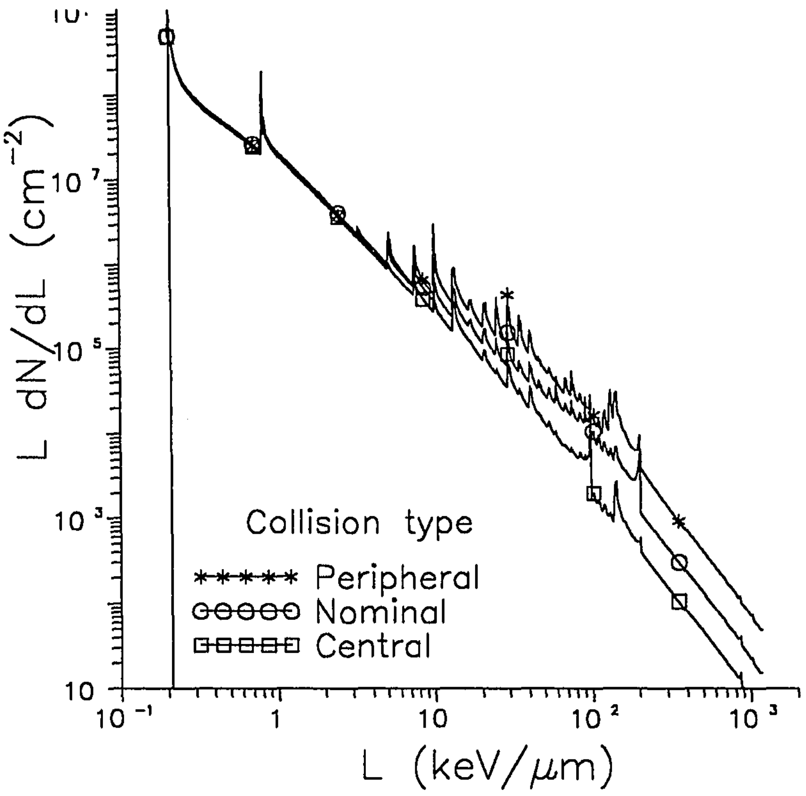

Figure 62. The uncertainty at 30 g/cm^2 for three nuclear models in polyethylene

Reproduced with permission of the copyright owner. Further reproduction prohibited without permission.

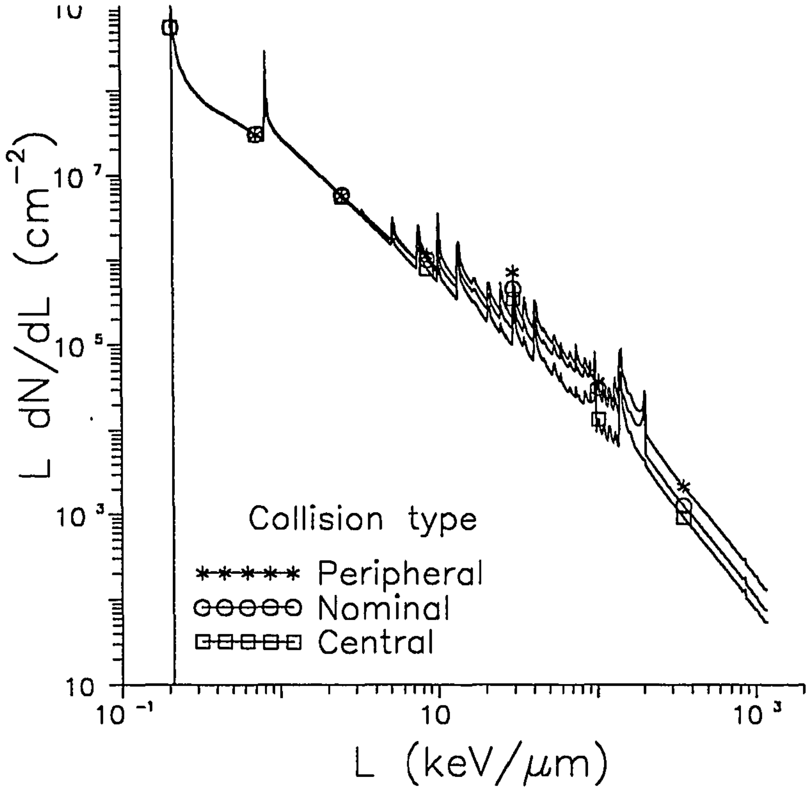

Figure 63. The uncertainty at 30 g/cm^2 for three nuclear models in aluminum

Reproduced with permission of the copyright owner. Further reproduction prohibited without permission.

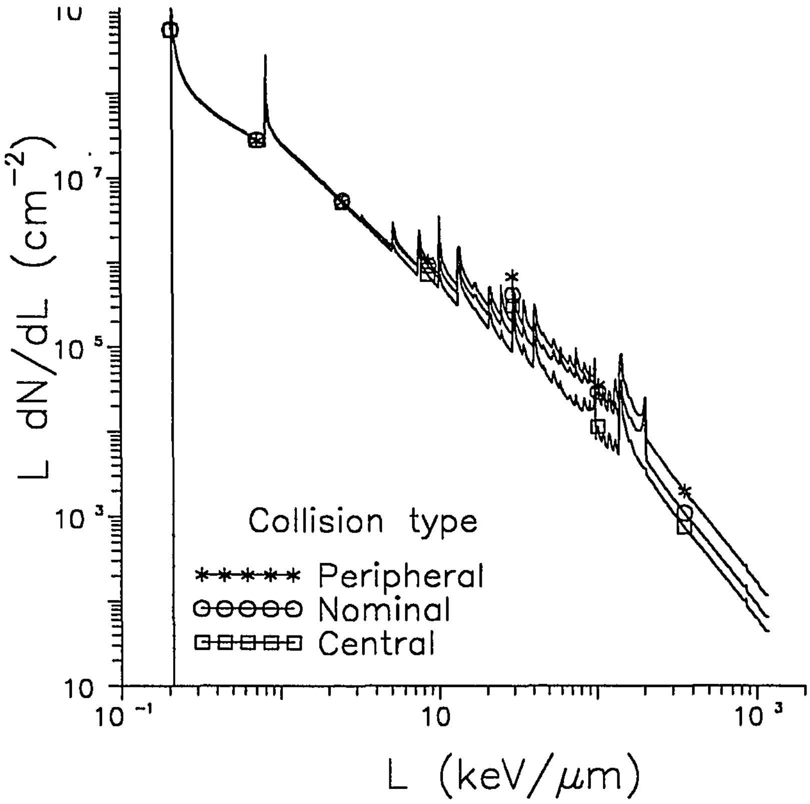

Figure 64. The uncertainty at 30 g/cm^2 for three nuclear models in regolith

Reproduced with permission of the copyright owner. Further reproduction prohibited without permission.

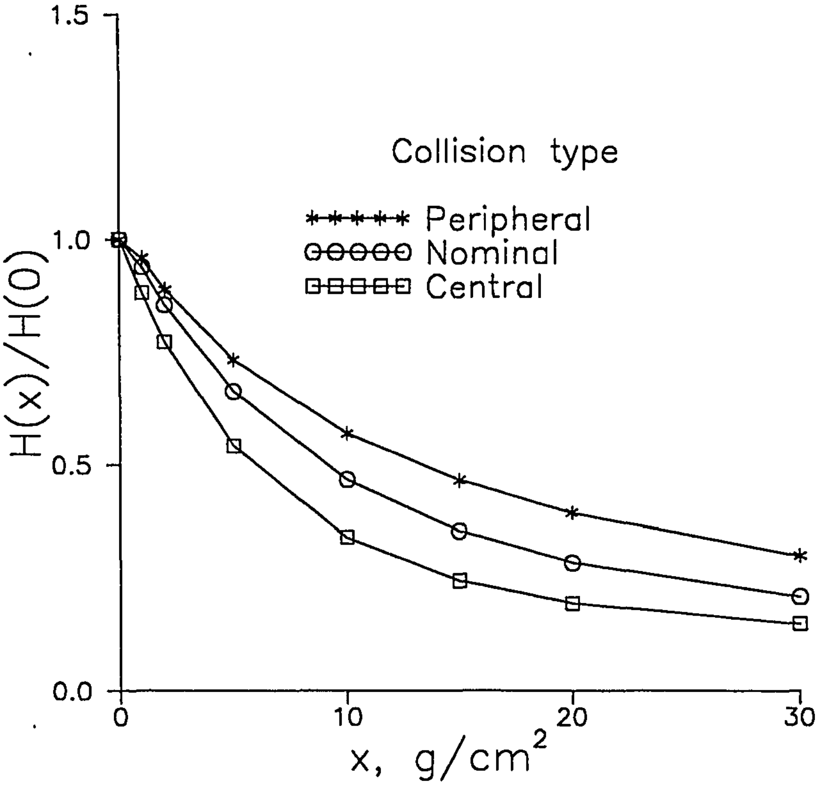

Figure 65. Attenuation characteristics of dose equivalent in polyethylene

Reproduced with permission of the copyright owner. Further reproduction prohibited without permission.

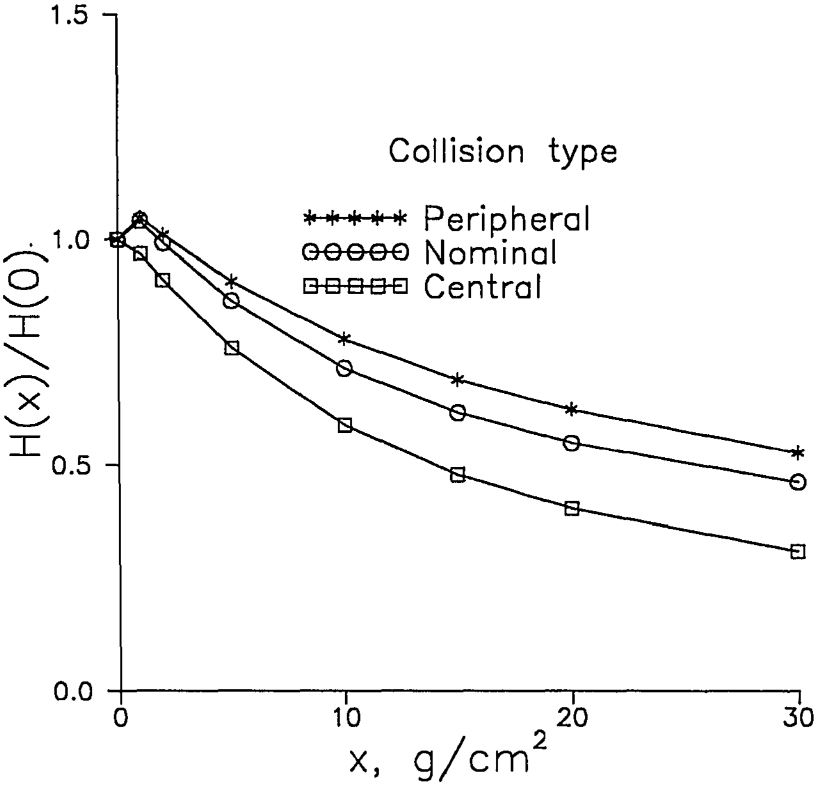

Figure 66. Attenuation characteristics of dose equivalent in aluminum

Reproduced with permission of the copyright owner. Further reproduction prohibited without permission.

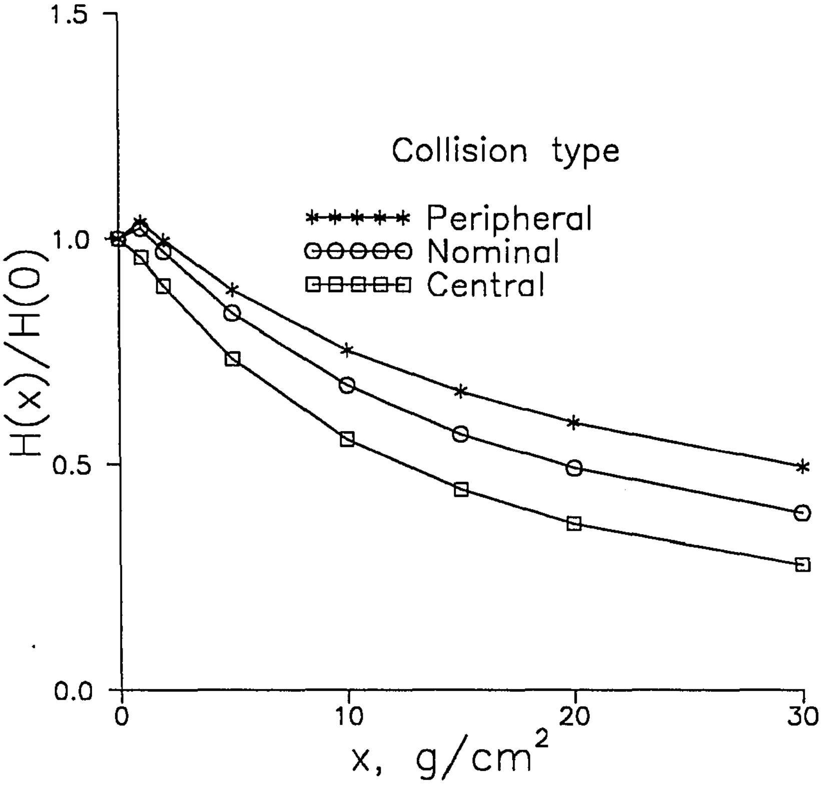

Figure 67. Attenuation characteristics of dose equivalent in regolith

Reproduced with permission of the copyright owner. Further reproduction prohibited without permission.

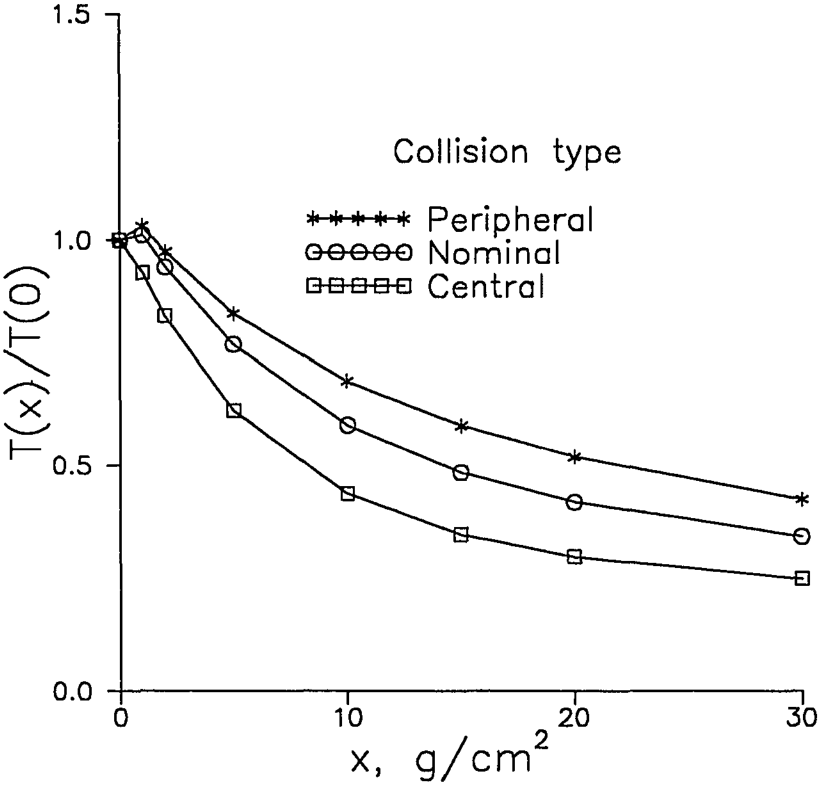

Figure 68. Attenuation characteristics of cell transformation in polyethylene

Reproduced with permission of the copyright owner. Further reproduction prohibited without permission.

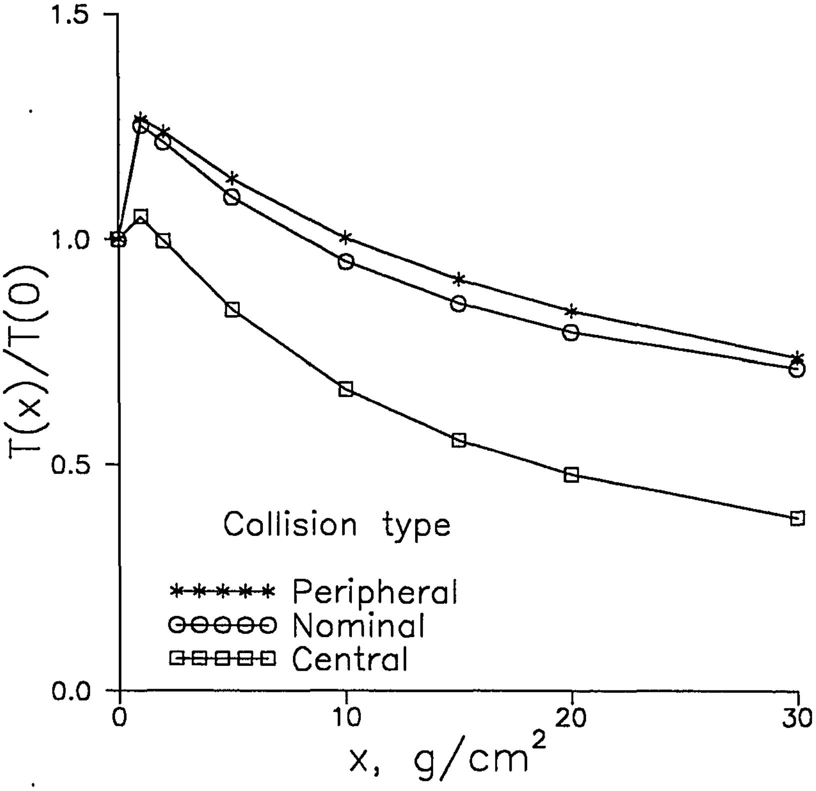

Figure 69. Attenuation characteristics of cell transformation in aluminum

Reproduced with permission of the copyright owner. Further reproduction prohibited without permission.

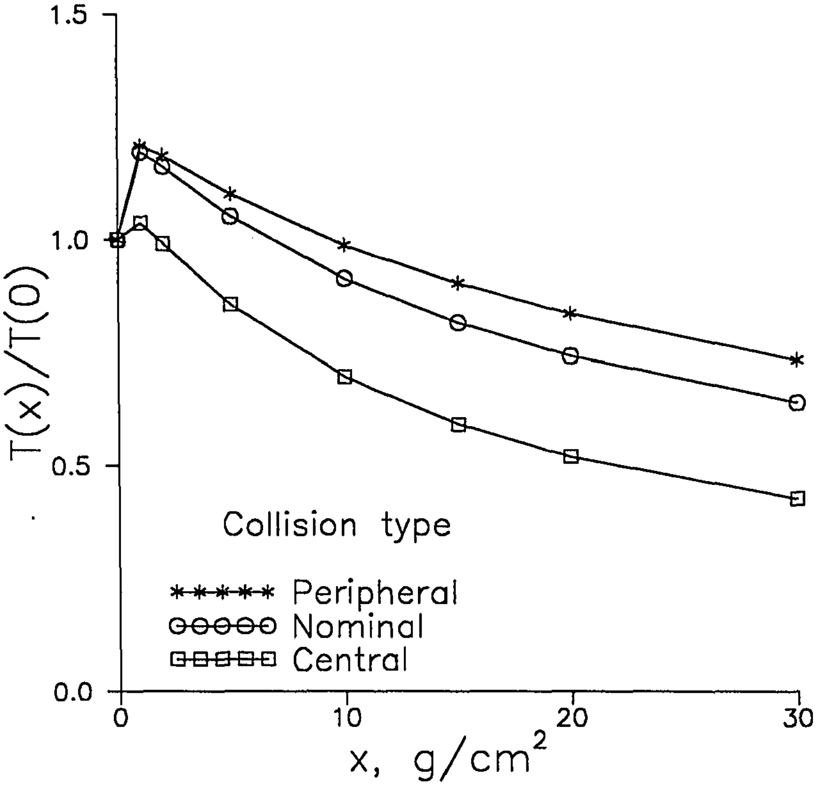

Figure 70. Attenuation characteristics of cell transformation in regolith

Reproduced with permission of the copyright owner. Further reproduction prohibited without permission.

6. Summary and Conclusion

Galactic cosmic radiation impacting on the exterior of a spacecraft can result in an increased number of fragments inside the spacecraft due to the production of secondary radiation through interactions with the spacecraft material. These radiation components present a hazard to humans and microelectronic devices. Selecting an appropriate composition of a structural piece or a container is a recognized means of reducing the radiation hazard to humans and microelectronic devices from space radiation and secondary neutrons on high-altitude airplanes, in low-Earth orbit, or in deep space missions.

Hydrogen-containing polymeric materials may have utility as shielding from GCR, because theoretical calculations[47] show that hydrogen presents the greatest cross section per unit mass. Additionally, hydrogen is particularly effective in reducing the energy of secondary neutrons generated in the shield through elastic collisions thereby making them more susceptible for absorption by other atoms such as boron. Calculations were performed for the propagation and interactions of particles having high atomic numbers and energy through six polymeric materials, both pure and loaded with boron, and with epoxy-bound lunar regolith. The modelings were carried out with the transport codes for laboratory ion beams and the cosmic ray spectrum at the 1977 solar minimum. Shield

Reproduced with permission of the copyright owner. Further reproduction prohibited without permission.

effectiveness was measured from the back side of the shield in several ways: as the fluence of projectiles and their fragments from laboratory ion beams, as the SEU response of microelectronic devices from the GCR, and as the biological response of living tissue from the GCR.

Energetic primary particles undergo nuclear reactions before stopping in a shield medium. The secondary radiation resulting from these reactions yields lighter particles with a broad distribution of energies. The flux of each radiation with a broad energy distribution behind a shield material was integrated numerically to compute the total ion fluence for laboratory ion beams. This quantity was then compared for different materials. For energetic ion beams, polyethylene with its high hydrogen density is the most effective absorber for thick shields, while polytetrafluoroethylene with the heavier fluorine atoms appears to be more effective for thin shields due to lower production of secondary radiation. The inclusion of boron in a polymeric material only slightly diminishes the capacity of the material to absorb HZE particles but dramatically increases its ability to absorb low energy neutrons. Lunar regolith is a less effective shield material for HZE particles than the hydrogen-containing polymers studied. Adding an epoxy to bind lunar regolith in a mixture enhances its shielding properties from HZE particles because of the hydrogen contained in the epoxy. Therefore, a material with a high percentage of lighter atoms such as hydrogen would be effective for thick shields while a material composed of heavier atoms might yet prove to be more effective in thin shields for energetic ion beams

Reproduced with permission of the copyright owner. Further reproduction prohibited without permission.

with respect to the number of secondary particles and without considering their radiation quality.

The fragmentation during nuclear reactions by and of an iron ion produces hundreds of isotopes. These isotopes are represented in the solution of the transport problem. A reduced set of isotopes was selected to minimize the computational burden but errors in the final result were introduced. A determination of the smallest isotope table to produce an adequate laboratory beam simulation was required. Improvements in the treatment of the nuclear database were obtained by a determination of an optimal isotope table that gives both computational precision and practical computation time. The effects on isotope list selection were studied on the mass and charge distributions for an iron beam in an epoxy. Charge distribution converges within 3.1 percent of the fluence spectra for a table of 80 isotopes compared to that of the largest table of 125 isotopes. The convergence is within 2.7 percent for a table of 100 isotopes. Mass distribution converges within 5 percent of the fluence spectra for a table of 122 isotopes. Iron is the most abundant massive ion in space and the fragmentation event is dominated by the nuclear structure of the projectiles, so these results are generally applicable to other materials and ions important to the space radiation problem.

Interaction data were combined in the Boltzmann equation with the 1977 solar minimum cosmic ray spectrum[59] to evaluate the transmitted environment through various shields. To predict the SEU error rate on SRAM, the resultant LET spectra through

Reproduced with permission of the copyright owner. Further reproduction prohibited without permission.

various materials using the HZETRN code[18] were coupled with a measured SEU cross section versus LET curve. High-LET ions are very instrumental in causing an SEU, so high-LET degraders are necessary for reducing SEU rates. The SEU error rate on SRAM is a rapidly decreasing function of shield thickness. Materials as diverse as liquid hydrogen (Z=1), aluminum (Z=13), iron (Z=26), copper (Z=29), and lead (Z=82), have been surveyed as shields against SEUs on SRAM. In addition, hydrogenous materials such as polyethylene, and lithium hydride were also surveyed. A liquid hydrogen shield is an ideal selection for attenuating all radiation components if structural considerations are ignored. The galactic cosmic high-LET ions were attenuated better in hydrogenous material such as polyethylene, which was a more effective high-LET degrader than metals. The result indicates that polyethylene provides good shielding efficiency against SEU.

The transmitted environment through various shields was used for further evaluation of biological effects. The shield effectiveness is intimately related to the nature of the nuclear cross sections through the change in the microscopic fluctuations in biological exposure. The shield effectiveness was examined in terms of two biological models. The first model is the conventional risk assessment method using the quality factor as a function of LET[62]. The second model is a track structure repair kinetic model[64] for the mouse cell C3H10T1/2.

The dose equivalent $H(x)$, which is obtained by multiplying the absorbed dose at each LET by the corresponding quality factor[62], is a measure of the response of living

Reproduced with permission of the copyright owner. Further reproduction prohibited without permission.

tissue to radiation. The quality factor was used to estimate the dose equivalent because all cells do not absorb energy equally from each LET component. Among the materials studied, polyethylene provides the most effective shielding at all thicknesses in terms of the relative attenuation of dose equivalent, $H(x)/H(0)$. Polyethylene is more effective than polytetrafluoroethylene even for very thin films because of its greater efficiency in attenuating the heavier ions that are the most destructive to living tissue. This result shows that polyethylene, with its short nuclear absorption length and the higher nuclear attenuation rate, is an efficient shield material for GCR exposure in spite of the large number of heavy projectile fragments produced. The calculations show lunar regolith to be a less effective shield material for GCR exposure than the hydrogen-containing polymers studied.

The second study of the response of living cells to the effects of GCR is represented in terms of occurrences of neoplastic cell transformations, $T(x)$, resulting from a one-year exposure behind a shield of thickness x relative to occurrences, $T(0)$, in free space. Unlike conventional dosimetric analysis, wherein radiation quality is represented by LET-dependent quality factors,.the repair kinetics model is driven by track-structure dependent injury coefficients[64] from experimental data with various ions. The variation in the calculated cell transformation ratio, $T(x)/T(0)$, shows that the dependence on material is qualitatively similar to that found for $H(x)/H(0)$. However, there are important quantitative differences in the protective properties of shield materials dependent on the biological model used. Clearly, many shield materials provide only modest reductions in

Reproduced with permission of the copyright owner. Further reproduction prohibited without permission.

neoplastic transformation ratios; whereas, they show a much greater reduction in dose equivalent for the same shield thickness. Complete shield optimization must await an improved understanding of biological response.

Radiation risks depend on the microscopic fluctuations of energy absorption events in specific tissues[77]. Materials with atoms of low atomic number (e.g., liquid hydrogen) attenuate a very broad range of LET components[47] even though there is a gain in many low LET components as shield thickness increases. However, the effects from these low LET components on cells are primarily indirect damage in cellular DNA brought about by OH radicals and are of negligible significance[81]. Materials with atoms of higher atomic number (e. g., lead) attenuate only the highest LET components[47] at the expense of producing a broad range of LET components for which biological response may be enhanced relative to free space exposures. These results[47] also occur for aluminum with thicknesses of 2 to 10 g/cm^2 which are typical for the space program. The effects of nuclear model uncertainty is more important in the case of cell transformation because there are important quantitative differences in the predicted biological effects between the two biological models. Uncertainties in the nuclear database exist for the calculation of the radiation field modified by different polymeric materials. The biological uncertainty is associated with the track structure of the energetic ions. The greatest uncertainty in biological response is expected from high-LET components[61]. However, a relatively appropriate shield material optimization is achieved by the estimation of shield effectiveness using the cell transformation ratio relative to free space in order to provide

Reproduced with permission of the copyright owner. Further reproduction prohibited without permission.

protection against exposure of diverse radiation types, which is typical of GCR exposure. The unique role of hydrogenous materials, such as polymers, as high-performance shields is clear, even though an accurate evaluation of risk reduction is not possible because of the current uncertainty.

Reproduced with permission of the copyright owner. Further reproduction prohibited without permission.

LITERATURE CITED

1. Haffner, J. W.: Radiation and Shielding in Space, Nuclear Science and Technology. Series 4, Academic Press, 1967, pp. 1- 347.

2. Ginzburg, V. L.: The Origin of Cosmic Radiation. Progr. Elem. Particle Cosmic Ray Phys. 4, 1958, p. 339.

3. Colgate, S. A.; Grasberger, W. H.; and White, R. H.: The dynamics of a Supernova Explosion. J. Phys. Soc. Japan, 17, Suppl. A-III, 1963, p. 157.

4. Meyer, P.: Cosmic Rays in the Galaxy. Ann. Rev. Astron. Astrophys., 7, 1969, p. 1.

5. Wilson, J. W.: Environmental Geophysics and SPS Shielding. Workshop on the Radiation Environment of the Satellite Power Systems, Walter Schimmerling and Stanley B. Curtis, eds., LBL-8581, UC-41 (Contract W-7405-ENG-48), Univ. of California, 1978, pp. 33-116.

Reproduced with permission of the copyright owner. Further reproduction prohibited without permission.

6. Wilson, J. W.; Townsend, L. W.; Schimmerling, W.; Khandelwal, G. S.; Khan, F.; Nealy, J. E.; Cucinotta, F. A.; Simonsen, L. C.; Shinn, J. L.; and Norbury, J. W.: Transport Methods and Interactions for Space Radiations. NASA RP-1257, 1991.

7. Freier, P.; Lofgren, E. J.; Ney, E. P.; and Oppenheimer, F.: The Heavy Component of Primary Cosmic Rays. Phys. Review, vol. 74, second ser., no. 12, 1948, pp. 1818-1827.

8. Simpson, J. A.: Introduction to the Galactic Cosmic Radiation. Composition and Origin of Cosmic Rays, Maurice M. Shapiro, ed., D. Reidel Publ. Co., 1983, pp. 1-24.

9. Adams, J. H.; Silberberg, R.; and Tsao, C. H.: Cosmic Ray Effects on Microelectronics. Part I - The Near-Earth Particle Environment. NRL Memo. Rep. 4506-pt. I, U. S. Navy, 1981. (Available from DTIC as AD A103 897.)

10. Simpson, J. A.: Elemental and Isotopic Composition of the Galactic Cosmic Rays. Annual Review of Nuclear and Particle Science, vol. 33, J. D. Jackson, H. E. Gove, and R. F. Schwitters, eds., Annual Reviews Inc., 1983, pp. 323-381.

11. Peters, B.: The Nature of Primary Cosmic Radiation. Progress in Cosmic Ray Physics, J. G. Wilson, ed., Interscience Publ., Inc., 1958, pp. 191-242.

Reproduced with permission of the copyright owner. Further reproduction prohibited without permission.

12. Schaefer, H. J.: Evaluation of Present-Day Knowledge of Cosmic Radiation at Extreme Altitude in Terms of the Hazard to Health. J. Aviation Med., vol. 21, no. 5, 1950, pp. 375-418.

13. Schaefer, H. J.: Exposure Hazards from Cosmic Radiation beyond the Stratosphere and in Free Space. J. Aviation Med., vol. 23, no. 4, 1952, pp. 334-344.

14. Anon.: Guidance on Radiation Received in Space Activities. NCRP Rep. No. 98, National Council on Radiation Protection and Measurements, 1989.

15. Alsmiller, R. G. Jr.; Irving, D. C.; Kinney, W. E.; and Moran, H. S.: The Validity of the Straightahead Approximation in Space Vehicle Shielding Studies. Second Symposium on Protection Against Radiations in Space, Arthur Reetz, Jr., ed., NASA SP-71, 1965, pp. 177-181.

16. Wilson, J. W.; Chun, S. Y.; Badavi, F. F.; and John, S.: Coulomb Effects in Low-Energy Nuclear Fragmentation, NASA TP-3352, 1993.

17. Townsend, L. W.; Wilson, J. W.; Tripathi, R. K.; Norbury, J. W.; Badavi, F. F.; Khan, F.: HZEFRG1: An Energy-Dependent Semiempirical Nuclear Fragmentation Model. NASA TP-3310, 1993.

Reproduced with permission of the copyright owner. Further reproduction prohibited without permission.

18. Wilson, J. W.; Chun, S. Y.; Badavi, F. F.; Townsend, L. W.; Lamkin, S. L.: HZETRN: A Heavy Ion/Nucleon Transport Code for Space Radiations. NASA TP-3146, 1991.

19. Aghamohammadi, S. Z.; Goodhead, D. T.; and Savage, J. R.: Induction of Sister Chromatid Exchanges (SCE) in G0 Lymphocytes by Plutonium-238 Alpha-Particles. Int. J. Radiat. Biol. & Relat. Stud. Phys., Chem. & Med., vol. 53, no. 6, 1988, pp. 909-915.

20. Kadhim, M. A.; Macdonald, D. A.; Goodhead, D. T.; Lorimore, S. A.; Marsden, S. J.; and Wright, E. G.: Transmission of Chromosomal Instability After Plutonium α-Particle Irradiation. Nature, vol. 355, no. 6362, 1992, pp. 738-740.

21. Kraft, G.: Radiobiological Effects of Very Heavy Ions: Inactivation, Induction of Chromosome Aberrations and Strand Break. Nucl. Sci. Appl., sect. A, vol. 3, no. 1, 1987, pp. 1-28.

22. Schimmerling, W.; Rapkin, M.; Wong, M.; Howard, J.: The Propagation of Relativistic Heavy Ions in Multielement Beams Lines. Med. Phys., vol. 13, 1983, pp. 212-228.

23. Wilson, John W.: Analysis of the Theory of High-Energy Ion Transport. NASA TN D-8381, 1977.

Reproduced with permission of the copyright owner. Further reproduction prohibited without permission.

24. Wilson, John W.: Heavy Ion Transport in the Straight Ahead Approximation. NASA TP-2178, 1983.

25. Wilson, John W.; Townsend, L. W., ; Bidasaria, H. B.; Schimmerling, W.; Wong, M.; and Howard, J.: ^{20}Ne Depth-Dose Relations in Water. Health Phys., vol. 46, no. 5, 1984, pp. 1101-1111.

26. Schimmerling, W.; Miller, J.; Wong, M.; Rapkin, M.; Howard, J.; Spieler, H. G.; and Jarret, B. V.: The Fragmentation of 670 A MeV Neon-20 as a Function of Depth in Water. Radiat. Res., vol. 120, 1989, pp. 36-71.

27. Shavers, M. R.; Curtis, S. B.; Miller, J.; and Schimmerling, W.: The Fragmentation of 670 A MeV Neon-20 as a Function of Depth in Water. II. One-Generation Transport Theory, Radiat. Res., vol. 124, 1990, pp. 117-130.

28. Wilson, John W.; Lamkin, S. L.; Farhat, H.; Ganapole, B. D.; and Townsend, L. W.: A Hierarchy of Transport Approximations for High Energy Heavy (HZE) Ions. NASA TM-4118, 1989.

29. Wilson, John W.; and Badavi, F. F.: New Directions in Heavy Ion Shielding. Proceedings of the Topical Meeting on New Horizons in Radiation Protection and Shielding, American Nuclear Soc., Inc., 1992, pp. 205-211.

Reproduced with permission of the copyright owner. Further reproduction prohibited without permission.

30. Wilson, J. W.; Townsend, L. W.; and Badavi, F. F.: A Semiempirical Nuclear Fragmentation Model. Nucl. Instrum. & Methods Phys. Res., vol. B18, no. 3, 1987, pp. 225-231.

31. Wilson, J. W.; Badavi, F. F.; Costen, R. C.; and Shinn, J. L.: Nonperturbative Methods in HZE Ion Transport. NASA TP-3363, 1993.

32. Wilson, John W.; and Badavi, F. F.: Methods of Galactic Heavy Ion Transport. Radiat. Res., vol. 108, 1986, pp. 231-237.

33. Wilson, John W.; and Townsend, L. W.: A Benchmark for Galactic Cosmic-Ray Transport Codes. Radiat. Res., vol. 114, no. 2, 1988, pp. 201-206.

34. Bethe, Von H.: Zur Theorie des Durchgangs schneller Korpuskularstrahlen durch Materie. Ann. Phys., 5 Folge, Bd. 5, 1930, pp. 325-400.

35. Silberberg, R.; Tsao, C. H.; and Shapiro M. M.: Semiempirical Cross Sections, and Applications to Nuclear Interactions of Cosmic Rays. Spallation Nuclear Reactions and Their Applications, B. S. P. Shen and M. Merker, eds., D. Reidel Publ. Co., 1976, pp. 49-81.

Reproduced with permission of the copyright owner. Further reproduction prohibited without permission.

36. Silberberg, R.; Tsao, C. H.: Partial Cross-Sections in High-Energy Nuclear Reactions, and Astrophysical Applications. I. Targets with $Z \leq 28$. Astrophys. J. Suppl. Ser., no. 220(I), vol. 25, 1973, pp. 315-333.

37. Bertini, H. W.; Guthrie, M. P.; and Culkowski, A. H.: Nonelastic Interactions of Nucleons and π-Mesons with Complex Nuclei at Energies Below 3 GeV. ORNL TM-3148, U.S. Atomic Energy Commission, 1972.

38. Wilson, J. W.; Townsend, L. W.; and Badavi, F. F.: Galactic HZE Propagation Through the Earth's Atmosphere. Radiat. Res., vol. 109, no. 2, 1987, pp. 173-183.

39. Bowman, J. D.; Swiatecki, W. J.; and Tsang, C. F.: Abrasion and Ablation of Heavy Ions. LBL-2908, Lawrence Berkeley Lab., Univ. of California, 1973.

40. Rudstam, G.: Systematics of Spallation Yields. Zeitschrift fur Naturforschung, vol. 21a, no. 7, 1966, pp. 1027-1041.

41. Wilson, J. W.; Shinn, J. L.; Townsend, L. W.; Tripathi, R. K.; Badavi, F. F.; and Chun, S. Y.: NUCFRG2: A Semiempirical Nuclear Fragmentation Model. Nucl. Instrum. & Methods Phys. Res., vol. B94, 1994, pp. 95-102.

Reproduced with permission of the copyright owner. Further reproduction prohibited without permission.

42. Shinn, J. L.; John, S.; Tripathi, R. K.; Wilson, J. W.; Townsend, L. W.; and Norbury, J. W.: Fully Energy-Dependent HZETRN (A Galactic Cosmic-Ray Transport Code). NASA TP-3243, 1992.

43. Wilson, J. W.; Badavi, F. F.; Shinn, J. L.; and Costen, R. C.: Approximate Green's Function Methods for HZE Transport in Multilayered Materials. NASA TM-4519, 1993.

44. Wilson, J. W.; Wood, J. S.; Shinn, J. L.; Cucinotta, F. A.; and Nealy, J. E.: A Proposed Performance Index for Galactic Cosmic Ray Shielding Materials. NASA TM-4444, 1993.

45. Wilson, J. W.; Cucinotta, F. A.; Shinn, J. L.: Multiple Lesion Track Structure Model. NASA TP-3185, 1992.

46. Wilson, J. W.; and Badavi, F. F.: A Study of the Generation of LET Spectra for Space Radiations. NASA TM-4410, 1992.

47. Kim, M. Y.; Wilson, J. W.; Thibeault, S. A.; Nealy, J. E.; Badavi, F. F.; and Kiefer, R. L.: Performance Study of Galactic Cosmic Ray Shield Materials. NASA TP-3473, 1994.

48. E. R. Long, Jr.: Electron and Proton Absorption Calculations for a Graphite/Epoxy Composite Model. NASA TP-1568, 1979.

Reproduced with permission of the copyright owner. Further reproduction prohibited without permission.

49. Nealy, J. E.; Wilson, J. W.; and Townsend, L. W.: Solar Flare Shielding with Regolith at a Lunar-Base Site. NASA TP-2869, 1988.

50. Johnson, R. N.; Farnham, A. G.; Clendinning, R. A.; Hale, W. F.; and Merriam, C. N.: Poly(aryl Ethers) by Nucleophilic Aromatic Substitution. I. Synthesis and Properties. J. Polym. Sci.: Part A-1, vol. 5, 1967, pp. 2375-2398.

51. White, D. M.; Takekoshi, T.; Williams, F. J.; Relles, H. M.; Donahue, P. E.; Klopfer, H. J.; Loucks, G. R.; Manello, J. S.; Matthews, R. O.; and Schluenz, R. W.: Polyetherimides via Nitro-Displacement Polymerization: Monomer Synthesis and ^{13}C-NMR Analysis of Monomers and Polymers. J. Polym. Sci.: Polym. Chem. Ed., vol. 19, 1981, pp. 1635-1658.

52. Sroog, C. E.; Endrey, A. L.; Abramo, S. V.; Berr, C. E.; Edwards, W. M.; and Olivier, K. L.: Aromatic Polypyromellitimides from Aromatic Polyamic Acids. J. Polym. Sci.: Part A vol. 3, 1965, pp. 1373-1390.

53. Kraus, W. B. ; Glasgow, M. B.; Kim, M. Y.; Olmeijer, D. L.; Kiefer, R. L.; Orwoll, R. A.; and Thibeault, S. A.: Boron Containing Polymers for Radiation Shielding. Polym. Prep., vol. 34, 1993, pp. 592-593.

Reproduced with permission of the copyright owner. Further reproduction prohibited without permission.

54. Shinn, J. L.; Townsend, L. W.; and Wilson, J. W.: Galactic Cosmic Radiation Levels in Spacecraft on Interplanetary Missions. The World Space Congress, 43rd Congress of the International Astronautical Federation and 29th Plenary Meeting of the Committee on Space Research, International Astronautical Federation and Committee on Space Research, 1992, pp. 567-568.

55. Cucinotta, F. A.: Calculations of Cosmic-Ray Helium Transport in Shielding Materials. NASA TP-3354, 1993.

56. O'Neill, P. M.; Badhwar, G.D.: Single Event Upsets for Space Shuttle Flights of New General Purpose Computer Memory Devices. IEEE Trans. Nucl. Sci., vol. 41, no. 5, 1994, pp. 1755-1764.

57. Taber, A. H.; Gillow, A. V.; and Dickinson, R. E.: Space Shuttle General Purpose Computer Radiation Effects Study--1991 Update. IBM Report 91-L75-001, 1991.

58. Pickel, J. C.; and Blandford, Jr., J. T.: Cosmic-Ray-Induced Errors in MOS Devices. IEEE Trans. Nucl. Sci., vol. NS-27, no. 2, 1980, pp. 1006-1015.

59. Badhwar, G. D.; Cucinotta, F. A.; and O'Neill, P. M.: Depth-Dose Equivalent Relationship at Various Solar Minima. Radiat. Res., vol. 134, 1993, pp. 9-15.

Reproduced with permission of the copyright owner. Further reproduction prohibited without permission.

60. Petersen, E. L.; Pickel, J. C.; Adams, Jr., J. H.; and Smith, E. C.: Rate Prediction for Single Event Effects--a Critique. IEEE Trans. Nucl. Sci., vol. 39, no. 6, 1992, pp. 1577-1599.

61. Schimmerling, W.: Radiobiological Problems in Space--An Overview. Radiat. & Environ. Biophys., vol. 31, 1992, pp. 197-203.

62. 1990 Recommendations of the International Commission on Radiobiological Protection. ICRP Publ. 60, Pergamon Press Inc., 1991.

63. Committee on the Biological Effects of Ionizing Radiations: Health Effects of Exposure to Low Levels of Ionizing Radiation. BEIR V, National Academy Press, 1990.

64. Wilson, J. W.; Cucinotta, F. A.; and Shinn, J. L.: Cell Kinetics and Track Structure. Biological Effects and Physics of Solar and Galactic Cosmic Radiation, Part B, C. E. Swenberg, G. Horneck, and E. G. Stassinopoulos, eds., Plenum Press, 1993, pp. 295-338.

65. Yang, T. C.; and Tobias, C. A.: Neoplastic Cell Transformation by Energetic Heavy Ions and Its Modification With Chemical Agents. Adv. Space Res., vol. 4, no. 10, 1984, pp. 207-218.

Reproduced with permission of the copyright owner. Further reproduction prohibited without permission.

66. Yang, T. C.; Craise, L. M.; Mei, M.; and Tobias, C. A.: Neoplastic Cell Transformation by High-LET Radiation: Molecular Mechanisms. Adv. Space Res., vol. 9, no. 10, 1989, pp. 131-140.

67. Bond, V. P.; Varma, M. N.; and Sondhaus, C. A.: The RBE Concept, Its Inadequacies and a Suggested Replacement. Mechanisms of Radiation Interaction With DNA: Potential Implications for Radiation Protection, CONF-870163, U.S. Dep. of Energy, 1988, pp. 31-38.

68. Xapsos, M. A.; Burke, E. A.; Shapiro, P.; and Summers, G. P.: Energy Deposition and Ionization Fluctuations Induced by Ions in Small Sites--An Analytical Approach. Radiat. Res., vol. 137, no. 2, 1994, pp. 152-161.

69. Todd, P.: Unique Biological Aspects of Radiation Hazards--An Overview. Adv. Space Res., vol. 3, no. 8, 1983, pp. 187-194.

70. The Quality Factor in Radiation Protection. ICRU Rep. 40, International Commission on Radiation Units and Measurements, 1986.

71. Wilson, J. W.; Nealy, J. E.; Schimmerling, W.; Cucinotta, F. A.; and Wood, J. S.: Effects of Radiobiological Uncertainty on Vehicle and Habitat Shield Design for Missions to the Moon and Mars. NASA TP-3312, 1993.

Reproduced with permission of the copyright owner. Further reproduction prohibited without permission.

72. Scott, B. R.: Methodologies for Predicting the Expected Combined Stochastic Radiobiological Effects of Different Ionizing Radiations and Some Applications. Radiat. Res., vol. 98, no. 1, 1984, pp. 182-197.

73. Burns, F. J.; and Albert, R. E.: Dose-Response for Radiation-Induced Cancer in Rat Skin. Radiation Carcinogenesis and DNA Alterations, F. J. Burns, A. C. Upton, and G. Silini, eds., Plenum Press, 1986, pp. 51-70.

74. Thomson, J. F.; and Grahn, D.: Life Shortening in Mice Exposed to Fission Neutrons and γ Rays. VII. Effects of 60 Once-Weekly Exposures. Radiat. Res., vol. 115, 1988, pp. 347-360.

75. Katz, R.; Ackerson, B.; Homayoonfar, M.; and Sharma, S. C.: Inactivation of Cells by Heavy Ion Bombardment. Radiat. Res., vol. 47, 1971, pp. 402-425.

76. Wilson, J. W.; and Cucinotta, F. A.: Cellular Repair/Misrepair Track Model. NASA TP-3124, 1991.

77. Wilson, J. W.; Kim, M. Y.; Schimmerling, W.; Badavi, F. F.; Thibeault, S. A.; Cucinotta, F. A., Shinn, J. L.; and Kiefer, R. L.: Issues in Space Radiation Protection: Galactic Cosmic Rays. Health Phys., vol. 68, no. 1, 1995, pp. 50-58.

Reproduced with permission of the copyright owner. Further reproduction prohibited without permission.

78. Townsend, L. W.; Cucinotta, F. A.; and Wilson, J. W.: HZE Reactions and Data-Base Development. Biological Effects and Physics of Solar and Galactic Cosmic Radiation, Part B, C. E. Swenberg, G. Horneck, and E. G. Stassinopoulos, eds., Plenum Press, 1993, pp. 787-809.

79. Wilson, J. W.: Composite Particle Reaction Theory. Ph.D. Diss., College of William and Mary, 1975.

80. Wilson, J. W.; and Townsend, L. W.: An Optical Model for Composite Nuclear Scattering. Canadian J. Phys., vol. 59, no. 11, 1981, pp. 1569-1576.

81. Billen, D.: Commentary: Spontaneous DNA Damage and Its Significance for the "Negligible Dose" Controversy in Radiation Protection. Radiat. Res., vol. 124, 1990, pp. 242-245.

Reproduced with permission of the copyright owner. Further reproduction prohibited without permission.

VITA

Myung-Hee Yoon Kim

Born in Buchon, South Korea on 20 September, 1957. Entered the Department of Chemical Engineering at Inha University, Inchon, South Korea, and graduated in 1980 with a Bachelor of Science. Was employed for three years by the Department of Chemical Engineering at Inha University, as a research assistant and logistics. Joined her husband in 1983 who came to the big world to pursue a doctoral degree in Oceanography at the College of William and Mary at Virginia. Entered the Department of Computer Science at Christopher Newport College, Newport News, Virginia, and graduated in 1987 with a Bachelor of Science. Entered the Department of Mathematics at Hampton University, Hampton, Virginia, in 1988. Received Master of Science in Applied Mathematics in 1991. In January 1991, began Ph.D. program in Polymer Science in the Department of Applied Science at the College of William and Mary, Williamsburg, Virginia. She will commence research as a National Research Council Post Doctor fellow at the NASA Langley Research Center, Hampton, Virginia, after completion of the Ph.D. degree.

Reproduced with permission of the copyright owner. Further reproduction prohibited without permission.